Titre: Title:	Impact of Mechanical Parameters and Fiber Orientation in Myocardial Passive Stiffness Estimation
Auteur: Author:	Sarah Leclerc
Date:	2025
Type:	Mémoire ou thèse / Dissertation or Thesis
Référence: Citation:	Leclerc, S. (2025). Impact of Mechanical Parameters and Fiber Orientation in Myocardial Passive Stiffness Estimation [Mémoire de maîtrise, Polytechnique Montréal]. PolyPublie. https://publications.polymtl.ca/66823/

Document en libre accès dans PolyPublie
Open Access document in PolyPublie

URL de PolyPublie: PolyPublie URL:	https://publications.polymtl.ca/66823/
Directeurs de recherche: Advisors:	Delphine Périé-Curnier
Programme: Program:	Génie biomédical

POLYTECHNIQUE MONTRÉAL

affiliée à l'Université de Montréal

Impact of Mechanical Parameters and Fiber Orientation in Myocardial Passive Stiffness Estimation

SARAH LECLERC

Institut de génie biomédical

Mémoire présenté en vue de l'obtention du diplôme de *Maîtrise ès sciences appliquées*

Génie biomédical

Juillet 2025

POLYTECHNIQUE MONTRÉAL

affiliée à l'Université de Montréal

Ce mémoire intitulé :

Impact of Mechanical Parameters and Fiber Orientation in Myocardial Passive Stiffness Estimation

présenté par **Sarah LECLERC**
en vue de l'obtention du diplôme de *Maîtrise ès sciences appliquées*
a été dûment accepté par le jury d'examen constitué de :

Hervé LOMBAERT, président
Delphine PÉRIÉ-CURNIER, membre et directrice de recherche
Vicky WANG, membre externe

ACKNOWLEDGEMENTS

First, I would like to thank the thesis examination committee — Hervé Lombaert, Delphine Périé-Curnier, and Vicky Wang — for their interest in this work and the time they devoted to reviewing this manuscript.

A special thanks to my research supervisor, Prof. Delphine Périé-Curnier, for her support throughout this Master's project and for her trust in my work. I am grateful for her guidance when needed, while also allowing me the freedom to explore my curiosities and develop my own reflections on this project. Thank you as well for giving me the opportunity to be involved in teaching activities and to undertake an internship during my Master's program.

I am also deeply thankful to the LifeEngine team I worked with during my internship. It was a highly enriching experience in a truly positive work environment.

I would also like to thank the previous students from the lab. I am especially grateful to Franck Mahaltchimy, who had worked on this subject before me. He patiently answered my questions and helped me get off to a good start on the project. Thank you also to Agathe Bedoux for sharing her experience.

Of course, I want to thank Aurélien Lacourt, my lab colleague, with whom I shared the ups and downs of research. I am truly grateful that he always took the time to answer my countless questions and provided constructive feedback on my work.

I would also like to express my gratitude to Jean-Marc Peyrat and Martin Genet, who, despite their busy schedules, patiently answered my questions and offered valuable insights.

On a more personal note, I would like to thank my friends here in Montreal, who helped make these past two years truly amazing and unforgettable. Thanks to all of them, I had a wonderful time and learned so much. These friendships have been incredibly precious to me. None of the work presented in this manuscript would have been possible without clearing my mind during such good times I spent with them. These memories put a smile on my face as I write these lines.

Finally, I am extremely grateful to my parents, who have always believed in me — sometimes even more than I believed in myself — and who have always helped me move forward while putting problems into perspective. Last but not least, a special thank-you to my sisters — not only because I was explicitly asked to include them — but above all for their ability to bring me joy at any time, even from across the Atlantic.

RÉSUMÉ

Les survivants du cancer infantile présentent des risques cardiaques accrus en raison des effets cardiotoxiques du traitement contre le cancer. La détection précoce de l'insuffisance cardiaque est cruciale pour ajuster les doses de traitement. La rigidité myocardique du ventricule gauche est considérée comme un indicateur de la fonction cardiaque et un biomarqueur prometteur pour la détection précoce de la cardiotoxicité et l'insuffisance cardiaque.

La rigidité du myocarde peut être estimée de manière non invasive par optimisation inverse, en utilisant des modèles par éléments finis patient-spécifiques, basés sur l'imagerie par résonance magnétique (IRM). Cette approche implique la sélection d'une loi constitutive des matériaux et la définition de l'orientation des fibres cardiaques dans le modèle. L'impact de ces données sur l'estimation de la rigidité du myocarde reste méconnu. Ce projet vise à comprendre et à évaluer l'impact de ces deux paramètres du modèle sur l'estimation de la rigidité.

La première partie de ce travail se concentre sur l'impact des paramètres de la loi constitutive du myocarde. La loi de comportement du matériau est une loi exponentielle isotropique transverse de type Fung, décrite par *Guccione et al.* (1991), couramment utilisée dans les modèles mécaniques du ventricule gauche. Elle comprend un ensemble de trois paramètres d'anisotropie (b_f, b_t, b_{ft}) qui varient considérablement entre les études, ce qui complique la sélection d'un trio de paramètres optimal. Cette étude vise à comprendre et à évaluer l'influence de ces paramètres sur l'estimation de la rigidité globale.

L'analyse a été divisée en trois étapes. Tout d'abord, des essais d'extensions biaxiales et cisaillements triaxiaux ont été simulés à l'aide d'un modèle par éléments finis, afin de comprendre l'impact de chaque paramètre sur le comportement du tissu et de comparer les trios de paramètres rapportés dans la littérature. Ensuite, l'optimisation de la rigidité étant basée sur le déplacement du ventricule, l'impact des trois paramètres sur le déplacement d'une géométrie idéale du ventricule gauche a été étudié à l'aide d'un modèle par éléments finis. Enfin, l'impact des trios de paramètres sur l'estimation de la rigidité a été évalué à l'aide de cinq modèles par éléments finis patient-spécifiques.

Les différences entre les trios de paramètres résultent en des changements significatifs dans le comportement local du myocarde et la mécanique globale du ventricule gauche. Au sein de la plage de variation étudiée, le paramètre b_t s'est avéré être le plus influent, et b_{ft} a eu le moins d'impact. En cohérence avec ces résultats, des différences significatives dans l'estimation de la rigidité sont observées entre les différents trios de paramètres. Aucun modèle ne se démarque comme étant plus adapté en termes d'erreur résiduelle. Le trio de paramètres de *Xi et al.*

(2013) a été sélectionné dans le présent travail, bien qu'aucun autre trio de paramètres ne se soit révélé nettement moins adapté.

La deuxième partie de ce travail se concentre sur l'impact de l'orientation des fibres cardiaques. L'orientation des fibres est souvent considérée comme homogène de la base à l'apex et sur toute la circonférence, avec un angle d'hélice variant linéairement à travers la paroi du ventricule entre 60° à l'endocarde à −60° à l'épicarde, et l'angle transversal étant fixé à zéro. Les nouvelles techniques d'IRM de diffusion ont permis d'intégrer une orientation plus précise des fibres dans les modèles. Cependant, l'intégration d'une orientation patient-spécifique complète, basée sur des acquisitions de diffusion in vivo, reste un défi majeur. Cette étude vise à comprendre et à évaluer l'impact de l'orientation des fibres sur la rigidité globale.

Trois modèles par éléments finis patient-spécifiques ont été construits afin d'étudier l'impact de l'orientation des fibres dans chaque géométrie. Ces modèles ont d'abord servi à étudier l'impact de l'orientation sur la mécanique du ventricule gauche pendant l'inflation passive, en utilisant une valeur de pression standard. Ensuite, en utilisant une approche d'optimisation inverse et une pression spécifique au patient, la rigidité a été évaluée pour chaque sujet et comparée entre les différentes orientations des fibres. Dans chaque étude, la plage de variation de l'angle d'hélice a été modifiée à la fois globalement dans le ventricule et localement dans chaque secteur cardiaque. L'impact de la distribution transmurale de l'angle d'hélix a également été évalué, ainsi que l'implémentation d'un angle transverse non nul. Enfin, des tranches mi-ventriculaires de données de diffusion in vivo ont été intégrées à trois modèles par éléments finis patient-spécifiques afin d'évaluer les différences mécaniques qui résultent des différentes tranches de diffusion.

Cette étude révèle une augmentation des contraintes et déformations causée par des fibres alignées plus circulairement, ainsi qu'une modification du déplacement du ventricule pendant l'inflation. Aucun des dix-sept segments définis par l'American Heart Association (AHA) ne se distingue par un impact plus ou moins important. L'angle transverse a un impact minimal. Les estimations de la rigidité montrent des variations marquées entre les reconstructions basées sur différentes tranches de diffusion, mais ces différences restent limitées par rapport à l'impact des paramètres matériaux. Les estimations à l'effort montrent un impact de l'orientation des fibres comparable à celui observé au repos.

Ces résultats devraient aider à choisir les caractéristiques du modèle pour représenter l'anisotropie du myocarde. Ils s'agit d'une étape importante en vue de déterminer des valeurs standards et pathologiques de la rigidité du myocarde, et devrait permettre d'améliorer l'efficacité de ce biomarqueur dans la détection précoce de la cardiotoxicité et de l'insuffisance cardiaque.

ABSTRACT

Survivors of childhood cancer are at higher risk of cardiac disease due to the cardiotoxic effects of cancer treatments. Early detection of heart failure is crucial for adjusting treatment doses. Passive myocardial stiffness of the left ventricle is considered an indicator of cardiac function and a promising biomarker for early detection of cardiotoxicity and heart failure.

Myocardial stiffness can be estimated non-invasively by an inverse optimization approach, using patient-specific finite element models, based on Magnetic Resonance Imaging (MRI). This approach involves selecting an appropriate material constitutive law and defining the orientation of cardiac fibers in the model. The impact of these inputs on the estimation of myocardial stiffness remains to be investigated. This project aims to understand and evaluate the impact of these two model inputs on the estimation of myocardial stiffness.

The first part of this work focuses on the impact of myocardium constitutive law parameters. The material behavior law is an transversely-isotropic Fung-type exponential law, described by *Guccione et al.* (1991), commonly used in left ventricle mechanical models. It includes a set of three anisotropy parameters (b_f, b_t, b_{ft}) that vary significantly across studies, complicating the selection of an optimal parameter set. This study aims to understand and assess the influence of these parameters on the estimation of global stiffness.

The analysis was divided into three steps. First, extension biaxial and triaxial shear tests were simulated using a finite element model, to understand the impact of each parameter on the tissue behavior and to compare parameter sets reported in the literature. Then, since stiffness optimization is based on ventricle displacement, the impact of the parameters on the displacement of a finite element model of an ideal geometry of left ventricle was studied. Finally, the impact of the different parameter sets on the estimation of stiffness was evaluated using five patient-specific finite element models.

Differences between parameter sets resulted in significant changes in local material behavior and global mechanics of the left ventricle. Within the studied range of variation, b_t proved to be the most influential, and b_{ft} had the least impact. Consistent with these results, different parameter sets significantly affect the estimation of stiffness. No model stands out as being more suited in terms of residual error. The parameter set from *Xi et al.* (2013) was selected in the present work, although no other parameter set was found to be significantly less suitable.

The second part of this work focuses on the impact of cardiac fiber orientation. Fiber architecture is often considered to be homogeneous from base to apex and around the circumference,

with the helix angle varying linearly across the ventricle wall from 60° at the endocardium to −60° at the epicardium, and with the transverse angle set to zero. New Diffusion Tensor Imaging (DTI) techniques have enabled the implementation of a more accurate fiber orientation into models. However, a complete integration of personalized fiber architecture based on in-vivo DTI acquisitions remains a major challenge. This study aims to understand and assess the impact of fiber orientation on global stiffness.

Three patient-specific left ventricle geometries were integrated into finite element models to study the impact of fiber orientation in each geometry. These models first served to study the impact on left ventricle mechanics during passive inflation, using a standard pressure value. Then, using an inverse optimization approach and a patient-specific estimated pressure, patient-specific stiffness was assessed for each subject and compared between fiber orientation. In each study, the helix angle variation range was modified both globally in the ventricle, and locally by cardiac sectors. The impact of helix angle transmural distributions was also evaluated, as well as the implementation of a non-zero transverse angle. Finally, one-slices in-vivo DTI data were wrapped onto three patient specific finite element models to assess the mechanical differences that result from different DTI slices.

This study reveals an increase in stress and strain values caused by more circularly-aligned fibers, and change in the motion of the ventricle during inflation. No American Heart Association (AHA) segment stands out for greater or lesser impact. Transverse angle showed minimal impact. Stiffness estimates show clear variations between DTI-slice-based reconstructions, but the differences remain limited compared to the material parameters impact. Deviations observed with estimates during exercise are comparable to those at rest.

These results are intended to guide the selection of input features for the implementation of myocardial anisotropy. It represents a valuable step towards determining standard and pathological values of myocardial passive stiffness, and would help enhance the effectiveness of this biomarker in the early detection of cardiotoxicity and heart failure.

TABLE OF CONTENTS

LIST OF TABLES

LIST OF FIGURES

LIST OF SYMBOLS AND ACRONYMS

ALL   Acute Lymphoblastic Leukemia

AHA   American Heart Association

bSSFP   balanced Steady State Free Precession

DENSE   Displacement Encoding with Stimulated Echos

DTI   Diffusion Tensor Imaging

E2A   Sheetlet Angle

ECG   Electrocardiogram

FEM   Finite Elements Model

HA   Helix Angle

HAR   Helix Angle Range

LV   Left Ventricle

MRI   Magnetic Resonance Imaging

RF   Radiofrequency

RMSE   Root Mean Squared Error

SE   Spin-Echo

STEAM   Stimulated Echo Acquisition Mode

TA   Transverse Angle

LIST OF APPENDICES

CHAPTER 1   INTRODUCTION

1.1   Context

Childhood acute lymphoblastic leukemia (ALL) is the most frequently diagnosed cancer among children. It affects the blood and bone marrow, and accounts for about 25% of all cancer cases among children under the age of 15 [10]. Doxorubicine is a chemotherapy agent commonly prescribed for cancer treatment. However, the adverse effects remain significant. Compared to the general population, childhood cancer survivors have a five- to fifteen-fold increased risk of experiencing congestive heart failure due to the associated cardiotoxicity [11].

Early detection of heart failure is crucial for adjusting treatment doses. The diagnosis involves evaluating cardiac function, especially of the left ventricle, given its critical role in systemic circulation. Passive left ventricle myocardial stiffness has been shown to be a relevant biomarker for the early detection of cardiotoxicity [12].

Myocardial stiffness can be estimated non-invasively by an inverse optimisation approach, using patient-specific finite element models, based on Magnetic Resonance Imaging (MRI) [5, 7, 8]. The principle is as follows : the finite element model replicates the patient left ventricle geometry, and the myocardium stiffness parameter in the model is optimized so that the displacement of the ventricle in the simulation matches the MRI measurements.

The implementation of finite element models requires defining the left ventricle geometry, the myocardium constitutive law, the myofiber orientation, and loading and boundary conditions.

While it is widely accepted that the myocardium is anisotropic [13,14], its integration into finite element models continues to raise questions. Accounting for anisotropy involves selecting an appropriate material constitutive law and defining the orientation of cardiac fibers.

The assumption of transverse isotropy, with an axis of symmetry along the fiber direction has been widely used in modeling approaches. The myocardium passive mechanical response is characterized by four key parameters : global stiffness, local stiffness in the fiber's direction, cross-fiber direction, and fiber-transverse shear plane [14]. Global stiffness is the biomarker of interest, that is being estimated. The three anisotropy parameters vary significantly across studies, hindering the selection of an optimal set of parameters. They will be the focus of the first part of this study.

The implementation of transverse isotropy in the left ventricle requires the definition of fiber orientation. Fiber orientation was first described using a rough estimation derived from

histological observations [15] : a helical structure, with a right-handed spiral near the endo-cardial surface, and a left-handed spiral near the epicardial surface, which was subsequently validated by Diffusion Tensor Imaging (DTI) [16, 17]. New DTI techniques have enabled the integration of a more accurate and data-driven fiber orientation into models, based on either *ex-vivo* [8, 18, 19] or *in-vivo* acquisitions [20]. However, a complete personalization of fiber architecture based on in-vivo DTI acquisitions remains a major challenge. Its ability to improve the stiffness estimation has yet to be fully assessed. This will be the focus of the second part of this study.

1.2   Research objectives

This project aims to understand and evaluate the impact of myocardial anisotropy on the estimation of the left ventricle myocardial passive stiffness. This work is divided into two distinct studies.

In the first study, the three anisotropy parameters are investigated. The aim is to **under-stand and assess the influence of these parameters on global stiffness**. It is intended to provide guidance in choosing an adequate set of parameters.

The second study focuses on fiber orientation. The aim is to **understand and assess the impact of fiber orientation on global stiffness**. It is expected to guide the choice of an appropriate implementation method of fiber orientation, based on the desired level of accuracy for the estimation of stiffness.

In the long run, these steps aim to determine standard and pathological values of this biomarker, allowing early detection of cardiotoxicity and heart failure.

1.3   Thesis outline

The present thesis is structured into five chapters.

Chapter 1 introduces the background of the study and outlines the main objectives

Chapter 2 provides an overview of existing knowledge essential for understanding the present work. It first introduces the structure and function of the heart, (Section 2.1) cancer thera-pies' impact, and the associated challenges of early detection (Section 2.2). A brief overview of MRI techniques commonly used in early detection are also presented (Section 2.3). The myocardial mechanical properties and their assessment are then described (Section 2.4). The key points of this section are summarized in Section 2.5. Finally, a brief summary of F. Mahalatchimy's Master's thesis [21] on the subject of interest is provided (Section 2.6).

Chapter 3 assesses the impact of mechanical parameters on stiffness estimation. After a brief introduction (Section 3.1), the methods are presented (Section 3.2). A sensitivity study for each parameter, as well as a comparative study of different parameter sets reported in the literature, are performed. The results of both studies are presented in Section 3.3 and discussed in Section 3.4.

Chapter 4 assesses the impact of fiber orientation on stiffness estimation. The introduction (Section 4.1) is followed by a description of the methods (Section 4.2). The study is divided into five consecutive steps, each focusing on a specific parameter of the fiber architecture. For each step, the results are presented in Section 4.3 and discussed in Section 4.4.

Chapter 5 concludes this master's thesis with a summary of the work, the main limitations, and directions for future work.

CHAPTER 2   SCIENTIFIC BACKGROUND AND LITERATURE REVIEW

2.1   Structure and function of the heart

2.1.1   Cardiac anatomy

The **heart** is located in the center of the thoracic cavity, between the two lungs. Although its size depends on individuals, it is commonly approximated to the size of a fist. Its contraction sends blood to the rest of the body. The superior part, called the base, is oriented backward and slightly to the right, while the tip of the heart, called the apex, points forward, downward, and to the left. [1]

As illustrated in Figure 2.1, the heart can be divided into two parts :

- the **left side** of the heart is connected to the blood vessels of the systemic circuit, which carry oxygenated blood from the heart to the body, and return deoxygenated blood back to the heart
- the **right side** of the heart is connected to the blood vessels of the pulmonary circuit, which carry deoxygenated blood from the heart to the lungs, and return oxygenated blood back to the heart
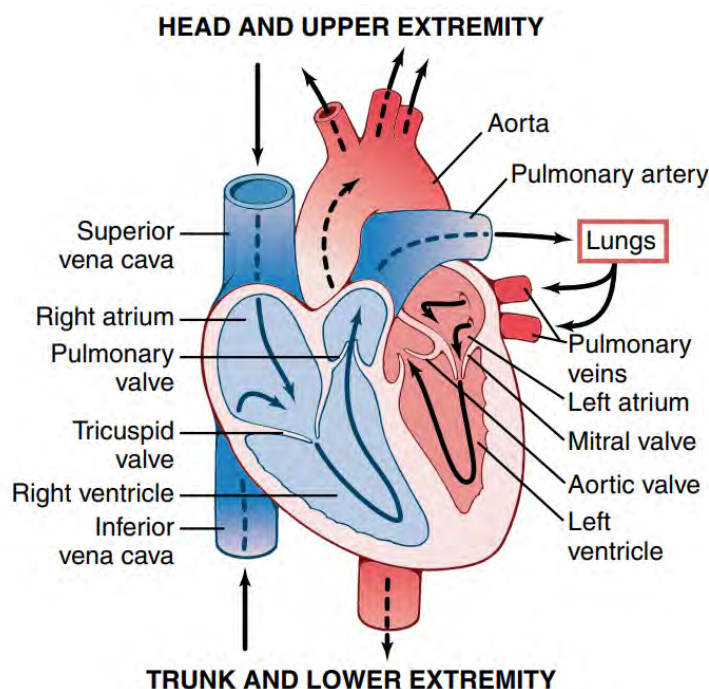
Figure 2.1 Structure of the heart (image taken from [1])

A central wall called "septum" separates the two sides. The left and right parts are each divided into two chambers : an upper one called "**atrium**" and a lower one called "**ventricle**". Valves are located at the entrance of each cavity, ensuring unidirectional blood flow.

Deoxygenated blood enters the right atrium through the superior and inferior vena cava. The right atrium ejects deoxygenated blood into the right ventricle through the tricuspid valve. The **right ventricle** then pumps **deoxygenated blood** through the pulmonary valve to the lungs. Blood is reoxygenated in the lungs before reaching the left atrium. The left atrium ejects oxygenated blood into the **left ventricle** (LV) through the mitral valve. The left ventricle then propels **oxygenated blood** through the aortic valve to the rest of the body. Figure 2.1 shows a schematic representation of these different structures. This circulation process is repeated continuously, maintaining blood flow throughout the body. [1]

The cardiac wall is composed of three layers. The **myocardium** is the central and thickest layer. It is made up of muscular tissue that ensures cardiac contraction. As the left ventricle must provide the necessary pressure to overcome the resistance of the systemic circuit and propel blood throughout the whole body, it is more than three times thicker than in the rest of the heart. Details of the myocardial structure are given in Section 2.1.3.

This layer is surrounded by an inner layer named **endocardium** and an outer layer named **epicardium**. The endocardium is directly in contact with blood inside the heart. The epicardium protects the inner structures of the heart and contributes to the production of pericardial fluid. This fluid is contained all around the heart, in the pericardial cavity, and reduces friction as the heart contracts. It is enclosed by the pericardium, which also helps anchor the heart in the thoracic cavity, preventing excessive movement during cardiac contractions. [22]

2.1.2 Cardiac cycle

With an average heart rate of 75 contractions per minute, the heart contracts 108 000 times a day, more than 39 million times a year [22]. Each cardiac cycle is composed of alternating relaxation and contraction of the atria and ventricles. During the relaxation phase, known as **diastole**, the ventricles fill with blood from the atria. During the contraction phase, known as **systole**, the blood is ejected from the ventricles. The left and right sides supply systemic and pulmonary circuits respectively. These phases are regulated by the activity of muscle cells and pressure variations within the cardiac chambers. [22]

The electrical impulse that activates the muscle cells of each heart chamber originates in the

sinoatrial node. It is then transmitted through the cardiac conduction pathways, first triggering atrial contraction, followed by ventricular contraction. On the electrocardiogram (ECG), the P wave represents atrial depolarization, the QRS complex corresponds to ventricular depolarization, and the T wave reflects ventricular repolarization.

Regarding systemic circulation, the cardiac cycle can be divided into five steps, illustrated in Figure 2.2 [23] :

1. **Isovolumetric contraction** : The left ventricle contracts, increasing pressure in this chamber, but the volume remains constant. The mitral and aortic valves are closed.
2. **Ventricular ejection** : When pressure in the left ventricle becomes greater than pressure in the aorta (about 80 mmHg), the aortic valve opens and blood is ejected from the ventricle. As blood is ejected, the pressure in the left ventricle decreases, causing the aortic valve to close when the pressure in the cavity is lower than in the aorta. The volume of blood, known as the telesystolic volume, is then at its lowest.
3. **Isovolumetric relaxation** : The pressure in the ventricle continues to decrease. A small amount of blood remains in the ventricle. All valves are closed, and the volume is constant during this phase.
4. **Rapid filling** : As the pressure in the atrium exceeds that in the ventricle, the mitral valve opens and blood rapidly flows into the ventricle.
5. **Diastasis** : Blood slowly flows from the atrium to the ventricle until the atrial and ventricular pressures equalize. The atrial contraction then ends the ventricle filling and the mitral valve closes. The volume of blood, known as the telediastolic volume, is at its highest.

These phases are repeated in each cardiac cycle, ensuring continuous blood flow in the body.
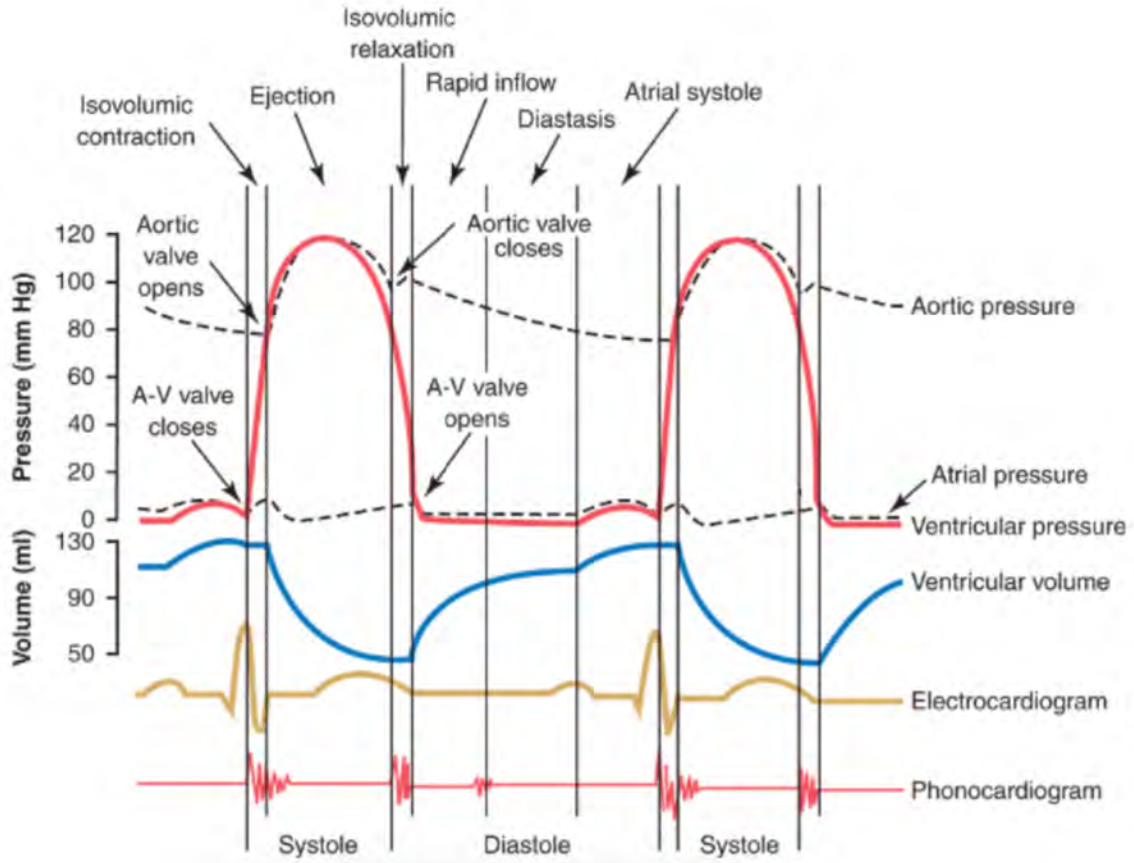
(a) Wiggers diagram (image taken from [23])
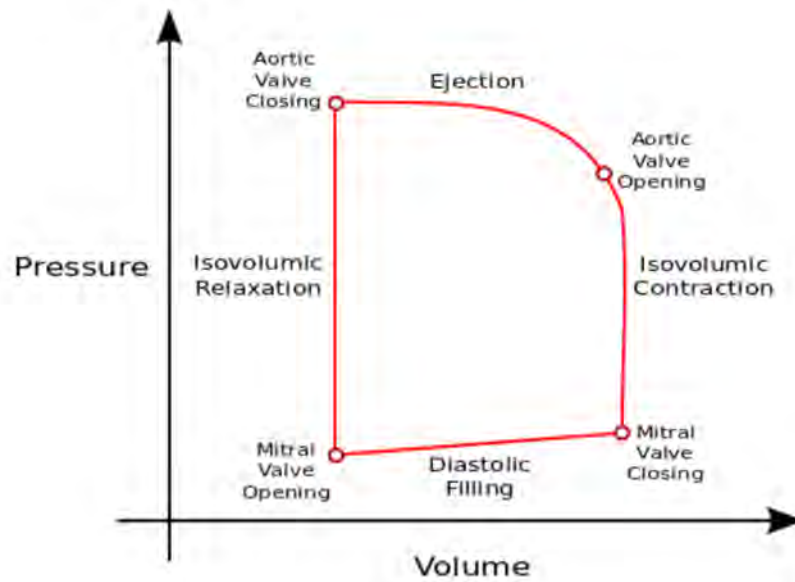
(b) Schematic pressure-volume loop (image taken from [23])

Figure 2.2 Vizualisation of the phases of the cardiac cycle

2.1.3 Myocardium mesostructure

Myocardium components :

The **myocardium**, the thickest layer of the cardiac wall, is responsible for tissue contraction during each cardiac cycle. It is composed of four major components : cardiomyocytes, fibroblasts, the extracellular matrix, and blood vessels. [24]

Cardiomyocytes are cylindrical cells that can be up to 7 times longer than their diameter [25]. They occupy 70% of the myocardium volume [13]. They are connected by intercalated discs, forming bundles called **myofibers**. Each cardiomyocyte is made up of several **myofibrils**, which are the basic contractile units of the cell. These myofibrils are a succession of sarcomeres, each composed of actin and myosin filaments, sliding relative to one another, causing the sarcomere to shorten and muscle contraction to occur at the tissue level. [24]

Fibroblasts are smaller cells that outnumber cardiomyocytes and are responsible for maintaining the extracellular matrix and anchor cardiomyocytes. [24]

The **extracellular matrix** supports cardiomyocytes and blood vessels. It plays a crucial role in maintaining their arrangement and distributing the load across the tissue. It is made up of collagen, elastin, and polyglycans. [25]. Collagen surrounds myofibers individually and connects them together, forming groups of myofibers called **sheetlets**, separated by cleavage planes. These sheetlets are about 4 cardiomyocytes thick. [26]

In the **left ventricle** wall, the myofibers gradually change orientation from a left-handed spiral near the epicardial surface to a circular arrangement in the middle of the wall and a right-handed spiral near the endocardial surface. A schematic representation of this **helical structure** is shown in Figure 2.3.
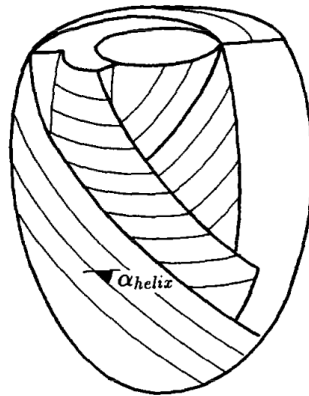
Figure 2.3 Schematic organization of myofibers in the LV (image taken from [2])

Myofiber architecture description :

Initial assessments of myofiber orientation were conducted through **histological analysis** [15]. The development of **Diffusion Tensor Imaging** (DTI) has since enabled both ex-vivo and in-vivo measurements of myofibers orientation in healthy and pathological conditions [16, 17, 27, 28], as well as assessments of myofiber mobility [29]. This technique will be described in greater detail in Section 2.3. **Micro-computed tomography** has also allowed for a more precise ex-vivo determination of cardiomyocyte orientation in myocardium samples [30].

In order to describe the myofibers architecture in the left ventricle, various coordinate systems and angular definitions have been introduced.
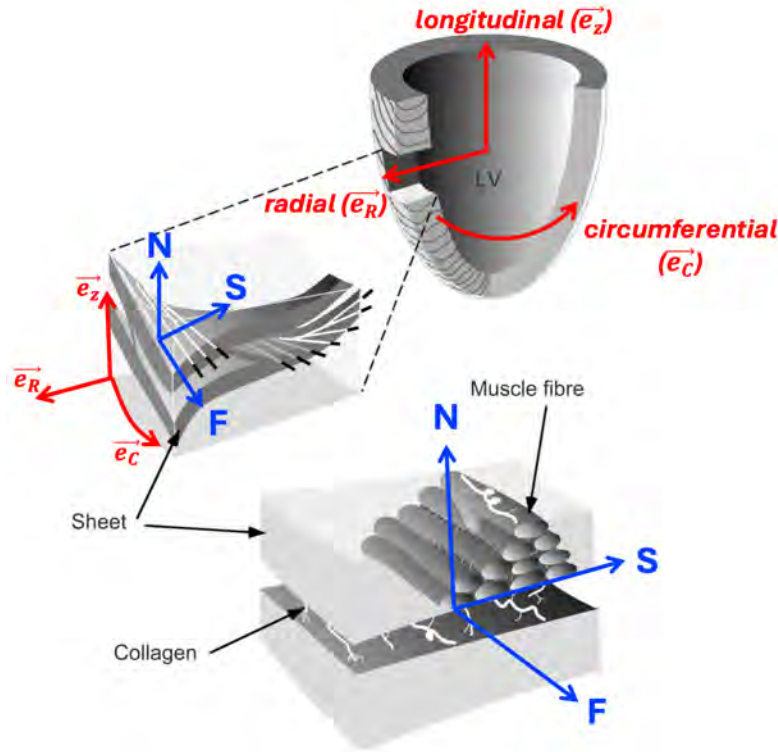
Figure 2.4 Local and global coordinate systems (image adapted from [3])

The **local coordinate system**, illustrated in Figure 2.4, refers to the aforementioned myocardium microstructure : the three axis are respectively oriented along the **fiber** axis (F), **sheetlet** plane direction (S), and **sheetlet-normal** direction (N) [26]. These three vectors are assumed to be orthogonal, even if this is not always the case in practice [31].

The **global coordinate system**, illustrated in Figure 2.4, refers to the global geometry

of the left ventricle [32]. The **longitudinal axis** is perpendicular to the base plane, and passes through the apex. The **radial axis** is perpendicular to the longitudinal axis, and oriented from the center of the left ventricular cavity toward the epicardium surface. The **circumferential axis** follows the curve of the epicardium surface and is orthogonal to the radial and longitudinal directions.

Three main angles, illustrated in Figure 2.5, have been introduced to orient the local co-ordinate system in the global coordinate system, thus allowing a complete description of myofibers architecture in the ventricle : the **helix angle** (HA), **transverse angle** (TA), and **sheetlet angle** (E2A).
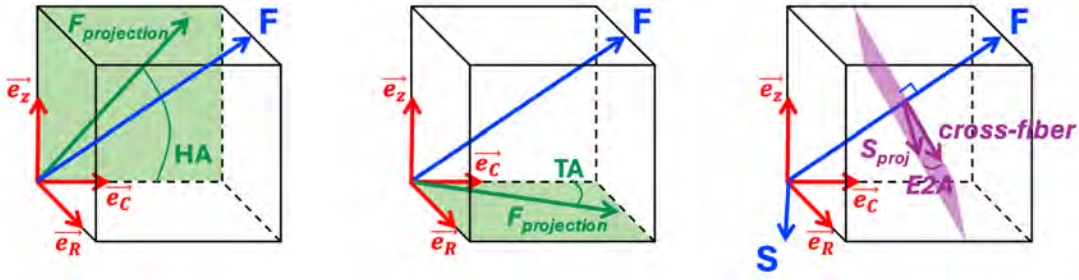
Figure 2.5 Angular definitions for myofiber orientation

Helix angle :

The **helix angle** is defined between the myofiber direction projected onto the longitudinal - circumferential plane and the circumferential direction (see Figure 2.5). This angle is the most extensively documented in the literature.

One of the first and most frequently cited studies in the field is the work conducted by *Streeter et al.* [15]. Based on histological analysis of 18 ex-vivo canine hearts, he concluded that helix angle changes smoothly from about **60° at the endocardium** to about **−60° at the epicardium**. The ratio of fibers oriented circumferentially ($|HA| < 22.5°$) to those aligned in the longitudinal directions ($|HA| > 67.5°$) is approximately 10 to 1.

Although some significant differences have been observed between species [33], this global cardiac architecture observed by *Streeter et al.* [15] has been confirmed in the human heart by DT-MRI studies [16, 27]. *Lombaert et al.* [16] and *Toussaint et al.* [27] reported respectively an average angle of 66° and 55° at the endocardium and −41° and −30° at the epicardium in the human heart. DT-MRI of the human heart revealed a fairly **homogeneous** distribution from base to apex, with smooth variation from the endocardium to epicardium strongly

correlated with transmural depth, except near the apex [16, 17, 33].

This **helical architecture** of cardiac fibers plays a crucial role in the efficient contraction of the left ventricle, particularly in ventricular strain, rotation, and shortening [23, 25].

However, despite a generally homogeneous architecture in the ventricle, some studies have highlighted strong **local variations**. For example, both DTI and micro-computed tomography analysis have demonstrated that the fiber architecture is disrupted at the junction between the left and right ventricles [29, 30, 34]. In this region, the presence of crossing fibers leads to abrupt changes and mixed directional patterns. Some local perturbation of fibers orientation have also been observed around cardiac blood vessels [35]. Overall, micro-computed tomography has revealed abrupt local variations of cardiac fiber on the micrometer scale, which are not visible when measured at the milimeter scale of DTI [30, 35, 36].

DTI has also enabled assessing the **helix angle evolution** though cardiac cycle. From diastole to systole, helix angle steepen : positive values near endocardium increase, and negative values near epicardium decrease [37], leading the helix angle range (HAR) to increase. *Moulin et al.* [29] reported a mi-ventricular helix angle range varying from 76.9° in average in early systole, to 96.6° in average in late systole.

Transverse angle :

Transverse angle measures the deviation of myofiber with respect to the circumferential direction (see Figure 2.5). It is measured by projecting the fiber axis onto the radial-circumferential plane and calculating the angle between this projection and the circumferential direction.

It is much less documented than helix angle. As this angle is quite small, it is often considered to be **zero** [27]. *Lombaert et al.* [16] reported an average transverse angle of 7°, *Toussaint et al.* [27] of 0°, and *Chen et al.* [38] reported values of transverse angle between 20 and -20 throughout the ventricle throughout the cardiac cycle. Thus, the fibers are mainly oriented parallel to the wall surface.

However, as for helix angle, this assumption masks more significant local variations, which are not always detected by the precision of DTI [28, 39].

There is **no global pattern** describing the evolution of the transverse angle in the ventricle, as there is for the helix angle. The transverse angle is poorly correlated with the wall transmural depth [16, 27].

Sheetlet angle :

The **sheetlet angle**, also named E2A, is measured between the sheet direction projected onto the cross-fiber plane and the myofiber perpendicular direction (see Figure 2.5).

This angle **varies** much within the left ventricle, and is poorly correlated with the wall transmural depth [16, 27].

Several authors have highlighted the existence of **two populations of sheetlets**, oriented in different directions [35, 36]. This could explain the variability of measurements observed by DT-MRI [17]

While the change helix angle during the cardiac cycle was moderate, the change in sheetlet angle is much more significant [29]. This variation is called **E2A mobility** and reflects sheetlets function [25]. As early as 1969, *Streeter et al.* had observed that cardiomyocytes thickening by itself could not fully account for the whole wall thickening during systole. Recent findings reported the correlation between E2A mobility and radial LV thickening [40], explaining how sheetlets reorientation during systole could account for wall thickening. *Moulin et al.* [29] reported a mi-ventricular sheetlet angle varying from 27.7° in average in early systole, to 45.2° in average in late systole.

Pathological conditions :

Abnormalities in cardiac fiber architecture and mobility have been associated with **pathological conditions**, such as infarctus [41], congenital heart disease [28], dilated cardiomyopathy [37, 40], or hypertrophic cardiomyopathy [40]. Crossing fibers with more abrupt angle variations were reported in infarcted region [41]. Helix angle and helix angle range were altered in hearts affected by congenital heart disease [28]. Helix angle steepening during systole is lower in patient with dilated cardiomyopathy, which could reduce left ventricle torsion, and ejection efficiency [37]. E2A mobility is reduced in patients with dilated cardiomyopathy and patients with hypertrophic cardiomyopathy [40].

2.2 Childhood acute lymphoblastic leukemia

Childhood acute lymphoblastic leukemia is a cancer of the blood and bone marrow. It is the most frequently diagnosed cancer in children, accounting for about 25% of all cancer cases among children under 15 years of age [10]. In the US, it represents about 3100 new cases each year, and this figure has increased since 1975 [10]. Recent cancer treatments have improved survival rates in the last four decades [42].

2.2.1 Treatment-related cardiotoxicity

Doxorubicine is a chemotherapy drug that belongs to the anthracycline class. It destroys cancer cells by interfering with DNA synthesis. It is used to treat more than half of all children with acute lymphoblastic leukemia [11]. However, it can have serious consequences on the heart and increase the risk of long-term morbidity and mortality [42]. In fact, child cancer survivors are at higher risk for cardiac disease than healthy children due to cancer therapy [43]. Cardiotoxicity depends on the dose of administered doxorubicine [44] and can appear up to 4 to 20 years after treatment ends [45]. **Cardiotoxicity** may induce arrhythmias, pericardial disease, valvular disease, or coronary artery disease, although it is most commonly associated with the development of congestive heart failure [44] . Childhood cancer survivors are between 5 and 15 times more likely to experience congestive heart failure than people in the general population [11]. The prognosis is poor, with a five-year survival rate below 50% following diagnosis [11].

Cardiotoxicity comes from toxic substances, produced by doxorubicine, which damage cardiac cells and disrupt calcium balance, hindering contraction. This leads to systolic and diastolic dysfunction [45]. **Diagnosis** consists of assessing the cardiac functions, and especially the **left ventricular** performance to pump blood into the systemic circulation.

2.2.2 Diagnostic tools

Biopsy, which involves collecting samples of myocardial tissue, is the most reliable technique to detect tissue damage and assess the severity of the disease. However, this is an invasive technique and can have side effects [45].

Echocardiography is a standard technique in cardiac evaluation. It is widely used because it is an easy-to-access and low-cost technique. The two main indices estimated from echocardiographic images derived indices are the left ventricular ejection fraction and the fractional shortening. However, these parameters are often insensitive to the early detection of cardiotoxicity of doxorubicin [46]. More recently, Doppler echocardiography, which enables the measurement of strain and strain rate, appeared as a promising tool to assess myocardial condition, as it is more sensitive to early damage [47, 48]. Stress echocardiography is also more sensitive to early subclinical changes, which is promising for early detection [49, 50].

Cardiac Magnetic Resonance Imaging (MRI) is also used as a diagnostic tool. It is more expensive than ultrasound, but the image quality is better. Cardiac cine-MRI can be used to measure left ventricle volume, mass, and ejection fraction, which are commonly used cardiac function indices [51]. However, these parameters are not sensitive enough to detect

cardiotoxicity at an early stage [45]. Measurement of left ventricle strain, through Tag MRI, Strain Encoding MRI, or Displacement ENcoding with Stimulated Echoes (DENSE), has been shown to be a promising predictor of cardiotoxicity of anthracyclines [52,53]. The strain can also be assessed using cine-MRI post-processing tissue tracking methods [51]. Magnetic resonance imaging can also be used to assess the characteristics of myocardial tissue, thus helping to detect early cardiotoxicity [46]. Gadolinium contrast, or T1 and T2 mapping are the commonly used methods for this purpose [51]. Cardiac MRI during exercise testing is also being developed for early detection of doxorubicine cardiotoxity, as it could emphasize a decrease of cardiac mechanical performances which are not visible at rest [54].

Currently, there is no standardized method for early detection of cardiotoxicty and the left ventricle ejection fraction remains the standard [51]. However, this parameter has been shown to be insufficient for subclinical changes [45, 48, 52].

2.2.3   Myocardial stiffness : biomarker of cardiotoxicty and heart failure

As tissue characterization and strain assessment were reported to be promising tools [46, 48, 52, 53], the **estimation of left ventricle myocardial stiffness** has emerged as a potential interesting biomarker for the early detection of doxorubicin cardiotoxicity [12]. In the more general case of cardiac pathologies and heart failure, this **biomarker** has been shown to be a **relevant** indicator of cardiac function, especially in cases of heart failure with preserve ejection fraction [55–58]. Stiffening of the ventricle walls alters diastolic filling and increase end-diastolic pressure [55], which has a direct impact on pumping efficiency : limiting the diastolic relaxation implies restricting the amplitude of contraction [59, 60].

The **end-diastolic pressure-volume relationship** can be used to estimate the passive left ventricle myocardial stiffness. However, this estimation reflects global apparent stiffness and is greatly influenced by ventricular geometry, rather than reflecting inherent tissue stiffness. For example, between walls of same stiffness, a thicker wall will appear stiffer, because it requires a higher pressure to be deformed. [20]

Another method of estimating left ventricle myocardial stiffness now rely on **patient-specific left ventricle finite element models**. The different existing models will be detailed in Section 2.4.2. The estimation principle is as follows :

- MRI scans make it possible to determine the geometry of the patient's left ventricle, and the numeric model reproduces this geometry
- cine-MRI or tag-MRI makes it possible to know the displacement or strain of the left ventricle during the diastolic phase

- in the numeric model, the stiffness parameter of the ventricle is iteratively optimized, so that displacement or strain at the end of the simulation best matches MRI data

This method has already been used to reveal increased passive stiffness in patients with heart failure [61], or to study the stiffness of the left ventricle in pathological conditions [5, 9, 62].

However, the limited number of patients included in these studies hinders the establishment of **standard stiffness values** for both healthy and pathological conditions, thus limiting its potential as a validated clinical biomarker.

In the case of children treated with doxorubicin, slight changes in myocardial hyperelastic properties have been observed [12]. These are only preliminary results, and further studies are needed to validate and expand upon these findings.

2.3 Cardiac Magnetic Resonance Imaging

As described in the previous section, MRI is widely used in the context of in-vivo stiffness estimation. An in-depth understanding of MRI is not necessary for this project, but an overview will be useful to better understand how MRI techniques can provide valuable information for biomechanical models of the left ventricle, but face certain challenges.

Basics :

MRI is based on the physical phenomenon called **nuclear magnetic resonance**. The principle is as follows [63]:

- when an **external magnetic field** $\vec{B}_o$ is applied, atomic nuclei become magnetized, aligning their magnetization with the field
- a **radiofrequency (RF) pulse** causes the magnetization M to precess around $\vec{B}_o$, and induces a RF pulse, which generates the signal observed in MRI
- the magnetization vector $\vec{M}$ has two components : **longitudinal** magnetization, aligned with $\vec{B}_o$, and **transverse** magnetization, in the perpendicular plane
- once RF is removed, magnetization vector $\vec{M}$ gradually ends the precession movement, and aligns back with $\vec{B}_o$

This **relaxation** is characterized by two characteristics times : T_1 and T_2, corresponding respectively to longitudinal and transverse relaxations. These relaxation times depend on **tissue properties**. Thus, by manipulating RF excitation pulse-sequences, taking into account differences of T_1 and T_2 between tissues, it is possible to produce MR images with sufficient **contrast** between anatomical structures to be discernible.

A key challenge of cardiac MRI is that heart is **constantly beating**. Because of this movement of the heart, MRI acquisition of the whole heart anatomy, i.e. with several image slices, requires the acquisition to last several cardiac cycles. Cardiac MRI acquisitions thus need to be synchronized with the patient **electrocardiogram**, and often require the patient to **hold his breath** to avoid respiratory movements. Moreover, due to cardiac motion, cardiac MRI pulse sequences must also be **fast**. [64]

The MRI sequence known as **balanced Steady State Free Precession** (bSSFP) is highly appreciated for its good contrast and signal-to-noise ratio [65]. This sequence is also widely used for cardiac cine MRI acquisitions [64].

Cine MRI :

Cardiac cine MRI consists of acquiring series of images at multiple time points throughout the cardiac cycle. It thus allows to assess the **dynamic changes** in cardiac geometry over a full cycle. In the left ventricle, for example, this makes it possible to assess the evolution of endocardium and epicardium geometry through the cardiac cycle, and assess the evolution of the cavity volume, wall thickness variations, stroke volume, ejection fractions, etc. [64].

Cine MRI differs from tissue tagging strategies, which measure local tissue deformations [66]. It provides information on the global movement of the tissue.

Cardiac cine MRI can also be coupled with **stress-testing** strategies, in order to unmask underlying pathologies not visible at rest. Protocols are either based on pharmacological agents, such as dobutamine or adenosine, or physical exercises (treadmill, ergometers, handgrip exercises, breathing maneuvers). [54]

Diffusion MRI :

DTI is based on the **random movement of water molecules** in tissue and how this movement is affected by microstructural environment, such as the cellular structure restricting their diffusion along certain directions. The movement of molecules affects the acquired MRI signals. The **signal attenuation** depends both on the direction of the applied magnetic field, and the direction of the molecular movement. [67]

DT images are based on **several acquisitions**, each with different magnetization **directions**, in order to assess the diffusion of water molecules in the tissue in all directions. At least seven acquisitions are required : a non-diffusion weighted image, and 6 different directions. [31]

Due to the challenges involved by cardiac movements, DTI acquisitions were first performed **ex-vivo** [16, 17], and **in-vivo** acquisition protocols were then established [27, 29, 40].

In current research, two main acquisition sequences are used :

- Spin Echo : Spin Echo (SE) sequence is widely used for DT-MRI acquisition [25]. As it is highly sensitive to cardiac movement, motion compensation techniques are required. The first and second order compensation technique is commonly applied and its reliability has been demonstrated comparing in-vivo and ex-vivo acquisitions [68]. Cardiac diffusion data acquired with a spin echo, first- and second-order motion-compensated, were reported to be more precise in midsystolic imaging [69];
- STEAM (Stimulated Echo Acquisition Mode) : STEAM is much less sensitive to cardiac motion but has a lower signal-to-noise ratio than the SE-based method. Due to longer diffusion times, the signal can be affected by tissue strain.

DTI data are recorded in a **diffusion tensor**. Eigenvectors of the tensor describe the direction of the diffusion, and eigenvalues the corresponding intensity of diffusion. The larger the principal eigenvalue, the greater the main directionality of diffusion; and the closer the eigenvalues are to one another, the more isotropic the diffusion. [67]

In the myocardium, **principal direction of diffusion** has been reported to be the cardiac **fiber axis** [70]. Thus, fiber orientation can be obtained with the first eigenvector of the diffusion tensor. As mentioned above, the orientation of this vector can be defined locally by two angles, the helix and the transverse angles. [67]

The **second** and **third** eigenvectors describe the **sheetlets** orientation. [67]

2.4 Myocardium mechanical behavior

Myocardial mechanical behavior is a promising biomarker of cardiotoxicity and heart failure. Its in-vivo estimation can be performed using a finite element model, and this approach will be described in Section 2.4.2. However, ex vivo testing remains essential for understanding and evaluating the passive mechanical response of the myocardium. The insights gained from these experiments are crucial for improving the accuracy of the in-vivo approach.

2.4.1 Ex vivo testing

Ex-vivo testing has led to significant advances in the assessment of mechanical properties of the left ventricular myocardium.

The first **biaxial extension** tests performed on canine myocardial samples [71–73] reported the **non-linear and anisotropic** mechanical behavior of the myocardium. A stiffer behavior in the fiber direction than in the cross-fiber direction was observed, leading to the first

assumptions of **transverse isotropy** [14, 72].

Sommer et al. [74] performed biaxial extension tests with different loading ratios on human myocardium samples. Non-linearity of the myocardium, and twice **stiffer** behavior in mean **fiber direction** than cross-fiber was reported, confirming previous findings. **Viscoelasticity**, hysteresis, and **history-dependent** mechanical behavior were also observed. The authors also highlighted **strain softening** in the myocardium : this irreversible softening of the passive tissue occurred whenever the applied load exceeds its previous maximum value.

However, due to the presence of **shear stress** during diastole, extension tests are not enough to characterize the passive mechanical behavior of the myocardium.

Dokos et al. [4] performed **triaxial simple shear** tests on cubic samples of pig myocardium. The six modes of shearing are illustrated in Figure 2.6. Myocardium mechanical behavior was found to be clearly **orthotropic**. FS and FN shear modes exhibited the highest stress values, indicating a stiffer mechanical response when extending cardiomyocytes. SF and SN modes showed intermediate stress values, and NS and NF modes lowest stress values. Viscoelasticity and hysteresis were also reported. The authors also observed strain softening: myocardium becomes permanently softer after being stretched. They attribute this phenomenon to damage in the extracellular matrix or fibers, or to the rearrangement of fibers and sheetlets.
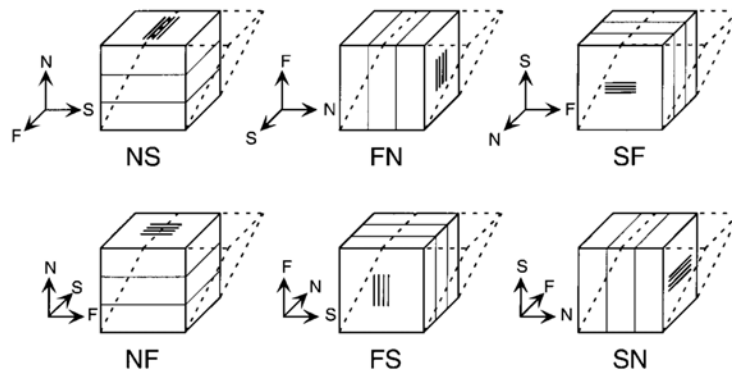
Figure 2.6 Six modes of shear (F: fiber direction, S: sheetlet direction, N = normal to sheetlet) (image taken from [4])

Sommer et al. [74] later performed the same triaxial simple shear tests on cubic samples of human myocardium and reported the same characteristic in mechanical behavior.

Differences within and among hearts :

The mechanical behavior of the myocardium (non-linearity, anisotropy, hysteresis, strain

softening) has been reported to be qualitatively **homogeneous** through left ventricle my-ocardium [73, 74]. While *Novak et al.* [73] described a stiffer behavior close to epicardium and less stiff close to endocardium, *Sommer et al.* [74] observed homogeneous peak stress values through the left ventricle, but significantly lower than in the right ventricle.

Myocardium stiffness has also been reported to be **significantly different** between human, bovine, and canine left ventricle myocardium [74]. Variations in testing protocols may partially account for the observed differences. In addition, although studies agree on a stiffer behavior in the fiber direction than cross fiber one, the ratio of fiber to cross-fiber stiffness has been reported to be different **between species** [75].

Although less pronounced than inter-species mechanical differences, differences were observed between human hearts, and could be due to variations in tissue architecture and collagen density, which naturally change **between individuals** [74].

New testing protocols :

More recently, the coupling of ex-vivo testing with **finite elements simulations** helped to understand new aspect of the myocardium mechanical behavior [76–78].

Avazmohammadi et al. [76] designed optimal deformation paths based on kinematical analysis, in order to accurately apply all deformations to one sample and preserve tissue viability, instead of performing several predefined tests. Finite element simulations were then used to determine the myocardium constitutive law.

Tueni et al. [78] and *McEvoy et al.* [77] used finite elements models (FEM) to understand the micro- and meso-structural causes of the observed macroscopic anisotropic behavior. Indeed, while cardiomyocytes clearly induce a transversely isotropic symmetry, the role of laminar structure and cardiomyocyte varying orientation in the orthotropic behavior remains a topic of discussion. The crucial role of the sheetlets organization in inducing an orthotropic behavior was reported [78]. Moreover, authors highlighted that some level of compressibility in the tissue was necessary to best fit the experimental data.

Indeed, as many other soft biological tissues mainly composed of water, myocardium was initially considered **incompressible** or quasi-incompressible [13, 77]. More recent findings defined the myocardium as being slightly compressible, due to both vasculature compression and the extracellular matrix, which could account for a volume change up to 10% [77, 79].

Transferring ex-vivo properties to the in-vivo context :

As the final objective of this project focuses on the in-vivo mechanical properties of the my-

ocardium, a few **precautions** should be mentioned when transferring ex-vivo experimental data to in-vivo behavior. Firstly, tissue damage from dissection, large deformations, and strain softening may affect stress and strain values compared to what would be observed in-vivo [4, 74]. Besides, residual strain relief due to dissection could also cause some differences [4, 14]. Moreover, due to the size of the sample tested, cardiomyocytes are not perfectly aligned and samples are rarely perfectly homogeneous, which could also affect stress-strain curves.

2.4.2   Left ventricle mechanical model

Numeric mechanical models can be used to estimate in-vivo the left ventricle myocardial passive stiffness.

These models allow for the calculation of mechanical data, such as stress, strain, displacement, energy, etc, in the left ventricle. Achieving this requires to resolve the mechanical equilibrium equations.

The **finite element method** is a numerical resolution method widely used in this context. The method consists of dividing the whole geometry into a mesh of small regions called elements. The equations are then solved within each element. The global behavior is then deduced from the results of each element. [80]

Initial left ventricle finite element models were developed in the 1990s, and only consider **passive behavior** of the tissue. Their geometry was a **simplified geometry** of the left ventricle, such as a truncated ellipsoid [2], or was based on histological data [81].

Patient-specific geometry was then implemented, based on MRI acquisitions [5,8]. **Active behavior** of the tissue was also added [82].

To better account for the **blood pressure** acting on the endocardial surface, some models were coupled with lumped-parameter representation of the circulatory system [62, 83] or fluid-structure interaction models were developed [84].

Electromechanical models were also developed. The coupling between electrophysiological and mechanical equations was implemented to reproduce cardiac cycle [85].

Some models simultaneously include **mechanical, electrical, and blood circulatory** governing equations in the left ventricle [86].

Models have been extended to **biventricular**, and even 4-chambers numeric models of the heart. The Living Heart Project is a 4-chambers electro-mechanical model coupled to a closed loop circulatory system [87].

In this project, we focus on modeling the **passive mechanical behavior of the left ventricle with the finite element method**. The following sections describe the models basic characteristics.

2.4.2.1   Geometry and boundaries condition

Geometry :

The **truncated ellipsoid**, considered an ideal geometry of the left ventricle, has been widely used in both older left ventricle models, and more recent models which focus on studying the impact of different parameters on the left ventricle behavior [88–93].

Patient-specific geometries, based on either cine-MRI acquisition [5,9,19,20,61,83,94–98]. Tag MRI [8,99], computed tomography [18,62], or 3D-echocardiography [100,101] have also been used. The general meshing principle remains the same regardless of the acquisition method [102] : the left ventricle endocardium and epicardium are first **segmented** ; then, a template mesh is wrapped to match the segmented contours. Thus, a **patient-specific mesh** of the left ventricle is obtained.

Loading conditions :

In case of stiffness estimation, finite element models compare two states : either the end of systole or the diastasis, considered as the **"reference" state**, with the **end of diastole**. Although the pressure in the reference state is often assumed to be **zero**, the pressure applied at the end of diastole is chosen to reflect the blood pressure at this time of the cardiac cycle. In most of the models, this pressure is **uniformly** applied to the surface.

Its value can be obtain by **catheterization**. This technique allows for direct measurement of pressure inside the ventricle, and the pressure values can be applied in the finite element model [5,8,100,103]. However, this is an invasive technique, and is not always feasible. This is why, some have chosen to **apply a standard value** of end-diastolic pressure, generally around 1kPa, that is 8mmHg [20,88,89,92,93,95,98].

In order to estimate a patient-specific pressure, some finite element models have been coupled to a **closed loop circulatory model** [18,83]. These circulatory models are based on the Windkessel model, and relate pressure, volume, compliance, and resistance in the circulatory system.

CircAdapt [104] is a lumped parameter model for the heart and circulatory system. This model includes adaptation rules to provide patient-specific data. It has been used to estimate patient-specific end diastolic pressure, thanks to an optimization of the most influential

parameters of the model [21]

Boundaries conditions :

The finite element model must be constrained to prevent **rigid body motion**. Existing models employ various strategies :

- Constrain displacement and rotation of all basal nodes in all directions [7]
- Constrain vertical translation of basal nodes (either fixed [98] or match MRI displacement [20]), and all translation of epicardial basal nodes [98]
- Constrain basal nodes and apex point to match displacement observed on MRI [5, 9]
- Constrain basal nodes with linear springs [86]

2.4.2.2 Material constituntive law

Continuum mechanics :

To facilitate understanding of myocardial mechanical behavior definition, a brief overview of **continuum mechanics** is first presented below :

- Let X be the position of a particle in the reference configuration and $x(X, t)$ its position in the deformed configuration.
- The deformation gradient tensor $F = \nabla x(X, t)$ describes this variation of position. The Green-Lagrange strain tensor $E = \frac{1}{2}(F^T F - I)$ quantifies the deformation of the material between its deformed state and the reference configuration.
- The second Piola Kirchhoff stress tensor, S, describes internal forces acting in the material with respect to the undeformed geometry. The Cauchy stress tensor, $\sigma = FSF^T$, describes internal forces acting in the material with respect to the actual geometry.
- The **energy density function**, ψ, relates stress and strain values : $S = \frac{\partial \psi}{\partial E}$. This constitutive law dictates the material mechanical response.

In this section, different **constitutive laws** used to model the mechanical behavior of the myocardium will be detailed.

Different constitutive laws :

The first models were linear and isotropic, which proved to be inadequate, as previously discussed [13]. **Transverse isotropy** was then implemented, with invariant-based [105] or Green-Lagrange strain based [14] constitutive laws. **Orthotropic laws** were then implemented [72, 106, 107]. Structural laws, which separates the different components of the myocardium and their interaction, have also been developed [78, 108, 109]. When comparing

existing constitutive laws, it is important to note that they are not all suited for the same purposes : some are effective in describing the mechanical response of the material, but may be not ideal for estimation of the constitutive law's parameters [110].

Viscoelasticity is often neglected in existing models, which should not be a problem at normal cardiac rate [13].

Compressibility of the myocardium has been shown to have a local impact on mechanical behavior [77, 78]. However, it has been reported to have a negligible impact on the global behavior of the left ventricle compared to other material parameters [101]. Compressibility has been neglected in most studies, except a few of them [86, 88].

In the context of mechanical parameter estimation, two main constitutive laws are commonly used : the one described by ***Guccione et al.*** [14], and the one reported by ***Holzapfel and Ogden*** [13].

Fung-type Guccione constitutive law :

The constitutive law described by *Guccione et al.* [14], is a Fung-type strain energy density function based on the Green-Lagrange strain tensor :

$$\psi = \frac{1}{2}C\left(e^Q - 1\right)$$

with

$$\begin{aligned}
Q = {} & b_1 E_{ff}^2 + b_2 E_{ss}^2 + b_3 E_{nn}^2 \\
& + 2b_4 E_{ff}E_{ss} + 2b_5 E_{ss}E_{nn} + 2b_6 E_{ff}E_{nn} \\
& + b_7(E_{fs}^2 + E_{sf}^2) + b_8(E_{sn}^2 + E_{ns}^2) + b_9(E_{fn}^2 + E_{nf}^2)
\end{aligned}$$

In case of **transverse isotropy**, with fiber axis being the principal direction, the relation simplifies as follow :

$$Q = b_f E_{ff}^2 + b_t(E_{ss}^2 + E_{nn}^2 + 2E_{sn}^2) + 2b_{ft}(E_{fs}^2 + E_{fn}^2)$$

with E being Green-Lagrange strain tensor, f the fiber direction, s the sheetlet direction, and n the sheetlet normal direction. C is the **global stiffness** paramater.

Stiffness in the fiber direction, cross-fiber direction and under shear, are related respectively to b_f, b_t and b_{ft}.

This constitutive law has been widely used to identify cardiac mechanical parameters in animal hearts [8, 75, 99, 103, 111] as well as in healthy and cardiopathological human hearts [5, 7, 9, 61].

Invariants based Holzapfel constitutive law :

The constitutive law described by *Holzapfel and Ogden* [13], is an orthotropic invariants based constitutive law :

$$\Psi = \frac{a}{2b} \exp[b(I_1 - 3)] + \sum_{i=f,s} \frac{a_i}{2b_i} \left\{ \exp\left[b_i(I_{4i} - 1)^2 \right] - 1 \right\} + \frac{a_{fs}}{2b_{fs}} \left[\exp(b_{fs}I_{8fs}^2) - 1 \right]$$

In this equation, I_j are the Cauchy-Green invariants : I_1 is the isotropic term, I_{4f} and I_{4s} transversely isotropic terms, related respectively to the behavior in the fiber and sheetlet directions, and I_{8fs} the orthotropic term related to shear in the sheetlet plane. The a_i and b_i terms are the 8 material parameters.

This constitutive law has also been widely used for myocardium modeling [95, 98].

2.4.2.3   Fiber orientation

The constitutive laws introduced above depend on the **local fiber orientation**. It is therefore necessary to define this orientation in the model. Local orientation needs to be define for each element of the mesh.

They are two type of methods to implement fiber orientation in the model :

- **Ruled-based methods** : fiber orientation is implemented through a mathematical description of the variation in fibers angles (HA, TA, E2A) across the myocardium.
- **DTI based methods** : DTI data are integrated to the finite element model.

Rule-based methods :

Due to the challenges of DTI acquisition, rule-based methods have been commonly used.

The most commonly used description of the myofibers architecture is the **helical structure** based on *Streeter et al.* histological data [15]. The **helix angle** is **homogeneous** from base to apex and **varies linearly from about 60° at the endocardium to about −60° at the epicardium**, and **transverse angle** is set to **zero** in the whole ventricle. Helix angle values at the endocardium and epicardium can vary a little between models, but remains between 60° and 90° at endocardium, and between −60° and −45° at epicardium. [5,7,9,32,90,95,100]

The main challenge in the implementation of this architecture is to accurately determine the **transmural distance** at each element of the mesh. Computing this distance only based on the minimal distance between endocardium and epicardium has been shown to be inappropriate, and several methods have been developed to improve this calculation. Laplace-Dirichlet rule-based algorithm [112] is the most commonly used, but sketch-based method [113] or Poisson interpolation algorithm [114] are other examples.

Rather than prescribing fiber orientation, some researchers have based the fiber orientation on an optimization process aiming at strain homogenization [91] (later employed by [88,93,115]).

DTI based methods :

Due to challenges of in-vivo acquisitions, **ex-vivo** diffusion data have been more commonly used, in either animal based models [18, 99, 103] and human based models [8, 19, 62]. More recently, animal [66] and human [20] **in-vivo** diffusion data have been integrated into finite element models. In-vivo, the acquisition of a sufficient number of slices and of high-quality data remains a significant challenge.

Following acquisition, the diffusion data need to be integrated into the finite element model. **Wrapping DTI data** onto the model geometry is challenging because the data consist of tensors, which include an orientation within a local coordinate system. As a result, they cannot be simply repositioned to match the geometry [17]. When integrating DTI data into the left ventricular geometry, each tensor must be **reoriented** to remain consistent with the underlying anatomical structure [116]. To achieve this, two different strategies have been used [116] :

- the finite strain : it consists of applying global rotation to tensors to make them follow the general movement of the image.
- the preservation of principal direction : it consists of reorienting tensors according to the cardiac fibers deformation in the tissue.

The second challenge is the **interpolation of missing data**. Indeed, especially in in-vivo acquisitions, difficulties mentioned above prevent a complete acquisition in the whole ventricle, and missing data need to be interpolated. Different strategies have been used : weighted average according to position in the left ventricle [27], adaptation of the Laplace-Dirichlet rule-based algorithm [112] to fit diffusion data [117] , tri-cubic Hermite interpolation [8, 20], b-splines interpolation [19]. More recently, deep learning methods have been used to learn from large databases in order to complete the diffusion data, or even to estimate directions directly from raw data [118].

2.4.2.4   Parameters estimation

Estimating mechanical properties with a finite element model is based on the principle of **inverse optimization**. We know the geometry and constraints (boundaries and loading conditions) of the mechanical model. Thank to MRI segmentation, we also know the solution we seek to obtain at the end of the simulation. The objective is to **estimate the mechanical parameters of the constitutive law that lead to this solution**.

The process of the inverse optimization starts with an initial guess of the mechanical parameters, and first computation is performed with this guess. The difference between the simulation result and the result we seek to obtain is evaluated, and the parameters are adjusted accordingly. The calculations are performed with these new parameters and the new solution is evaluated. These steps are repeated until the mechanical parameters have converged.

This process requires an evaluation criterion of the difference between end-diastolic simulation and MRI. The **objective function** evaluates this difference, and is minimized during the optimization process. In existing studies, objective function are based on different criteria : the position of endocardium and epicardium nodes [5, 8, 20] ; the strain in the tissue [96, 119] sometimes combine with end-diastolic ventricle volume [120] ; the end-diastolic pressure-volume relationship [7, 62, 83] ; the external work and internal energy [9]

This optimization process can be used to estimate **one or several mechanical parameters** of the constitutive law. Models that use Holzapfel's invariant-based constitutive law generally estimate the full set of mechanical parameters [95, 97]. In contrast, models employing the Fung-type law typically follow one of three strategies : estimating all parameters [8, 14, 99, 103], estimating the global stiffness and one of the anisotropic parameters [7] or the sum of them [5, 20], or estimating C alone [61].

However, some mechanical parameters could be coupled [99]. When estimating several parameters the solution may **not be unique**, as multiple parameter combinations can lead to similar results [5].

As part of the optimization procedure, a step can be added to first estimate the **residual tension** in the myocardium [5]. Indeed, the residual tension generated by the contraction of cardiomyocytes affects the stiffness of the tissue, but is neglected in most studies.

The **unloaded geometry** can also be estimated as a first step of the optimization process [62]. Indeed, reference geometry is considered to be the zero-pressure geometry in most studies, which is an approximation.

The inverse optimization process can also be used to estimate **active mechanical param-**

eters, using an adapted constitutive law and systolic MRI data [61].

2.4.2.5 Sensitivity to model inputs

Stiffness estimation depends on **several model inputs** : the reference geometry, the constitutive law, the fiber orientation, the loading and boundaries conditions.

Some studies have focused on the impact of these inputs on the **left ventricle mechanics** [90,97,98,101]. Different outputs are generally been studied : the left ventricle cavity volume, apex lengthening and rotation, stress and strain distribution in the myocardium, and systolic function [121]. Thus, the impact of fiber orientation [2, 89, 90, 97, 98, 101, 122], left ventricle geometry [89], mechanical interaction of the right ventricle [97], and boundaries conditions [123] have been assessed.

Only a few studies have investigated the impact of these inputs on the **stiffness estimation**. *Guccione et al.* [14] reported differences in the estimation of the four parameters of the Fung-type law for a few different fibers architecture. *Nikou et al.* [122] and *Palit et al.* [124] studied the impact of the fiber orientation in the estimation of the eight parameters of Holzapfel's invariant-based constitutive law. *Palit et al.* [124] also investigated the impact of the left ventricle geometry and end-diastolic pressure on this estimation. *Kolawole et al.* [20] evaluated the impact of the fiber orientation and end-diastolic pressure on the estimation of two parameters of the Fung-type law (the global stiffness and the sum of anisotropic mechanical parameters).

The limited studies in this area highlight the **need for further investigation**. Understanding the impact of input parameters on model outcomes is essential for developing models that are both accurate and efficient, without unnecessary complexity.

2.5 Key points

A summary of the literature review is provided below to outline the key aspects pertinent to this work :

- Current diagnostic tools have limitations regarding the early detection of doxorubicine-induced cardiotoxicity, and more broadly, heart failure. Studies in the field have highlighted the promising potential of estimating the **left ventricle myocardial passive stiffness**.

- **Finite element models** are efficient tools for non-invasive estimation of myocardium mechanical properties. The estimation is based on inverse optimization process.

- Implementation of finite element models requires the definition of the left ventricle geometry, myocardium constitutive law, myofiber orientation, loading and boundaries conditions.

- Ex-vivo tests have helped define the **myocardium constitutive law**. It should be modeled as a non-linear anisotropic material. The transversely-isotropic Fung-type law described by *Guccione et al.* [14] has been widely used in the context of mechanical parameter estimation. It includes a global stiffness parameter, and three anisotropic parameters. The estimation of all parameters may lead to non-uniqueness of the solution.

- DTI has helped understand the **myofiber architecture**, in both ex-vivo and in-vivo acquisitions. DTI data can now be integrated in patient-specific left ventricle model, but both acquisition and integration in the model are challenging. In the absence of patient-specific orientation data, the helical structure reported by *Streeter et al.* [15] has been widely used.

- Models **inputs** have been shown to have impact on the left ventricle mechanics. Fewer studies have focused on the **impact of these parameters on myocardium stiffness estimation**. It is nonetheless crucial for assessing the precision requirements in model implementation.

2.6 Overview of the preceding student's work

Given that this study continues Franck Mahalatchimy's master's research [21], the literature review concludes with a brief summary of his project and the developments that have followed.

Franck Mahalatchimy developed a framework to estimate passive stiffness in patient-specific left ventricle finite element models, with cardiac MRI collected at rest and during exercise. The method was applied to 5 healthy subjects.

A brief overview of this work is provided below; for further details, please refer to [21] :

- Cardiac cine MR images were acquired at rest, during isometric effort, and during exercise using an ergometer.
- The endocardium and epicardium contours were semi-automatically segmented on short- and long-axis views, using SEGMENT software. The curve of the left ventricle volume was used to determine the diastasis and end-diastole phases. Segmented points coordinates were imported in MATLAB software.

- The template mesh, a truncated ellipsoid was created on Abaqus software. Mesh nodes coordinates were imported in MATLAB software.

- A registration algorithm based on translations and rotations is applied to the segmentation points to align them with the configuration of the template mesh nodes. Control points are chosen among segmented points and mesh nodes. A 3D thin plate spline warping algorithm allows estimating the displacement field between the segmented control points and mesh control points. The displacement field is applied to all nodes of the mesh. The patient-specific mesh is thus obtained.

- The finite element model is built with Abaqus software, and includes the aforementioned patient-specific mesh. A transversely-isotropic Fung-type law is implemented, with mechanical parameters taken from *Xi et al.* [5]. Regarding the material local orientation, a linear transmural variation, from $60°$ at the endocardium to $-60°$ at the epicardium is implemented. All basal nodes are fixed in all direction.

- Concerning the loading pressure, CircAdapt model [104] was used to estimate end-diastolic pressure in the left ventricle. The most influential parameters of this model were optimized using cardiac flow values derived from segmentation and pressure values derived from blood pressure measurements. This optimization is based on minimizing the difference between the curve of the left ventricle volume in the segmentation and from CircAdapt simulation. The obtained value of end-diastolic pressure obtained is applied uniformly at the endocardium surface of the finite element model.

- The target displacement field is estimated thanks to segmented contours of endocardium and epicardium, and interpolated to the nodes of these surfaces in the finite element model.

- The optimization is based on minimizing the quadratic difference between this target displacement field, and the displacement field from the simulation. The optimisation process is implemented with MATLAB software, using *fminsearch* function.

In the current work, this framework is kept identical, with adjustment of some steps. This framework is summarized in Figure 2.7. Segmentation data, loading pressure and optimization algorithm are kept identical. The template mesh, morphing algorithm, fiber orientation implementation, and displacement field estimation are adjusted.
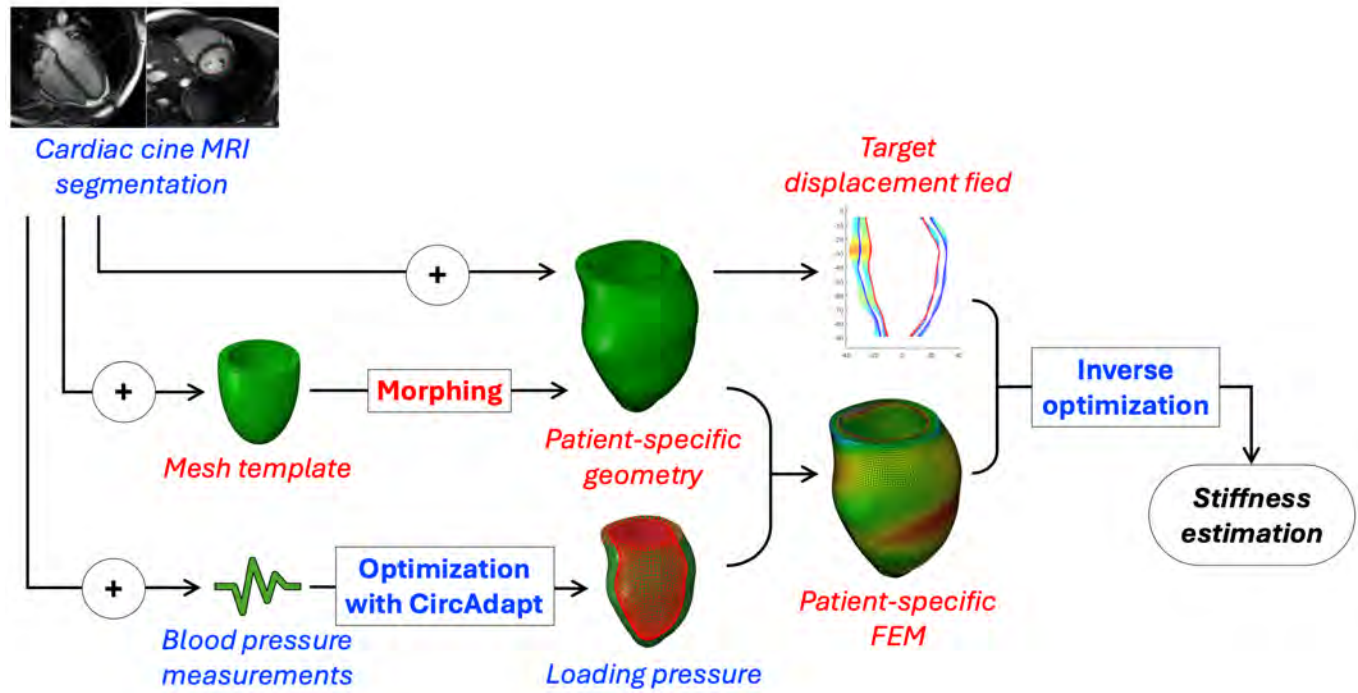
Figure 2.7 Framework for stiffness estimation (*blue : kept identical ; red : adjusted*)

CHAPTER 3   COMPARING FUNG-TYPE PASSIVE LAW PARAMETERS FOR LEFT VENTRICLE MYOCARDIAL STIFFNESS ESTIMATION

3.1   Introduction

As outlined in Chapter 2, left ventricle myocardial stiffness is a promising biomarker for the early detection of cardiotoxicity and heart failure. Finite element models, used for inverse optimization of in-vivo mechanical parameters, are efficient tools for this stiffness estimation.

Estimation relies on the definition of the myocardium constitutive law, and the selection of one or several parameters of the law to be estimated.

The transversely isotropic Fung-type constitutive law described by *Guccione et al.* [14] has been widely in this context. The strain energy density function is written :

$$\psi = \frac{1}{2}C\left(e^Q - 1\right)$$

with

$$Q = b_f E_{ff}^2 + b_t(E_{ss}^2 + E_{nn}^2 + 2E_{sn}^2) + 2b_{ft}(E_{fs}^2 + E_{fn}^2)$$

In this constitutive law, C is the global stiffness of the tissue, and b_f, b_t and b_{ft} are the three anisotropy parameters, respectively stiffness in the fiber direction, cross-fiber direction and under shear.

Previous studies have highlighted the issue of non-uniqueness in estimating all four parameters [5, 8].

It has been shown that the global stiffness C has by far the largest impact on left ventricle behavior, relative to the three anisotropy material parameters b_f, b_t and b_{ft} [101].

Choosing C value as the biomarker of interest, and fixing the other three anisotropy parameters to standard values would allow a comparison between patients, and the definition of standard and pathological values. However, the set of three parameters varies significantly across studies, complicating the selection of an optimal parameter set.

The aim of this Chapter is to understand and evaluate the impact of this set of three parameters on global stiffness estimation. This can be divided into three specific sub-objectives.

1. Study the impact of each parameter of the set
2. Compare existing parameter sets of the left ventricle myocardial passive law
3. Choose a parameter set reported in the literature

3.2 Methods

The analysis is conducted in three steps :

- Biaxial and shear tests are simulated using a finite element model, to understand the impact of each parameter on the local tissue behavior and to compare parameter sets reported in the literature.
- Then, since stiffness optimization is based on ventricle displacement, the impact of these parameters on the displacement of an ideal left ventricle finite element model is studied.
- Finally, the impact of these parameter sets on stiffness estimation is evaluated with five patient-specific finite element models.

The aim of these three steps is to assess the impact of the mechanical parameters on global stiffness estimation and understand its underlying causes.

Finite element models are implemened in Abaqus/Standard (v2022) [125]. Studies are conducted with static analysis using the default direct solver, with the full Newton solution technique and geometric nonlinearity enabled. The time incrementation is automatic. A maximum time increment of 0.1 is imposed for extension and shear test (see Section 3.2.2). The models are discretized with linear hybrid hexahedral elements (C3D8H).

3.2.1 Myocardial constitutive law

The left ventricle myocardium is assumed to be homogeneous, hyper-elastic, anisotropic, and incompressible. It is modeled using the Fung-type transversely isotropic constitutive equation described by *Guccione et al.* [14].

This law is implemented using the Fung-type anisotropic low in Abaqus software [125]. In Abaqus, for the incompressible case, the law is expressed as followed [126] :

$$\psi = \frac{1}{2} C \left(e^Q - 1 \right)$$

with

$$Q = \underline{\underline{E}} : \underline{\underline{\underline{B}}} : \underline{\underline{E}} = E_{ij} B_{ijkl} E_{kl}$$

where B is a dimensionless symmetric fourth-order tensor of anisotropic material constants and E the Green-Lagrange strain tensor. Due to symmetry of these tensors, we can use Kelvin representation to write the expression of Q as follows [94] :

$$Q = E \cdot B \cdot E^T$$

with B being symmetric, and $E = \begin{bmatrix} E_{11} & E_{22} & E_{33} & \sqrt{2}E_{12} & \sqrt{2}E_{13} & \sqrt{2}E_{23} \end{bmatrix}$.

In case of transverse isotropy, with the first direction being the principal axis, the relation simplifies as follows [94] :

$$
B = \begin{bmatrix}
b_f & 0 & 0 & 0 & 0 & 0 \\
0 & b_t & 0 & 0 & 0 & 0 \\
0 & 0 & b_t & 0 & 0 & 0 \\
0 & 0 & 0 & b_{ft} & 0 & 0 \\
0 & 0 & 0 & 0 & b_{ft} & 0 \\
0 & 0 & 0 & 0 & 0 & b_t
\end{bmatrix}
$$

Assuming that the fiber axis f is the principal axis of symmetry, and the sheetlet direction s and the sheetlet normal direction n are orthogonal vectors in the normal plane, Q can be written as [94] :

$$
Q = b_f E_{ff}^2 + b_t (E_{ss}^2 + E_{nn}^2 + 2E_{sn}^2) + 2b_{ft}(E_{fs}^2 + E_{fn}^2)
$$

This last formulation is commonly mentioned in the literature. The mechanical parameters in Abaqus are thus chosen as follows : $b_{1111} = b_f$, $b_{2222} = b_{3333} = b_t$, $b_{1212} = b_{1313} = \frac{b_{ft}}{2}$, and $b_{2323} = \frac{b_t}{2}$, all other components being zero.

A total of 14 parameter sets reported in the literature have been selected, and summarized in Table 3.1.

In the finite element models presented in the following, two types of studies are conducted :

- Sensitivity study : Mechanical parameters are set according to the values reported by *Xi et al.* [5], which are considered as the "reference" simulation. One parameter is then successively set to the minimum, first quartile, median, last quartile and maximum of values reported in the literature (lines 15 to 19 of Table 3.1), in order to independently study the impact of each parameter.
- Comparative study : Mechanical parameters are based on a set of values reported in the literature (lines 1 to 14 of Table 3.1), in order to compare existing set of parameters with each other.

Table 3.1 List of mechanical parameters studied

Authors	Species	C	b_f	b_t	b_{ft}
Augenstein et al., 2005 [99]	pig	3.00	11.09	1.76	10.00
Genet et al., 2014 [7]	human	0.12	14.40	5.76	10.08
Costa et al., 1996 [127]	dog	0.88	18.48	3.58	1.63
Nasopoulou et al., 2017 [9]	human	1.70	8.28	3.00	3.75
Okamoto et al., 2000 [128]	dog	0.51	67.07	24.16	21.60
Omens et al., 1993 [75]	rat	2.20	9.20	2.00	3.70
Omens et al., 1993 [75]	dog	2.40	26.70	2.00	14.70
Osnes and Sundnes, 2012 [90]	dog	1.10	6.60	4.00	2.60
Vetter and McCulloch, 2000 [119]	rabbit	1.76	50.00	5.00	1.63
Walker et al., 2005 [103]	sheep	0.23	49.25	19.25	17.44
Wang et al., 2009 [8]	dog	1.66	14.31	4.49	0.76
Wang et al., 2013 [61]	human	3.60	8.60	3.70	25.80
Xi et al., 2013 [5]	human	2.00	19.13	10.67	12.76
Zhang et al., 2021 [6]	human	0.01	20.28	7.46	8.72
Minimum		0.01	6.60	1.76	0.76
First quartile		0.6	9.67	3.15	2.88
Median		1.68	16.44	4.25	9.36
Third quartile		2.15	25.10	7.04	14.22
Maximum		3.60	67.07	24.16	25.80

3.2.2 Biaxial extension and triaxial simple shear tests

The biaxial extension and triaxial simple shear tests conducted by *Sommer et al.* [74] are reproduced numerically with finite element models in Abaqus/Standard (v2022) [125], according to the details provided in the introduction of this chapter.

3.2.2.1 Biaxial extension tests

Sommer et al. [74] specimen were thin squared specimen of myocardium, of average dimension $12.5 \times 12.5 \times 2.3$ *mm*. One side was aligned with the mean-fiber direction and the other in the cross-fiber direction. After preconditioning cycles, different stretches were applied consecutively until a final stretch of 1.10. Different ratios of fiber and cross-fiber were applied. Further details about the experimental protocol can be found in [74].

This study focuses on the 1:1 ratio tests, which means a stretch of 1.10 in both the fiber and the cross-fiber direction. Due to the symmetry of the boundary conditions, only a quarter of *Sommer et al.* [74] specimen is modeled. The geometry is a parallepiped of $12.5 \times 12.5 \times 2.3$ *mm*. A mesh convergence is performed to ensure maximum stress and strain deviation with finer meshes remains below 1%. The final mesh is composed of 200 elements. Stretch is simulated by imposing a displacement of 1.25 *mm* to two adjacent lateral faces in the direction of the surface normal, and a zero displacement of the two other adjacent lateral faces in the the surface normal direction. The principal material direction, representing the fiber orientation, is aligned with one of the stretch directions.

The geometry and boundary conditions are illustrated in Table 3.2, along with a summary of all model-related information.

The values of stress σ_{11} and σ_{22}, and logarithmic strain LE_{11} and LE_{22} are extracted from simulation results at each time increment. The stretches $\lambda_{11} = exp(LE_{11})$ and $\lambda_{22} = exp(LE_{22})$ [126] are computed to plot stress-stretch curves and compare with stress values reported by *Sommer et al.* [74].

3.2.2.2   Triaxial simple shear tests

Sommer et al. [74] specimen were cubic specimen of myocardium, of average dimension $4 \times 4 \times 4$ *mm*. Using the coordinate system introduced in Chapter 2, F being the fiber direction, S the sheetlet direction, and N sheetlet normal direction, the specimen sides were aligned with these directions. Preconditioning cycles, and different consecutive shear were applied. Six different modes of shearing were applied, and have been introduced in Chapter 2 (see Figure 2.6) Further details about the experimental protocol can be found in [74].

The finite element model is a cube of $4 \times 4 \times 4$ *mm*, composed of 8000 mesh elements. A mesh convergence is performed to ensure that, compared to finer meshes, the deviation of the average shear stress on the moving surface remains below 1%. In addition, as a region of high stress is observed at the edges of the moving surface, an additional convergence criterion is introduced : this region must extend over less than 5% of the total distance. Material orientation is defined so that one face is parallel to fiber direction, one to sheetlet direction, and one to sheetlet normal direction. Shear is simulated by imposing displacement on two opposite faces : a displacement of 1.5 *mm* is imposed on one, while the other remains fixed. The six different shear modes (FS, SF, FN, NF, SN, NS) are modeled.

The geometry and boundary conditions are illustrated in Table 3.2.

The values of displacement U_i and average stress σ_{ji} on the moving surface are extracted from

simulation results at each time increment. The "amount of shear" as defined by *Sommer et al.* [74] is computed as $\frac{U_i}{L}$ with $L = 4\ mm$ being the length of each edge of the cube. Shear stress-strain curves are then plotted.

3.2.2.3 Results analysis

For both biaxial extension and triaxial simple shear tests, stress-strain curve are plotted. The root mean squared error (RMSE) between the curves obtained from the simulation and the measurements by *Sommer et al.* [74] are computed. The convexity of stress-strain curves is quantified by averaging the second derivative of the normalized curve. All calculations are performed using Python (v3.11.9).

3.2.3 Passive inflation of an ideal left ventricle geometry

As the stiffness estimation relies on the displacement of left-ventricle, the impact of the mechanical parameters on this displacement was investigated. To prevent the geometry from affecting the results, it was decided to conduct this analysis with an ideal left ventricle geometry.

The finite element model is built in Abaqus/Standard (v2022) [125], according to the details provided in the introduction of this chapter.
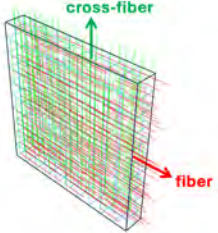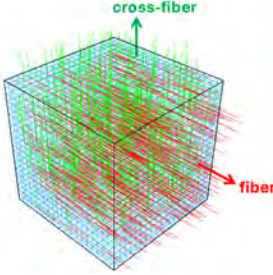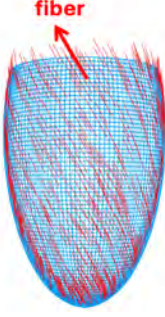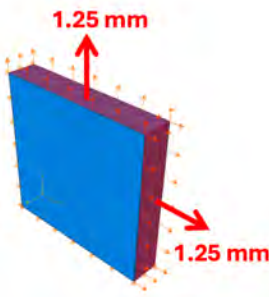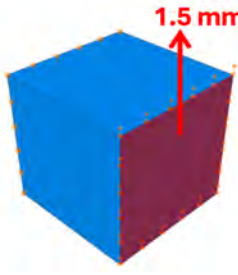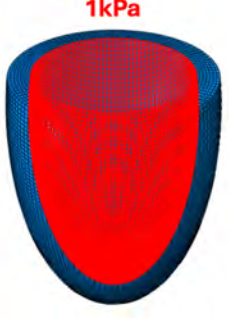
The geometry is a truncated ellipsoid, with a minor axis of length 50 mm, apex-to-base distance 80 mm, and thickness 7 mm. The truncation is 20 mm above minor axis. A mesh convergence is performed, to ensure that within 90% of the height, excluding the basal region, maximum stress and strain in the fiber direction deviate less than 2% with thinner meshes. The geometry is finally discretized in 51569 elements.

Fiber orientation is implemented by assigning a local coordinate system to each element of the mesh. The principal direction models the fiber orientation, and the second direction the sheetlet plane. The mesh is composed of 7 layers, each with a respective helix angle of 60°, 40°, 20°, 0°, −20°, −40°, −60° from endocardium to epicardium. The transverse angle is zero throughout the model.

Zero displacement is imposed on basal nodes, and a $1kPa$ pressure is applied on endocardial surface. The geometry and load are illustrated in Table 3.2.

At the end of the simulation, the maximum displacement in the model, and coordinates of each nodes, are extracted. The endocardial cavity volume is computed using Python Convex Hull algorithm with nodes coordinates.

Table 3.2 Details of the finite element models

	Biaxial extension	**Shear**	**Ideal left ventricle geometry**
Geometry	Parallepiped $(12.5 \times 12.5 \times 2.3\ mm)$	Cube $(4 \times 4 \times 4\ mm)$	Truncated ellipsoid (Minor axis : $50mm$; Apex-to-base : $80mm$; Thickness : $7mm$)
Mesh	200 C3D8H elements	800 C3D8H elements	51569 C3D8H elements
Fiber orientation	Fibers aligned with one side of the square, cross-fiber with the other side of the square	One face parallel to fiber direction, one to sheetlet direction, one to sheetlet normal direction	Linear transmural variation of helix angle from 60° at endocardium to −60° at epicardium
Load and boundaries conditions			

3.2.4 Patient-specific stiffness estimation

Patient-specific stiffness estimation is based on F. Mahalatchimy Master's thesis [21], and has been described in Section 2.6.

In this first study (Section 3), the framework developed by F. Mahalatchimy is kept identical. Only the mechanical parameters of the Abaqus Fung-type constitutive law are modified, based

on the values provided in Section 3.2.1.

For the 6 available subjects, patient-specific stiffness is estimated with the different set of mechanical parameters. Stiffness estimation with different mechanical parameter sets were compared using a Friedman ANOVA [129] using a significance level of $p = 0.1$. Both estimated stiffness and residual error (objective function at the end of the optimization) were compared.

3.3 Results

This section reports the results obtained for the three studies. First, biaxial extension and triaxial simple shear tests results are presented, then results of passive inflation of an ideal left ventricle geometry, and finally patient specific stiffness estimations.

The results are presented sequentially for the two axis of analysis : sensitivity study (a single parameter varying step by step from the reference value, which corresponds to the parameters reported by *Xi et al.* [5]), and comparative study (comparison of full sets of parameters reported in the literature).

3.3.1 Biaxial extension and triaxial simple shear tests

3.3.1.1 Sensitivity study

Figure 3.1 shows the stress-stretch curves resulting from **biaxial extension** tests with *Xi et al.* [5] except one parameter varying as described in Section 3.2.1.

At fixed strain, both stresses in fiber and cross-fiber direction are directly proportional to C.

An increase in b_f (respectively b_t) of 164.1% (172.8%) leads to an increase of 161.7% (124.9%) of the stress in the fiber direction at 1.1 stretch, and of 22.8% (177.1%) of the stress in the cross-fiber direction at 1.1 stretch.

Increasing b_f and b_t contribute to the stress-stretch curve inflexion. In the fiber direction, increasing b_f from reference simulation ($b_f = 19.13$) to the maximum value ($b_f = 67.07$) increases the curvature from $114.8 kPa$ to $227.35 kPa$. In the cross-fiber direction, increasing b_t from reference simulation ($b_t = 10.67$) to the maximum value ($b_t = 24.16$) increases the curvature from $100.0 kPa$ to $182.2 kPa$.

The parameter b_{ft} has no impact on extension stresses in both fiber and cross-fiber direction.
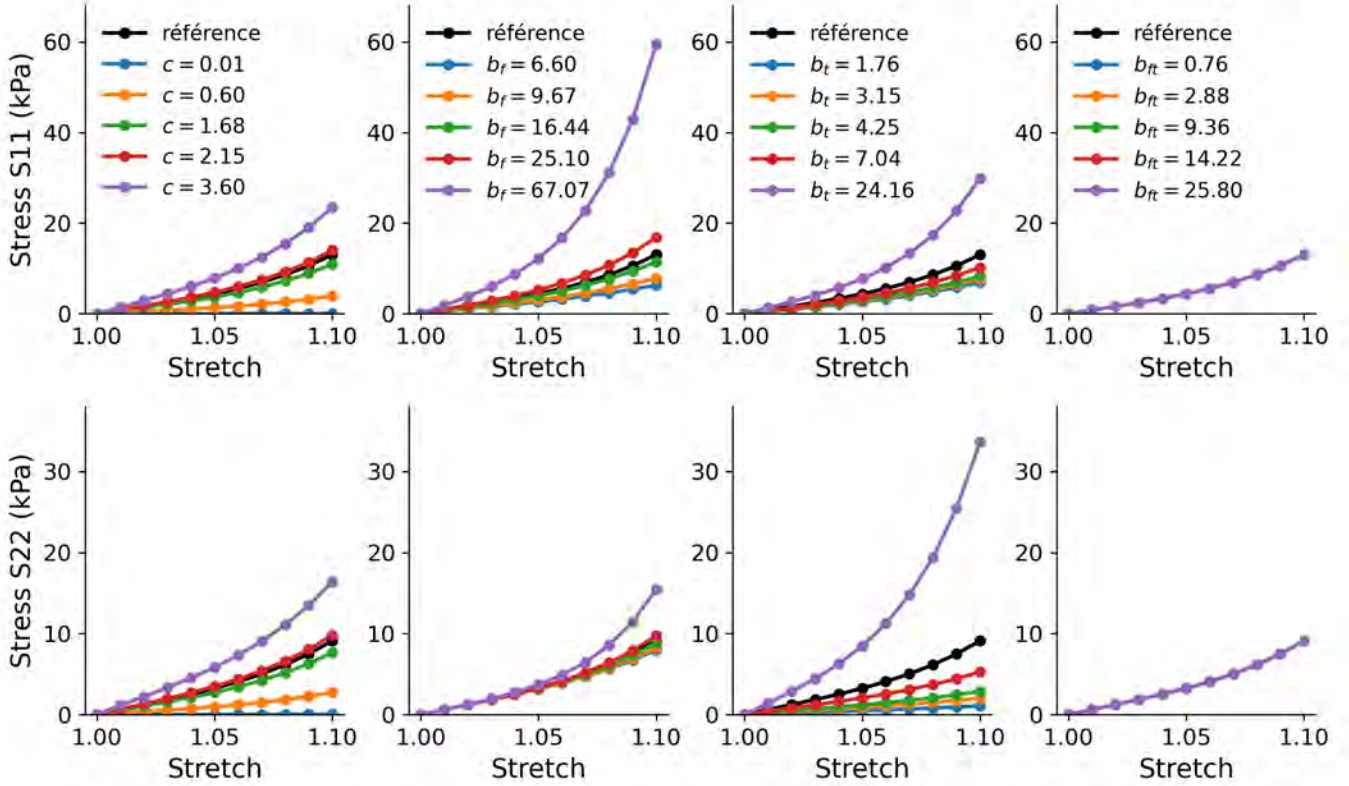
Figure 3.1 Stress-stretch curves of biaxial extension tests in the sensitive study

Convergence issues made it difficult to perform the complete sensitivity study for **triaxial simple shear** tests. Nevertheless, it can be observed that shear stress in FS, FN, SF, NF are impacted by b_{ft} parameter, and that these stresses increase as b_{ft} increase. Shear stresses in SN and NS mode increase when b_t increases. These results are illustrated in Appendix A.

3.3.1.2 Comparative study

Figure 3.2 shows the stress-stretch curves resulting from **biaxial extension** tests with different parameter sets reported in the literature. The upper row corresponds to parameter sets obtained from animal data, while the lower row corresponds to those derived from human data.
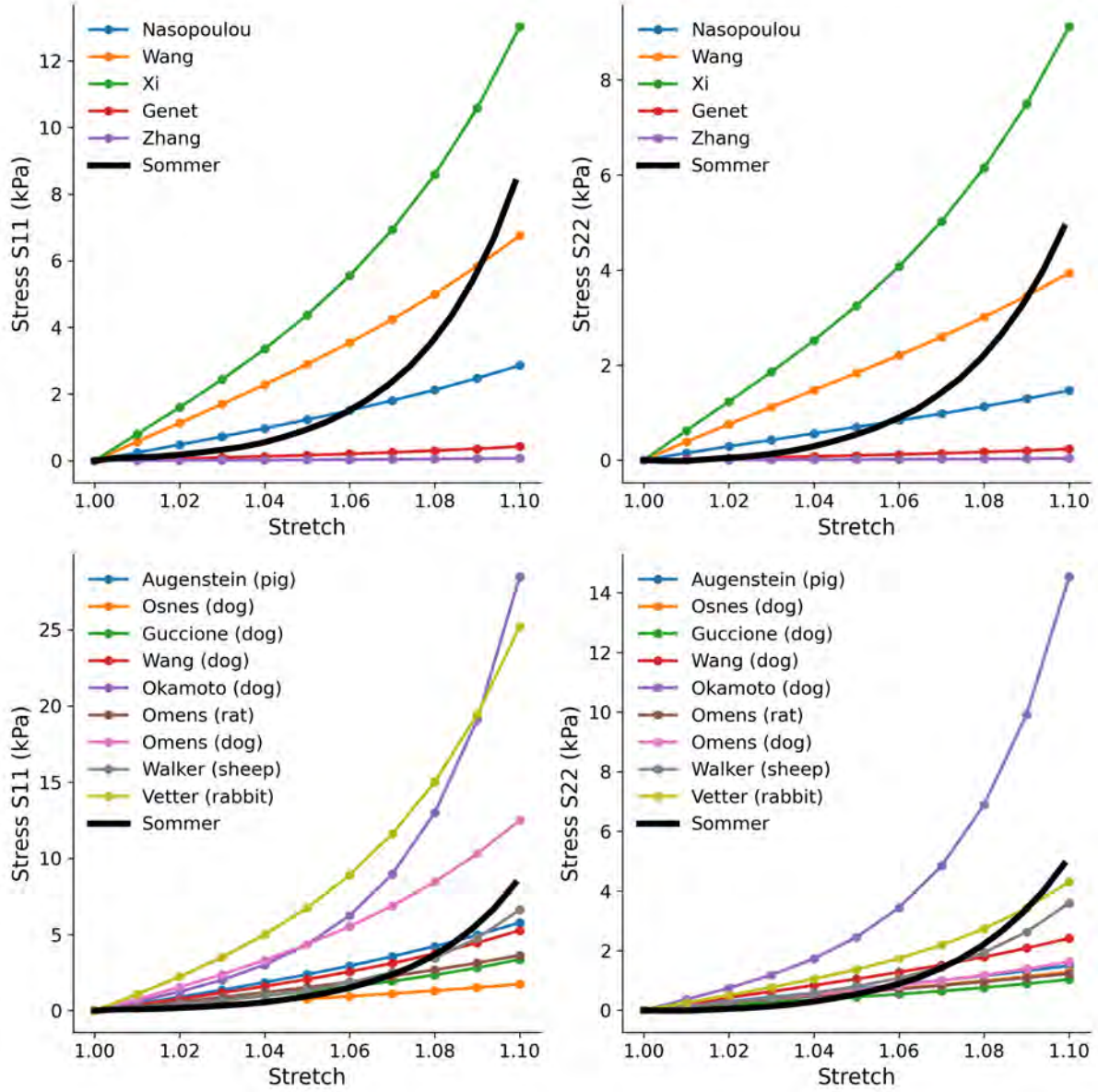
Figure 3.2 Stress-stretch curves of biaxial extension tests in the comparative study

In the fiber direction, the three parameter sets, based on animal data, that yield results closest to *Sommer et al.* [74] measurements are those reported by *Walker et al.* [103] ($RMSE = 0.62$), *Wang et al.* [8] ($RMSE = 1.19$), and *Augenstein et al.* [99] ($RMSE = 1.20$). Regarding parameter sets based on human data, these are those reported by *Wang et al.* [61] ($RMSE = 1.39$), *Nasopoulou et al.* [9] ($RMSE = 1.97$), and *Genet et al.* [7] ($RMSE = 3.14$).

In the cross-fiber direction, closest results based on animal and human data are respectively the ones reported by : *Walker et al.* [103] ($RMSE = 0.49$), *Vetter and McCulloch* [111]

($RMSE = 0.59$) and *Wang et al.* [8] ($RMSE = 0.91$) ; and *Wang et al.* [61] ($RMSE = 0.92$), *Nasopoulou et al.* [9] ($RMSE = 1.27$) and *Genet et al.* [94] ($RMSE = 1.87$).

All stress-strain curves are more linear than those reported by *Sommer et al.* [74] : curvature as measured in this study (second derivative average) is equal to $367.0kPa$ for *Sommer et al.* [74] measurements, compared to a maximum of $115.0kPa$ among human data-based models (obtained with *Xi et al.* [5] parameters, and respectively $281.3kPa$, $228.6kPa$, $170.1kPa$ with *Okamoto et al.* [128], *Walker et al.* [103] and *Vetter and McCulloch* [119] parameter sets.

Figure 3.3 shows the stress-stretch curves resulting from **triaxial simple shear** tests with five different parameter sets based on human data reported in the literature. For all parameter sets, stresses are higher in the FS and FN modes, than other modes. Stresses are equal by pairs, with FS and FN stresses being equal, SF and NF, and SN with NS. Convergence issues made it difficult to compare all parameter sets of the comparative study.
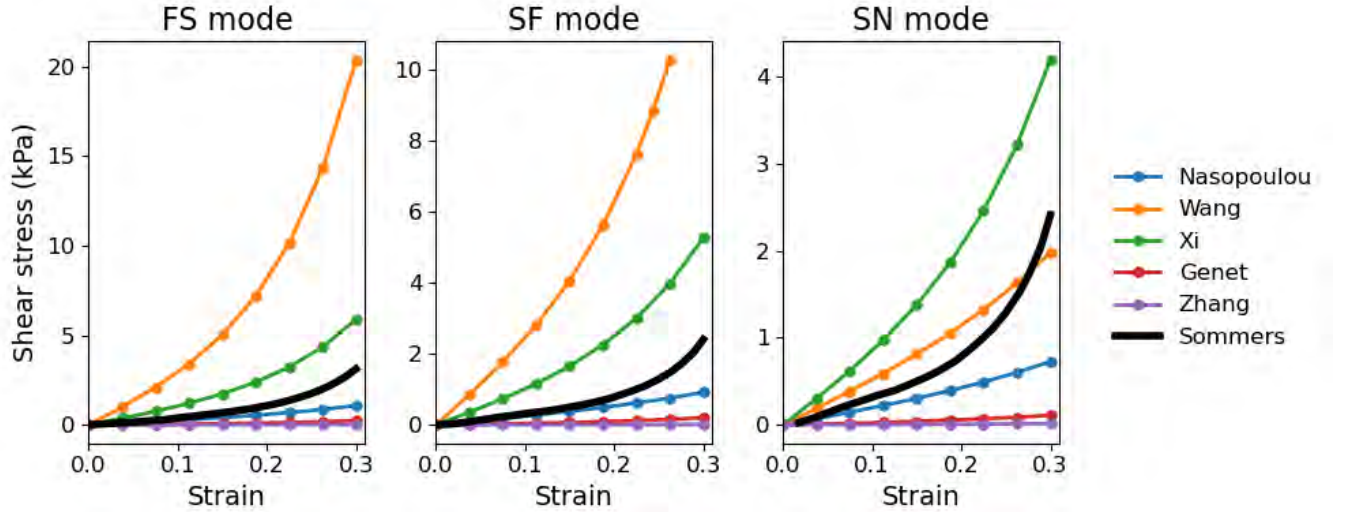
Figure 3.3 Stress-strain curves of triaxial simple shear tests in the comparative study

3.3.2 Passive inflation of an ideal left ventricle geometry

3.3.2.1 Sensitivity study

An increase in each parameter leads to a decrease in myocardium maximum displacement and cavity volume expansion. Detailed results for each parameter are shown in Table 3.3. The impact (percentage variation) on the displacement and cavity expansion of the ventricle, resulting from the variation of each parameter, is reported therein. Convergence issues were encountered with the two lowest values of b_{ft} and the smallest value of C, so the results were

not taken into account for these three values.

Table 3.3 Variations in maximum displacement and endocardial inner volume

		Variation (%)	
	Parameter	Maximum displacement	Cavity volume expansion
C	142.8	-129.5	-120.8
b_f	164.1	-77.6	-67.17
b_t	172.8	-114.4	-119.8
b_{ft}	93.5	-10.2	-9.3

Displacement distribution maps for the smallest values of b_f and b_t are shown on Figure 3.4. A decrease in b_f results in a widening of the geometry, whereas a decrease in b_t leads to its elongation during passive inflation.

(a) $b_{f_{min}}$ (b) $b_{t_{min}}$
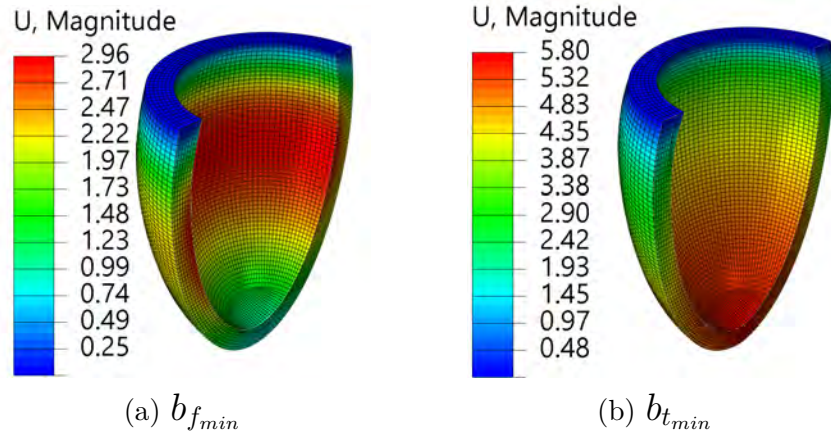
Figure 3.4 Displacement (U, mm) of an ideal left ventricle geometry with a $1kPa$ endocardial pressure

3.3.3   Patient-specific stiffness estimation

3.3.3.1   Sensitivity study

Figure 3.5 shows the impact of each parameter on the stiffness estimation with P03 patient-specific model.

Convergence issues encountered with the two smallest values of b_{ft} force us to exclude the results with these two values from the analysis.
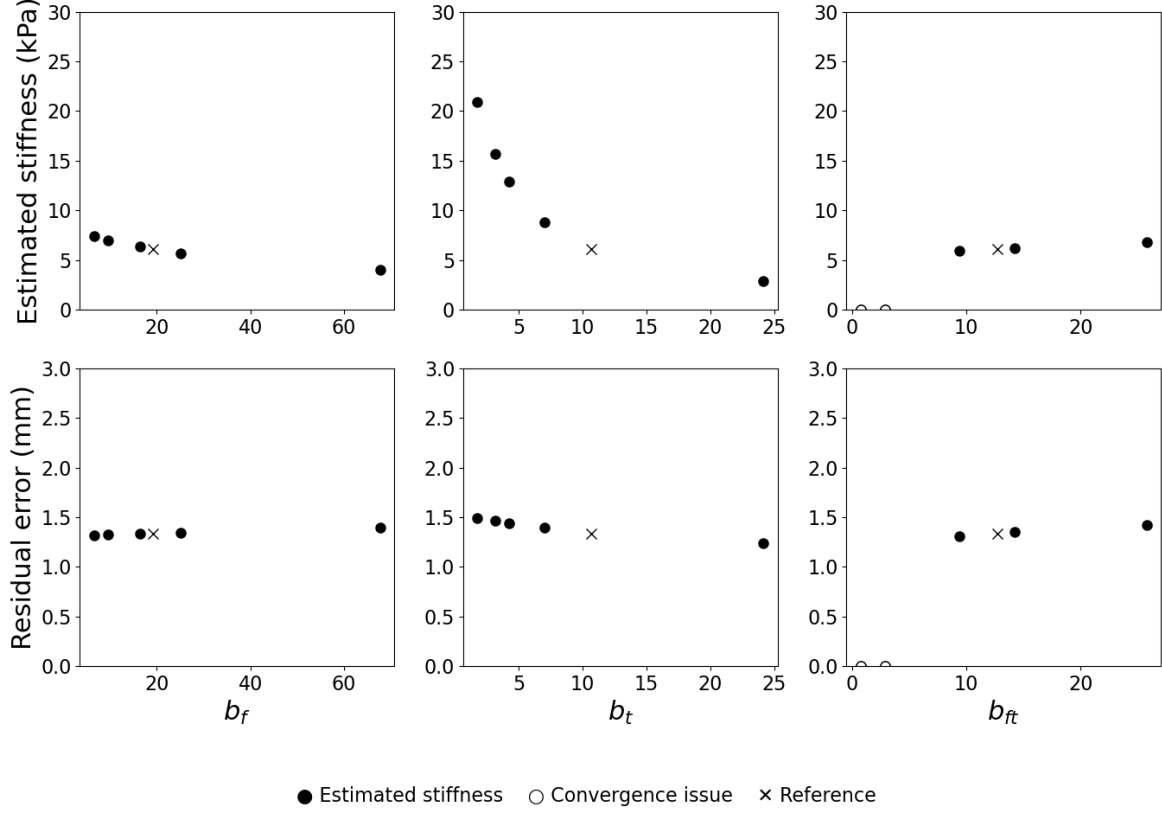
Figure 3.5 Patient-specific (P03) stiffness estimation in the sensitivity study

3.3.3.2 Comparative study

Figure 3.6 shows stiffness estimation and residual error using 5 different sets of parameters based on human data.

Due to convergence issues during optimization with the parameters from *Nasopoulou et al.* [9] parameters, stiffness estimation with these parameters are not available for subjects P01 and P06. Stiffness estimates using *Nasopoulou et al.* [9] parameters are thus excluded from the statistical analysis.

There are significant differences between parameter sets (Friedman ANOVA, $p < 0.1$), but no significant difference between residual error (Friedman ANOVA, $p > 0.1$). The average residual error is $1.8mm$. For the 6 volunteers, stiffness estimations showed a consistent ranking : $C_{Xi} < C_{Zhang} < C_{Genet} < C_{Wang}$. This order matches with the value of b_t in the set : $b_{t_{Xi}} > b_{t_{Zhang}} > b_{t_{Genet}} > b_{t_{Wang}}$.
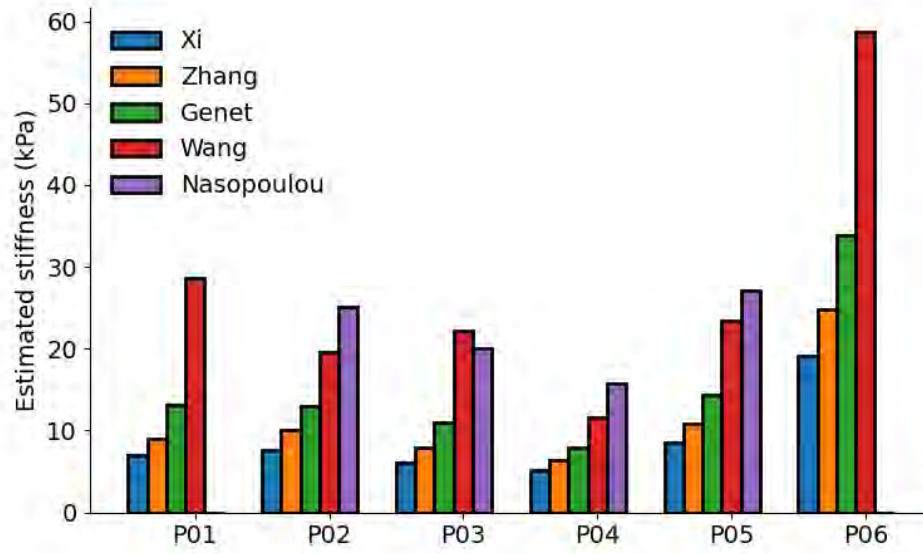
(a) Estimated stiffness
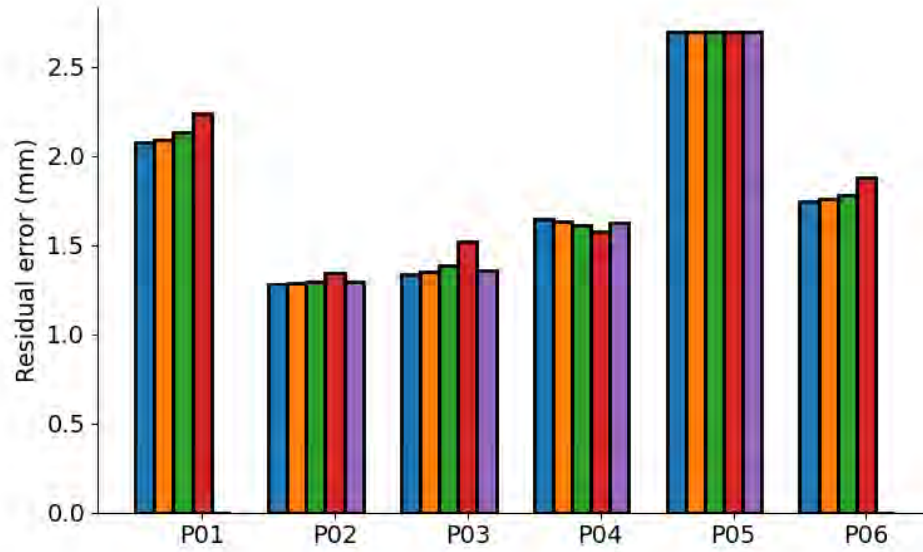
(b) Residual error

Figure 3.6 Estimated stiffness and residual error for the 6 volunteers (P01-P06) with different parameter sets (Xi : [5], Zhang : [6], Genet : [7], Wang : [8], Nasopoulou : [9])

3.4 Discussion

The aim of this study was to understand and evaluate the impact of the three anisotropic parameters (b_f, b_t, b_{ft}) on global stiffness estimation. The methodological approach involved analyzing the impact of each parameter of the set, and comparing existing parameter sets reported in the literature. The study was conducted from a local viewpoint (biaxial and shear tests) to a broader mechanical perspective (left ventricle ideal and patient-specific geometries). This should facilitate the informed choice of a parameter set, based on an understanding of its effects.

3.4.1 Biaxial extension and triaxial simple shear tests

3.4.1.1 Biaxial extension tests

For all parameter sets, stresses are higher in the fiber direction than cross-fiber direction, which is coherent with experimental data [74].

All stress-strain curves are more linear than the experimental measurement of *Sommer et al.* [71–74]. However, they remain consistent with simulation results reported by *Zhang et al.* [6]. The difference with experimental data could be explained by tissue damage and strain softening during tests, and the relief of residual stress due to dissection [4, 74]. Moreover, fibers may not be perfectly aligned and homogeneous in the experimental specimen.

Biaxial extension tests highlighted significant differences between stress-strain curves obtained with different parameter sets reported in the literature. This differences are consistent with the sensitivity study results :

- At fixed strain, stresses are directly proportional to global stiffness C. Stiffness values in *Genet et al.* [7] and *Zhang et al.* [6] are the smallest, and result in the lowest stress values among human data-based parameter sets.
- The parameters b_f and b_t contributes to increase of stress values and inflexion of stress-strain curve, respectively in fiber and cross-fiber direction. It can be observed in simulation results with *Okamoto et al.* [128], *Vetter and McCulloch* [119], and *Walker et al.* [103] parameter sets. The same tendency is also observed in simulation with *Xi and al.* [5] parameters set compared to other human data-based parameter sets.

3.4.1.2 Triaxial simple shear tests

The following pairwise equal stresses were observed : FS = FN, SF = NF, SN = NS. This result is consistent with the symmetry induced by the organization of the cardiomyocytes

and the strain-energy density function implemented, but does not match the pairs observed experimentally (FS = FN, SF = SN, NF = NS) [4,74]. Indeed, experimental measurements show orthotropic behavior, whereas transverse isotropic behavior was assumed. The choice of the strain-energy density function leads to neglect the laminar structure, taking only into account cardiomyocytes organization.

Unfortunately, the convergence issues associated with the model's large deformations prevent us from drawing definitive conclusions or precisely comparing the different parameter sets. Nevertheless, we could observe trends that are consistent with the energy density equation : shear stresses in the FS, FN, SF, and NF modes are influenced by the b_{ft} parameter, while those in the NS and SN modes are influenced by the b_t parameter.

Although results on shear stresses are limited, this should not affect the understanding of the impact of the parameters on stiffness estimation. Indeed, as discussed below, and confirmed by [8], the impact of shear on the ventricle mechanical behavior is low during diastole.

3.4.2 Passive inflation of an ideal left ventricle geometry

Mechanical simulations highlighted the impact of global stiffness C on local material behavior. This explains the major influence of this parameter on the displacement of the truncated ellipsoid. According to Rodriguez-Cantano et al. [101],C is by far the most influential parameter. In our study, however, the variation range of C is smaller, while the variation ranges of the other parameters are significantly larger. This difference may explain why C's influence does not appear to be as dominant relative to the other parameters as reported in their study.

Both b_f and b_t influence the passive expansion of the cavity. As their increase leads to an increase of stresses and local stiffness, respectively in fiber and cross-fiber direction, it is consistent to observe that it leads to a reduction in cavity volume expansion and myocardial displacement.

These two parameters impact the expansion of the cavity differently. A decrease in b_f, meaning a lower stiffness in the fiber direction, facilitates the widening of the cavity during diastole. In contrast, a decrease in b_t, meaning a lower stiffness in the cross-fiber direction, facilitates the lengthening of the cavity during diastole. This result is consistent with the fiber orientation implemented in the model. Indeed, due to their helical structure in the ventricle, most fibers have a larger circumferential component than longitudinal. Lowering b_f thus promotes widening. Conversely, as the component of cross-fiber direction is mainly longitudinal, lowering b_t promotes lengthening.

The b_t parameter is the most influential parameter of the 3 parameters of the set (b_f, b_t,

b_{ft}). Although the variation range remains of the same order of magnitude, the impact on expansion is clearly more significant.

3.4.3 Patient-specific stiffness estimation

As previously mentioned, b_f and b_t both contribute to constrain the left ventricle displacement. It is consistent to observe that their increase leads to a decrease in the estimated stiffness.

The minimal impact of b_{ft} on ideal left ventricle geometry displacement is coherent with its minimal impact on stiffness estimation, although only a few value are studied.

The parameter b_t once again stands out as the most influential parameter on stiffness estimation, which is consistent with previously mentioned results.

In the comparative study, the decision was made to focus on models based on human data, as there can be significant differences between species [75]. Although not shown in this study, stiffness estimation was also performed using *Walker et al.* [103] parameters, as the stress-strain curves obtained with these parameter best matches *Sommer et al.* [74] measurement. No significant difference of stiffness estimation and residual error was found when compared to the estimation performed using *Xi et al.*'s parameters [5] (Wilcoxon test, $p > 0.1$).

The estimated stiffness values are consistent with previous studies [8, 12, 20, 21]. However, for all parameter sets, the estimated stiffness remains higher in our study than reported in the cited work. This could be due to the fact that the pressure values used are only estimates, and when they exceed those reported in the cited studies, they may lead to higher stiffness. Additionally, differences in boundary conditions, whether more or less stringent, could also contribute to these observed differences.

Notably, for all subjects, the values of estimated stiffness with different parameter sets follow an ordering that is consistent with that of b_t. This finding supports the previously observed strong effect of b_t parameter.

There is no significant difference between residual error among parameter sets : no set stands out for better fit with segmentation data, and the C value compensates for the stiffness increase or loss of stiffness due to the other parameters.

3.4.4 Limits

There are some limitations to this study that must be taken into consideration.

First, due to the choice of the transversely-isotropic constitutive law, the orthotropic behavior

of the myocardium observed in experimental studies [4, 74] was not taken into account. The shear properties therefore remain approximate. However, this approach reduces the number of parameters in the constitutive law and helps mitigate issues related to non-uniqueness of the solution. Viscoelasticity was also neglected, but this is not expected to be an issue given the timescale considered [13].

Moreover, the material behavior is defined relative to a local orientation, defined by the myofiber orientation. However, patient-specific model include the general helical structure observed by *Streeter et al.* [15], but does not incorporate a patient-specific fiber architecture. Studies suggest that this should not compromise the results [101]. A more detailed analysis of this issue is provided in Chapter 4.

The convergence issues encountered during the simulation prevented the analysis of the full range of data initially planned. However, the results obtained, although incomplete compared to the initial method, still allow a meaningful understanding of the mechanical implications of the parameters and fulfill the objective of this study.

Finally, it is noteworthy that sensitivity studies performed to compare the influence of each parameter are highly dependent on the variation range of the parameters. Moreover, within each range studied, only few values are evaluated. Therefore, these sensitivity studies contribute to a better understanding of the impact of each parameter, although, caution is required when comparing the influence of one parameter to another. However, since the variation range is based on data from the literature, it should reflect the variability reported in published studies.

3.5 Conclusion

Left ventricle myocardial stiffness is a promising biomarker in early detection of heart failure. Finite element models are efficient tools to estimate this parameter. However, the estimation relies on the choice of a set of parameters (b_f, b_t, b_{ft}) which are highly variable across studies.

Table 3.4 summarizes the qualitative findings of the sensitivity study.

Table 3.4 Summary of parameters impact

	Mechanical tests	Passive inflation	Stiffness estimation
$b_f \searrow$	$S_{11} \searrow$	widening	estimated stiffness $\nearrow$
$b_t \searrow$	$S_{22} \searrow$	lengthening	estimated stiffness $\nearrow$
	$SN, NS \searrow$	*strong impact*	*strong impact*
$b_{ft} \searrow$	$SF, FS, FN, NF \searrow$	*minor impact*	*minor impact*

In the comparative study, we observed significant differences in stress-strain curves resulting from different parameters sets reported in the literature. Stiffness estimation performed with different parameter sets reported in the literature were also significantly different. However no model stands out as being more suited in terms of residual error. The parameter b_t stands out having a crucial impact on the observed differences.

Stiffness estimation performed with *Xi et al.* [5] parameters is closest to the stiffness values found in the literature [5, 20, 61]. This parameter set also leads to consistent mechanical simulation results compared to *Sommer et al.*'s measurements. Therefore, the set of parameters reported by *Xi et al.* [5] is selected for the subsequent part of the study.

To our knowledge, this study is the first to compare parameter sets reported in the literature, and it should contribute to a better understanding and assessment of the impact of the parameters variability. This step seems crucial to the longer-term objective of determining standard and pathological values of myocardial passive stiffness, and brings us closer to the ultimate goal of early detection of cardiotoxicity and heart failure.

However, as previously discussed, the selection of local mechanical parameters dictates material properties relative to the local orientation. It is thus intrinsically linked to fiber orientation. Accordingly, it is essential to assess the degree of precision needed in defining fiber orientation. This constitutes the objective of the next chapter.

CHAPTER 4   ASSESSING THE IMPACT OF FIBER ORIENTATION IN LEFT VENTRICLE MYOCARDIAL STIFFNESS ESTIMATION

4.1   Introduction

This study builds upon previous work (Chapter 3). In the context of stiffness estimation with patient-specific model, this prior study demonstrated the significant impact of anisotropy parameters (b_f, b_t, b_{ft}). Since these parameters are defined relative to fiber architecture in the model, investigating the effect of the architecture itself stood out as an important analysis.

Even if called "patient-specific", most of finite element models used for stiffness estimation do not include a patient-specific cardiac fiber architecture. This is mainly due to the challenges associated with in vivo DTI acquisitions [20].

Instead, the helical architecture described by *Streeter et al.* [15] is commonly adopted. This fiber orientation is characterized by an helix angle varying linearly from about 60° at the endocardium surface, to about −60° at the epicardium surface, throughout the entire circumference and height of the left ventricle.

Nonetheless, as mentioned in Chapter 2, significant deviations from this general fiber architecture have been reported in both healthy and pathological subjects [29, 67]. Moreover, fiber orientation has been reported to have a non-negligible impact on left ventricle mechanics [2, 90, 97, 98, 101, 122] (see Chapter 2). However, fewer studies have focused on this impact on stiffness estimation. Yet, this is crucial to assess the extent to which fiber orientation in the model need to be patient-specific, and determine the required level of precision.

Indeed, a complete personalization of fiber architecture based on in-vivo DTI acquisitions increases the complexity of the process, and is much more time-consuming during both acquisition and post-processing. It is therefore necessary to develop a method of fiber implementation that balances ease of implementation with sufficient precision. Achieving this requires the understanding and evaluation of the impact of fiber orientation on stiffness estimation.

The aim of this Chapter is to understand and assess the impact of fiber architecture on the stiffness estimation. This can be divided into two specific sub-objectives :

1. Evaluate how fiber orientation impacts the left ventricle passive inflation
2. Compare stiffness estimation using different fiber orientations

4.2 Methods

Three MRI datasets of healthy subjects from F. Mahalatchimy's master research [21] are selected (P02, P03, P05), and patient-specific models are built. The impact of fiber orientation is analyzed using these three finite element models.

These finite element models serve two main purposes, each addressing a specific sub-objective:

1. First, a standard pressure is applied at the endocardial surface of the model, and mechanical behavior during inflation is analyzed.
2. Then, using a patient-specific estimated pressure, stiffness is estimated by inverse optimization.

The analysis is divided into five steps, each aiming at evaluating the impact of a precise parameter of the fiber architecture :

- Global change in maximal helix angle : value of helix angle at endocardium and epicardium are modified
- Transmural change in helix angle : transmural distribution of helix angle from endocardium to epicardium is no longer linear but asymmetrical
- Change in maximal helix angle by sector : fiber orientation in one of the 17 sectors defined by the American Heart Association (AHA) [130] is affected, while fiber orientation in the rest of the ventricle remains unchanged
- Change in transverse angle : a non-zero value of transverse angle is assigned in the ventricle
- Reconstruction of fiber architecture from a single DTI slice : fiber orientation is reconstructed in the whole ventricle from a single mid-ventricular slice of in-vivo DTI acquisition of *Moulin et al.* [29],

The following sections provide a comprehensive description of the finite element models construction. As mentioned in Section 2.6, the framework is based on F. Mahalatchimy's master research [21].

4.2.1 Construction of patient-specific meshes

The construction of patient-specific meshes relies on a template mesh and segmentation data. The main idea behind the method is to move the mesh points to match those of the segmentation, so that the final mesh reproduces the patient-specific left ventricle geometry. The whole method is implemented using MATLAB (vR2024a)

The segmentation data were rigorously validated in F. Mahalatchimy's master research [21]

and are kept unchanged. The points obtained from the segmentation are imported directly in MATLAB. It consists of epicardial and endocardial contours in short-axis views, as well as epicardial contours in the 3-chamber and 4-chamber views. Figure 4.1 shows epicardium and endocardium points obtained from segmentation of the P03 short-axis views.
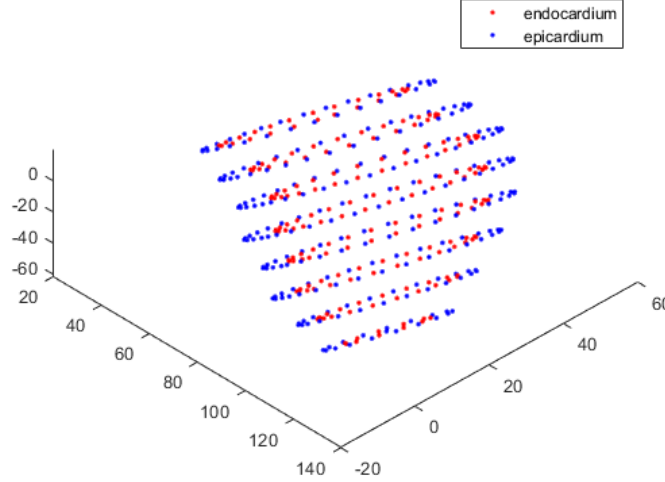

Figure 4.1 Points obtained from the segmentation in short-axis view (P03)

The template mesh is an ideal geometry of the left ventricle, which is a truncated ellipsoid, built in Abaqus, as described in Chapter 3. The mesh resolution is chosen based on a convergence study, as described below. The nodes of the template mesh are imported in MATLAB.

4.2.1.1 Alignment of geometries

The first step in the construction of patient-specific meshes is the alignment of the template mesh nodes and segmentation points.

First, the direction of the long axis is determined in the mesh and in the contours of the segmented epicardium. A rigid rotation is applied to segmented points in order to align these two axes. Then, an Iterative Closest Point registration algorithm is applied to compute the rigid rotation and translation required to align the segmented epicardium basal plane with basal plane in the mesh. Next, this same transformation is applied to all points of the segmentation (epicardial and endocardial contours in short-axis views, epicardial contours in the 3-chamber and 4-chamber views). Figure 4.2 illustrates this alignment.
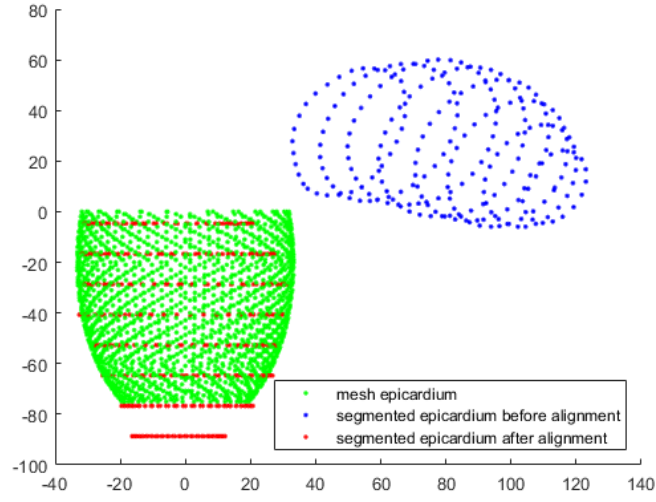
Figure 4.2 Epicardial contours before and after alignment, relative to template mesh nodes

Thereafter, short-axis slices obtained from segmentation are aligned with 3-chamber and 4-chamber points, to correct motion-related artifacts. To achieve this, epicardial contour in 3-chamber and 4-chamber views are divided by slices, as illustrated in Figure 4.3. Each epicardial short-axis slice is centered within them, and the computed translation is then applied to the endocardial slice.
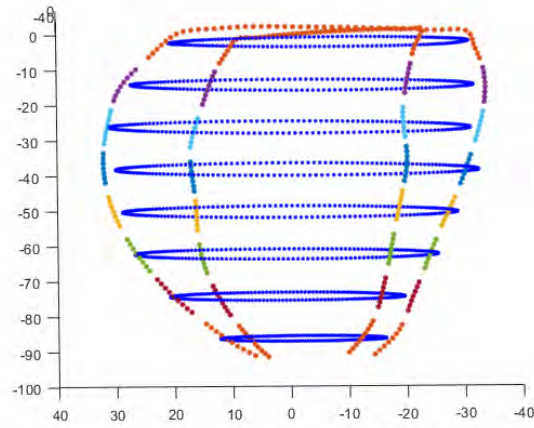

Figure 4.3 Epicardial contours divided by slices

4.2.1.2   Morphing

Each point of short-axis epicardial and endocardial contour is associated to its closest point in the mesh, measured with Euclidian distance. A 3D Thin Plate Spline Algorithm is used to estimate the displacement field needed for control points to match segmentation points, and deform the mesh nodes accordingly. This process is illustrated in Figure 4.4. This allows to determine the coordinates of the patient-specific mesh nodes.
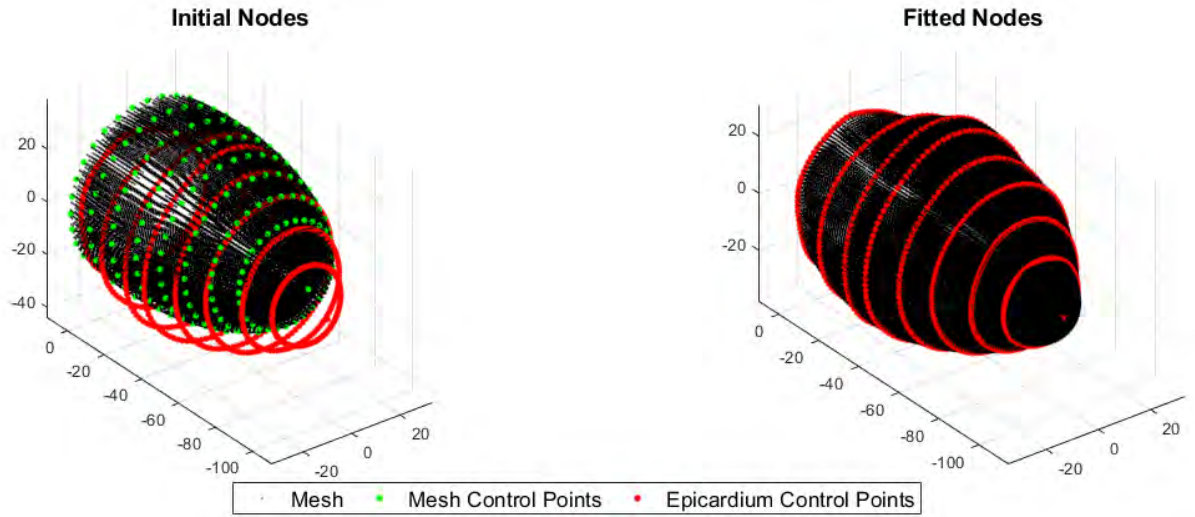

Figure 4.4 Epicardial contours divided by slices

This method is applied to built patient-specific mesh for subjects P02, P03, and P05 of F. Mahalatchimy's master research [21]. Segmented data acquired at rest and during isometric contraction are used. The final meshes are illustrated in Figure 4.5
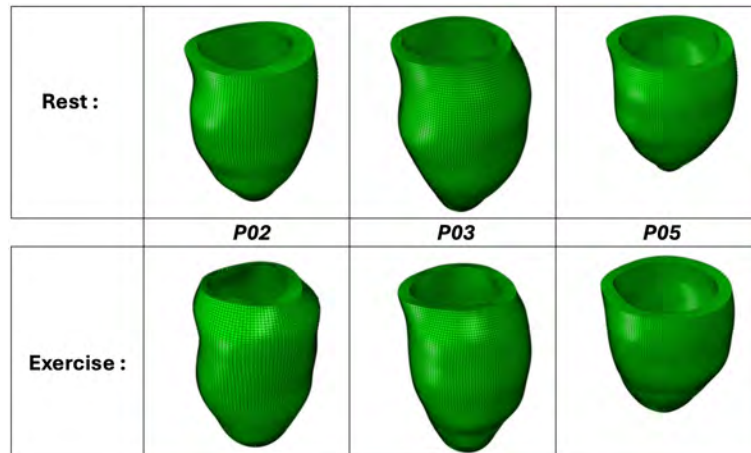

Figure 4.5 Final meshes

4.2.1.3   Mesh convergence

To determine the mesh resolution, a mesh convergence study is performed. The quantities of interest to assess convergence are stress and strain in the fiber direction within the complete ventricle, and excluding 10% of the geometry near the base, which corresponds to the boundary condition region. Figure 4.6 shows this analysis. Since the transmural distribution of stress will be analyzed in this study, a qualitative verification of this quantity is also performed. The "layers" mentioned in this figure correspond to the number of transmural layers in the ventricle wall mesh. Finally, the 7-layers mesh, composed of 87346 elements is selected. It ensures that the maximal stress deviation with finer mesh is equal to 5.6% in the complete ventricle and 1.5% when excluding the basal part. The strain deviation is equal to 1.6% in the complete ventricle.
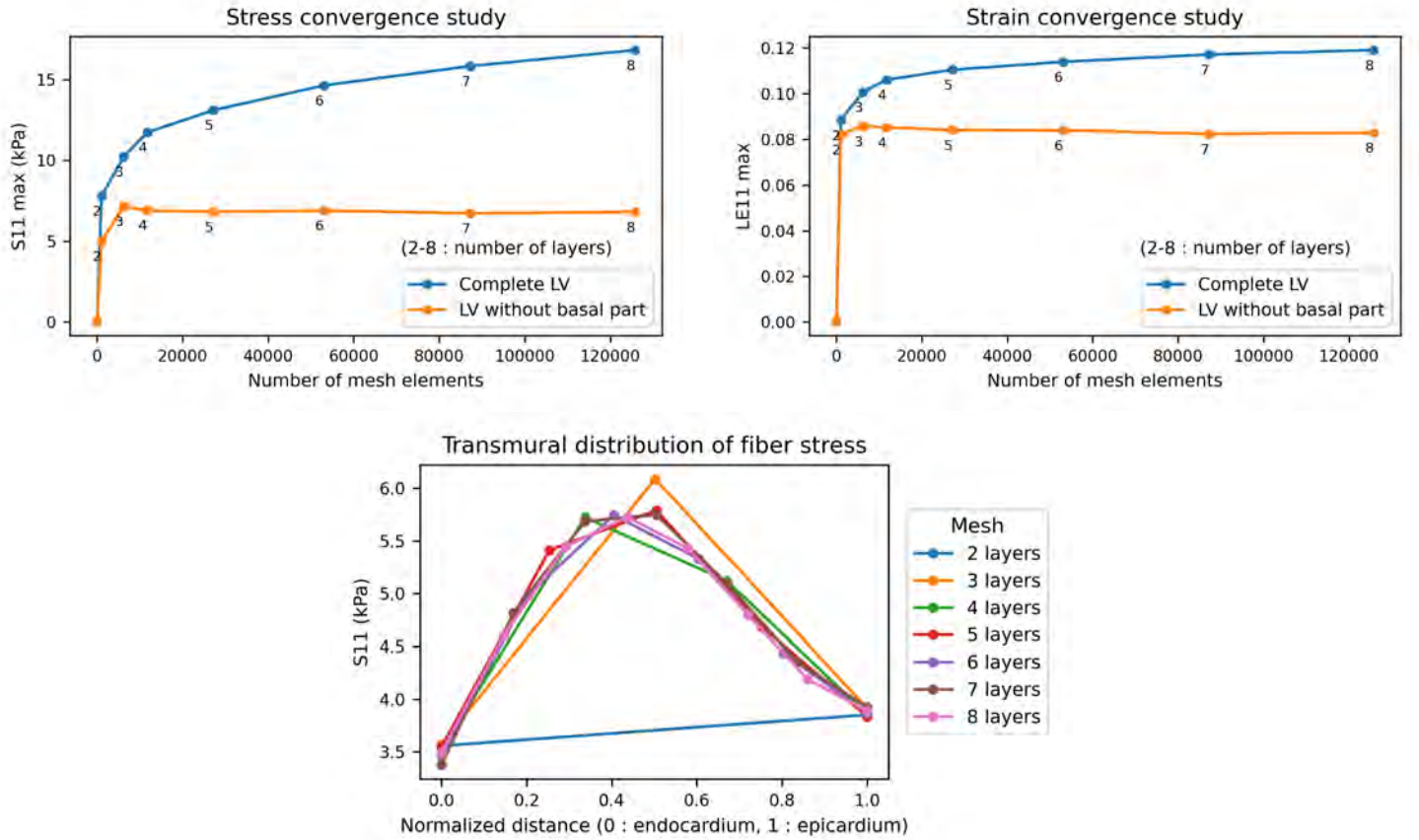

Figure 4.6 Mesh convergence results

4.2.2 Fiber orientation implementation

Fiber orientation is implemented in the finite element model by assigning a local coordinate system to each element of the mesh. For each of the 5 studies described in the introduction of this Section, different fiber architectures are implemented. However, the method remains essentially the same. The fiber orientation is computed for each element using MATLAB (vR2024a) and then written to the Abaqus *.inp* file.

The first paragraph outlines the shared aspects of this computation, followed by detailed information on the different studies in the subsequent paragraphs.

4.2.2.1 Shared features

1st step - Local coordinate system :

First, a local orientation, relative to the ventricle geometry, independent of fiber orientation, has to be computed for each element of the mesh. From this local orientation, the fiber orientation can be defined [3, 32].

In each element, the local orientation is defined by 3 axis : $\vec{e_n}$ is the normal vector of the wall local surface, $\vec{e_z}$ the longitudinal vector, and $\vec{e_c}$ the circumferential vector. These vectors are illustrated in Figure 4.7.

For each element, the coordinates of the four nodes defining the internal wall surface (closest to the endocardium) and the external wall surface (closest to the epicardium) are used to compute their respective normal vectors. The vector normal to the surface is computed using singular value decomposition. They are oriented from endocardium to epicardium. The normal vector $\vec{e_n}$ is obtained by averaging internal and external normal vectors.

The longitudinal vector $\vec{e_z}$ is perpendicular to the basal plane. The normal direction is obtained using singular value decomposition.

Finally, the circumferential vector is the cross product of $\vec{e_n}$ and $\vec{e_z}$.
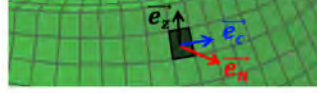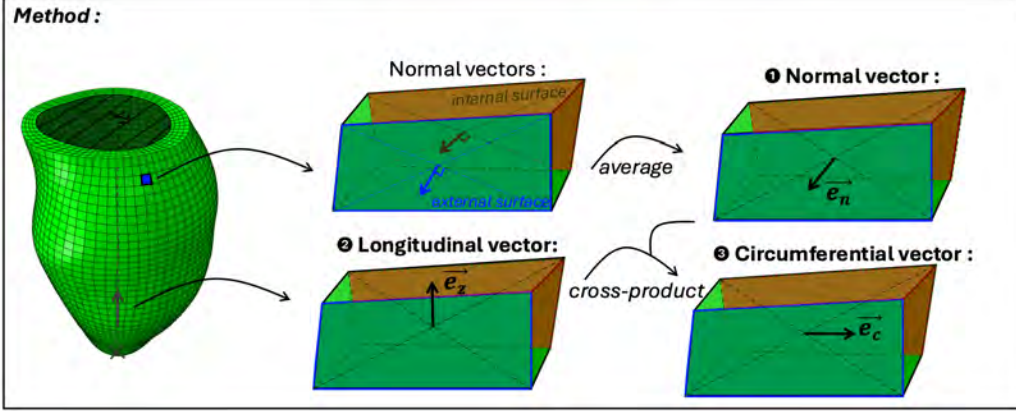
Figure 4.7 Implementation of local orientation ($\vec{e_n}$: radial direction, $\vec{e_c}$: circumferential direction, $\vec{e_z}$: longitudinal direction)

2nd step - Fiber orientation :

As presented in Chapter 2, fiber orientation is usually defined relative to the local coordinate system, by the helix and transverse angle. The fiber direction can defined as : $\overrightarrow{fiber} = \cos(\alpha)\sin(\beta)\vec{e_n} + \cos(\alpha)\cos(\beta)\vec{e_c} + \sin(\alpha)\vec{e_z}$. The cross-fiber direction can be defined as : $\overrightarrow{cross - fiber} = \cos(\beta)\vec{e_n} - \sin(\beta)\vec{e_c}$. This vectors are illustrated in Figure 4.8.

The coordinates of fiber and cross-fiber directions can thus be computed for each element of the mesh, and written in the simulation file.

Figure 4.8 Implementation of fiber orientation

4.2.2.2 Reference fiber orientation

Given that the objective of this study is to compare different fiber architectures to evaluate the model's sensitivity to them, a refere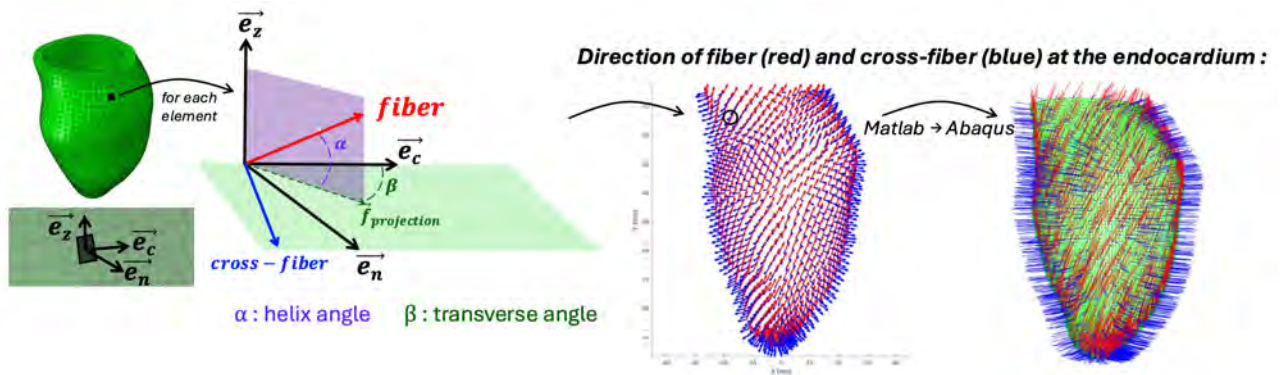nce fiber configuration is chosen for comparison. This reference architecture is the commonly used orientation described by *Streeter et al.* [15]. The helix angle is equal to $60°$ at the endocardium, and $-60°$ at the epicardium. The transmural variation is linear, symmetric, and centered around mid-ventricle. This distribution is homogeneous from base to apex. The transverse angle is uniformly zero across the entire ventricle. This fiber orientation is illustrated in Figure 4.9.
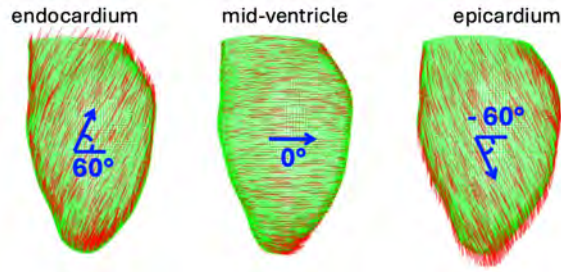
Figure 4.9 Reference fiber orientation

4.2.2.3 Global change in maximal helix angle

The first parameter that is modified relative to the reference orientation is the helix angle value at endocardium and epicardium. The transmural variation remains linear, symmetric, and centered around mid-ventricle. However, helix angle at the endocardium varies from $10°$ to $90°$, with increments of $10°$ across models. These values are chosen based on the extrema of helix angle values reported in histological and DTI studies [15, 16]. The helix angle at the epicardium remains the opposite of endocardium value, and transverse angle remains zero. This fiber orientation is illustrated in Figure 4.10.

Figure 4.10 Examples of fiber orientations for different values of the maximal helix angle
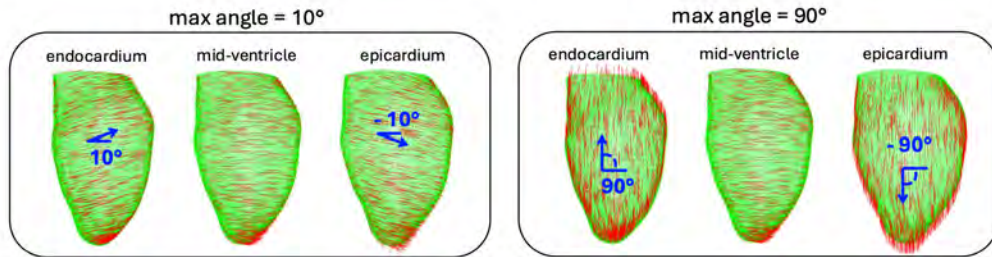
4.2.2.4 Transmural change in helix angle

The second parameter that is modified relative to the reference orientation is the transmural variation of helix angle. Helix angle values at the endocardium and epicardium remains respectively 60° and −60°, but the variation between the two is offset. The zero value of helix angle is shifted from the mid-ventricle, varying between 0 and 100% of the transmural distance between endocardium and epicardium. This helix angle distribution is illustrated in Figure 4.11. The transverse angle remains zero.
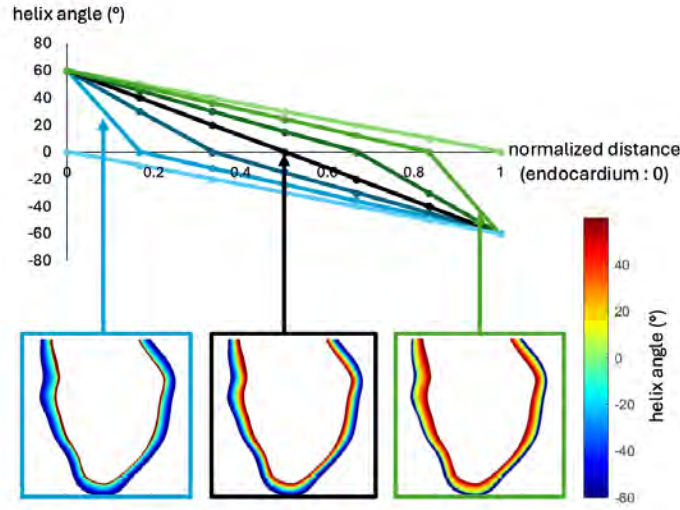
Figure 4.11 Examples of transmural distribution of helix angle

4.2.2.5 Change in maximal helix angle by sector

In order to assess the impact of fiber orientation in each ventricle region independently, fiber orientation in one of the 17 AHA segments [130] is affected, while in the rest of the ventricle it remains identical to the reference configuration. The sectors are modified sequentially, with a zero helix angle assigned throughout each affected sector.

For each subjects, sectors are segmented on MRI images. The transformation used for mesh construction and applied to the segmentation points during the geometry alignment process (see the first steps of the previous section) is also applied to the sectors contour points. Sectors are thus aligned with the final mesh geometry. Then, each element of the mesh is assigned to one of the 17 segments. To achieve this, the longitudinal distance (y) and azimuthal angle ($arctan(\frac{z}{x}) \pm \pi$) of each elements are computed [3, 32]. These two coordinates, compared to the same coordinates of the segment contours, allow assigning each element to one of the 17 AHA segments. The 17 sectors are illustrated in Figure 4.12.
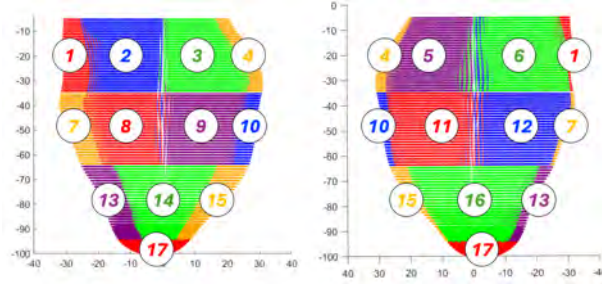
Figure 4.12 Example of left ventricle division by segments

4.2.2.6 Change in transverse angle

In existing models, the transverse angle is often considered to be zero [5, 7, 32], and such is the case in the reference orientation of this study. DTI studies confirm that the transverse angle is zero on average and correlates poorly with location in the myocardium [16, 27]. To our knowledge, there is little geometric description of transverse angle variations, unlike the helix angle. The chosen distribution is based on that described by *Bovendeerd et al.* [2] and has been adopted by other researchers [23, 92].

The transverse angle varies both transmurally and from base to apex. It varies transmurally from 0° at the endocardium, to an extremum in mid-ventricle, to 0° at the epicardium. This extremum varies longitudinally : it is maximum at the base, 0° in the mid-ventricle, and minimum at the apex. More precisely, apex mid-ventricle value is the opposite of basal mid-ventricle value. This distribution is shown in Figure 4.13. Based on extrema reported in the literature [16], the maximum value of transverse angle varies from 0° to 50°, with increment of 10° across models.

The helix angle distribution remains identical to the reference orientation.

Figure 4.13 Examples of transverse angle distribution

4.2.2.7 Reconstruction of fiber architecture from a single DTI slice

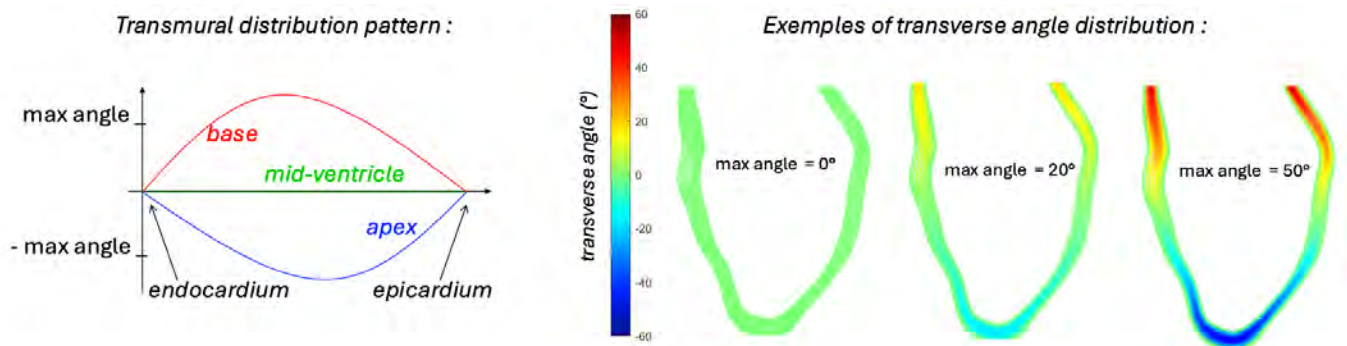The four previous studies provide insights into the physical implications of various fiber orientation parameters and their impact on stiffness estimation. The objective of this last study is to compare different, more physiologically "realistic" fiber configurations to evaluate the significance of variations among healthy configurations.

Mid-ventricular DTI slices acquired at diastasis from six healthy volunteers are adapted to the previously mentioned patient-specific finite element models. These DTI data are taken from *Moulin et al.* [29].

For each of the three finite element models, these six fiber architectures are implemented and compared. The implementation methods presented below is identical for all three models and six DTI slices.

The DTI slices include the complete fiber and sheetlets orientation, describe by the three eigenvectors in each voxel. This orientation can also be described by helix, transverse, and E2A angles. In this study, the sheetlet angle is neglected due to the assumption of transverse isotropy. The transverse angle is also neglected, given its minimal influence, as demonstrated in the following sections. The helix angle is the only angle considered. The method works as follows : the helix angle distribution map on the DTI slice is wrapped onto a mid-ventricle slice of the mesh, and data are then extended from base to apex. The method involves the following steps, illustrated in Appendix B :

1. The mesh nodes coordinates of a mi-ventricle slice of the finite element model are extracted. Using the same method as described for the division in AHA segments, nodes in the septal parts are identified.
2. Using rigid translation and rotation, the DTI and mesh slices are first centered, then rotated to align the septa.
3. Control points are selected on the endocardial contour of the mesh. Each point is associated with its closest point on the endocardial contour of the DTI slice, measured with Euclidean distance. The same process is applied to the epicardial contour. Using these control points, a 2D Thin Plate Algorithm is used to deform the DTI slice geometry to fit the mesh slice geometry. Each element of the mesh is associated to the closest helix angle value of the deformed DTI slice, using the Euclidean distance.
4. From the mid-ventricle mesh slice associated with helix angle values, the helix angle distribution map is extended to the entire ventricle. Given that only one slice was available and that the helix angle distribution has been reported to be relatively uniform from base to apex [17], the mid-ventricular distribution was reproduced by duplicating it

along the long axis of the ventricle. To achieve this, the azimuthal angle and transmural distances are computed for each element of the mesh, and these coordinates are used to assign the corresponding helix angle value from the mid-ventricular slice. Final reconstruction are shown in Appendix C.

4.2.3 Mechanical framework

The precedent sections described the mesh construction and assignment of local orientation for each element of the mesh. To complete the finite element model, the material constitutive law, as well as loading and boundaries conditions need to be implemented.

4.2.3.1 Material constitutive law

The myocardium is assumed to be homogeneous, hyper-elastic, incompressible, and transversely-isotropic. The material constitutive law is the Fung-type anisotropic law described in more details in Chapter 3 :

$$\psi = \frac{1}{2} C \left(e^Q - 1 \right)$$

with

$$Q = b_f E_{ff}^2 + b_t (E_{ss}^2 + E_{nn}^2 + 2 E_{sn}^2) + 2 b_{ft} (E_{fs}^2 + E_{fn}^2)$$

According to Chapter 3, parameters b_f, b_t, and b_{ft} are selected based on the values provided by *Xi et al.* [5] : $b_f = 19.13$, $b_t = 10.67$, $b_{ft} = 12.76$.

As previously mentioned, the finite element models serve two main purposes : in one case, the focus is on studying the passive inflation of the ventricle ; in the other on estimating the patient-specific myocardial stiffness. Thus, in the first case, global stiffness C is set to the standard value of $2kPa$ [5]. In the second case, C is estimated by inverse optimization.

4.2.3.2 Loading and boundaries conditions

All nodes at the base are fixed, and pressure is applied on the endocardial surface. In the first case (study of the passive inflation of the ventricle), a standard pressure of $1kPa$ [5] is applied. In the second case, (stiffness estimation), a patient-specific pressure is estimated with CircAdapt model. These patient-specific pressure values are used directly, without modification, from F. Mahalatchimy's work [21], and are summarized in Table 4.1.

Table 4.1 Patient-specific pressure for the three subjects studied

Subject	Rest	Isometric contraction
P02	1.30 kPa	2.10 kPa
P03	1.35 kPa	1.11 kPa
P05	1.54 kPa	3.15 kPa

4.2.4 Results analysis

In the passive inflation study, the maximum stress and strain in the fiber direction are extracted at the end of the simulation. Maxima are computed across the entire ventricle, excluding the basal 10%. The average displacement, as well as maximum longitudinal displacement and maximum displacement in the basal plane, are also extracted. The results are compared to a reference value by computing the percentage deviation. Transmural values of stress at the base, mid-ventricle, and apex are also extracted, and compare qualitatively. Stress and strain distributions in the myocardium are also analyzed. All results are extracted from the simulation *.odb* file using Python (v3.11.9).

In the stiffness estimation study, stiffness is estimated by inverse optimization using the optimization algorithm developed by F. Mahalatchimy's [21]. In the first three fiber orientation studies, the obtained stiffnesses are compared to the reference value by computing the percentage deviation. In the last study (reconstruction from a DTI slice), stiffness estimations are compared using a Friedman ANOVA [129], with a significance level of $p = 0.1$, followed by post hoc pairwise Wilcoxon signed-rank tests corrected for multiple comparisons using the Bonferroni method. Both estimated stiffness and residual error (objective function at the end of the optimization) are compared. Computation are performed using Python (v3.11.9).

4.3 Results

This section provides the results of the five different studies previously described.

4.3.1 Global change in maximal helix angle

4.3.1.1 Passive inflation

Figure 4.14a reports the maximum stress value in the myocardium according to the maximal helix angle. Figure 4.14b shows the stress distribution in P03 myocardium for different maximal helix angle. Figure 4.15 illustrates the impact of the angle variation on transmural

value of stress in P03 model.

As illustrated in Figure 4.14a, lower helix angles ($\leq 30°$) lead to an increase in maximum stress compared to the reference orientation. Between fiber orientations with $60°$ and $10°$ maximum helix angle, the maximum stress deviates by an average of 24.4% across the three subjects studied. For lower helix angles, maximum stress values are located near the endocardium surface. More generally, as illustrated in Figure 4.15, stresses values are globally higher at the endocardial surface when helix angle decreases.

Higher helix angle values also result in increased maximum stress, but the maximal stress is located near the middle of the wall thickness. The deviation in maximum stress between fiber orientations of $60°$ and $90°$ is 6.5% on average for the three subjects. Overall, as illustrated in Figure 4.15, stress values increase near the middle of the wall thickness with decreasing helix angle, especially in the mid-ventricle region.

Moreover, as shown in Figure 4.14b, increasing the helix angle from $10°$ to $90°$ leads to greater stress homogenization within the myocardium.

Figure 4.15 also shows that stresses in the apical region are lower and less influenced by the helix angle. However, the same tendency is observed regarding the impact of the helix angle when compared to the mid-ventricle. This same tendency is also observed in the basal region, but with a fewer impact due to boundary conditions. The same study has been performed on other cross-sectional planes (see Appendix E), and although stress values and their transmural variations are influenced by the local geometry, the same tendencies are observed. Observations are identical with P02 and P05 geometries (see Appendix E).

The results of strain analysis are similar to stress results (see Appendix E). Maximum strain value in the myocardium is minimal for an helix angle around $60° - 70°$, with an increase of strain at the endocardium surface for lower angles, and near the middle of the wall thickness for higher angle. Higher helix angles ($\geq 60°$) leads to greater strain homogenization within the myocardium.

Figure 4.16 shows the impact of maximal helix angle on displacement during passive inflation. For all three subjects (P02, P03, P05), displacement in the basal plane is higher than vertical displacement. The displacement in the basal plane tends to increase as the maximal helix angle increases (average increase of 8.6% across the three subjects between $10°$ and $90°$), while vertical displacement exhibits a sharper decrease (average decrease of 30.7% across the three subjects between $10°$ and $90°$). Globally, the average displacement in the myocardium decreases as the maximal helix angle increases (average decrease of 13.1% across the three subjects between $10°$ and $90°$).
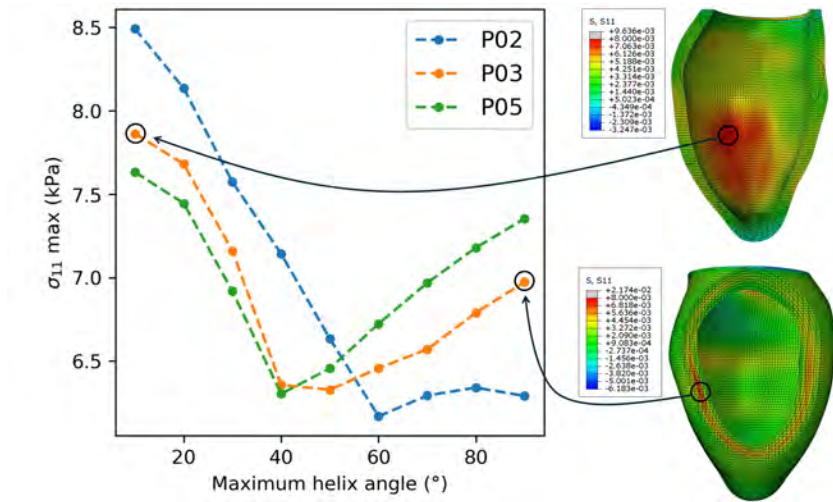
(a) Maximum stress in the myocardium
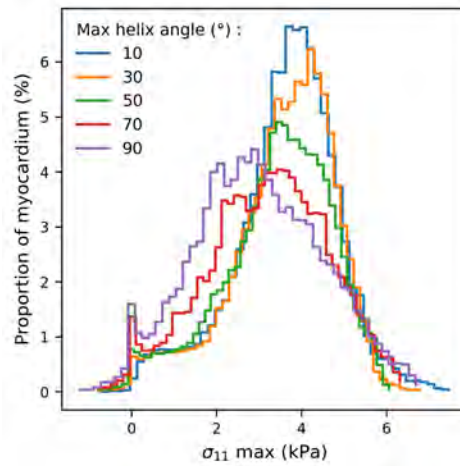
(b) Distribution of stress in the myocardium

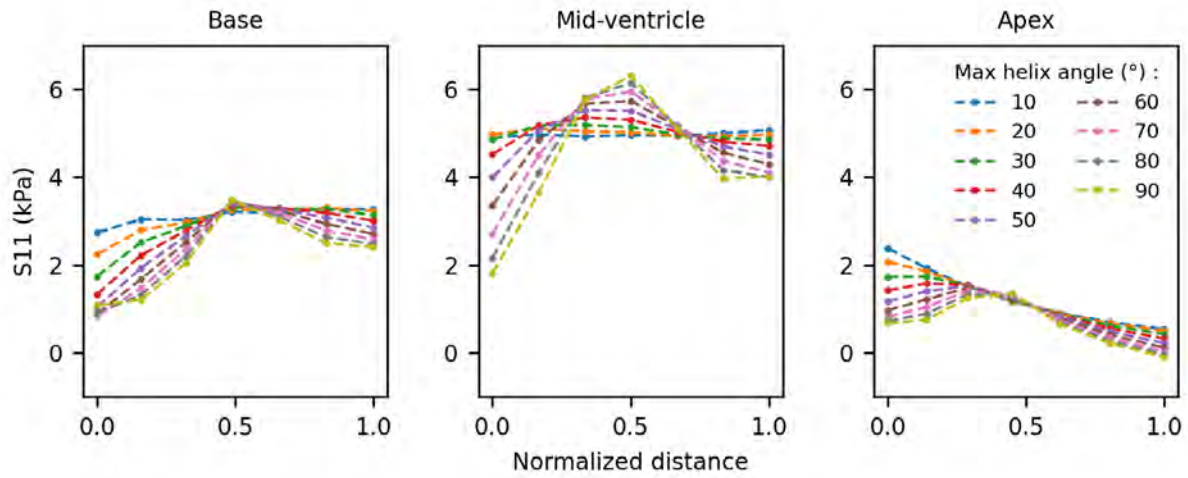Figure 4.14 Impact of maximum helix angle on stress in the myocardium

Figure 4.15 Impact of maximum helix angle on transmural stress values (P03)
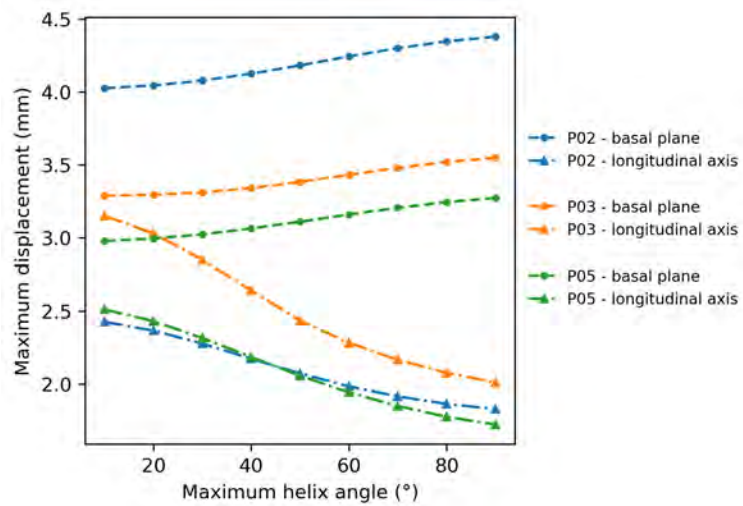
Figure 4.16 Impact of maximum helix angle on myocardium displacement

4.3.1.2 Stiffness estimation

Figure 4.17 shows the impact of maximal helix angle on estimated stiffness and residual error. Compare to the reference orientation (60°), the maximum deviation observed is 8.7%, 22.4%, and 5.9% respectively for P02, P03, P05, associated to a respective deviation in residual error equal to 2.1%, 5.8% and 0.60%.

(a) Estimated stiffness   (b) Residual error
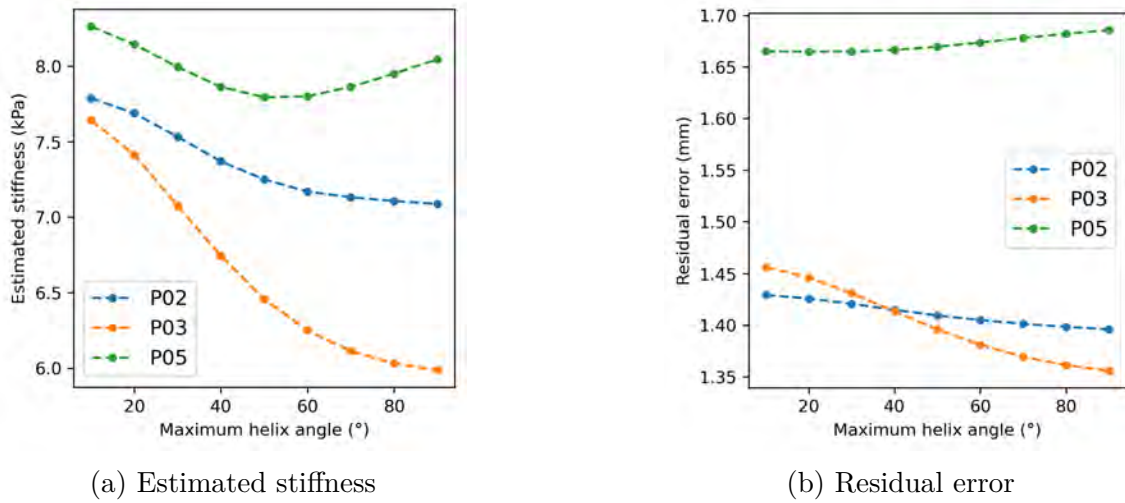
Figure 4.17 Estimated stiffness and residual error with different maximum helix angle

As illustrated in Figure 4.18, at isometric contraction, the impact of fiber orientation on stiffness estimation follows the same trend as at rest for each subject.

The influence of fiber orientation is slightly greater during isometric contraction compared to rest, with respective variations of 15.7%, 37.0%, and 6.1% for subjects P02, P03, and P05 during isometric contraction.
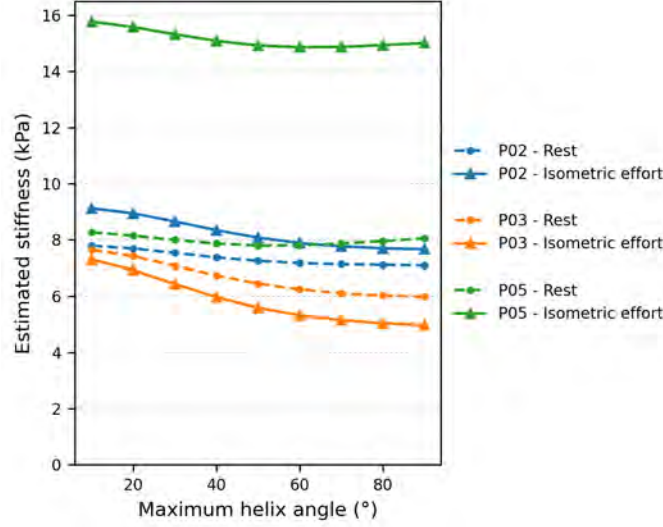
Figure 4.18 Estimated stiffness at rest and during isometric contraction

4.3.2 Transmural change in helix angle

4.3.2.1 Passive inflation

Figure 4.19 shows the impact of the transmural change of helix angle distribution on stress in the myocardium. The normalized distance is equal to 0 at endocardium and 1 at epicardium. As shown in Figure 4.19a, maximum stress increases as the distribution is off-centered. Zero-angle values near the endocardium surface are responsible for highest stress. The maximum stress value is always located in a region with zero-angle value, as illustrated by black circles. Indeed, as illustrated in Figure 4.19b the regions with a lower helix angle exhibit higher stresses. This tendency is slightly less marked at basal and apical region, as observed in the previous study.

The average displacement of the myocardium during inflation is minimal when the helix angle distribution is centered, and increases when off-centered (see Appendix F). Compared to the reference orientation, the deviation is 4.6% when the helix angle is zero at the endocardium (normalized distance: 0), and 7.7% when the helix angle is zero at the endocardium (normalized distance : 1) in average across the three subjects.
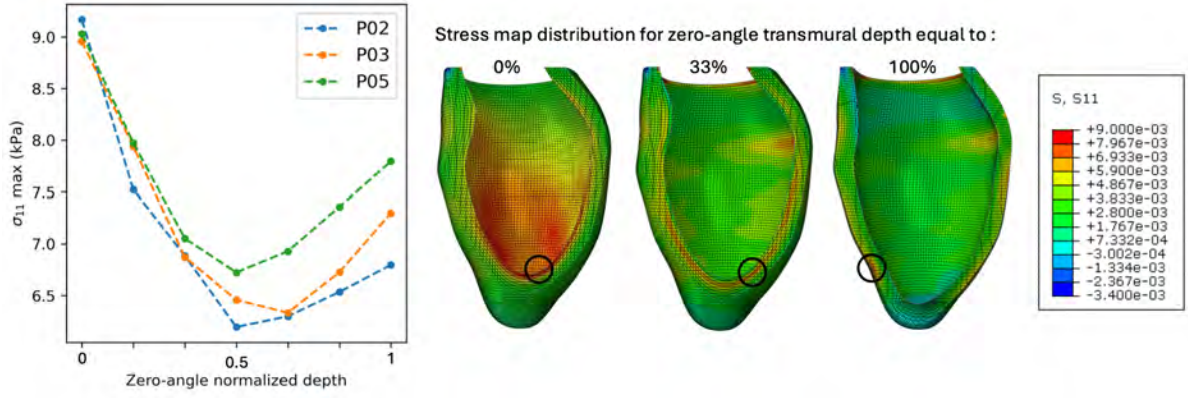
(a) Impact of helix angle transmural distribution on maximal stress
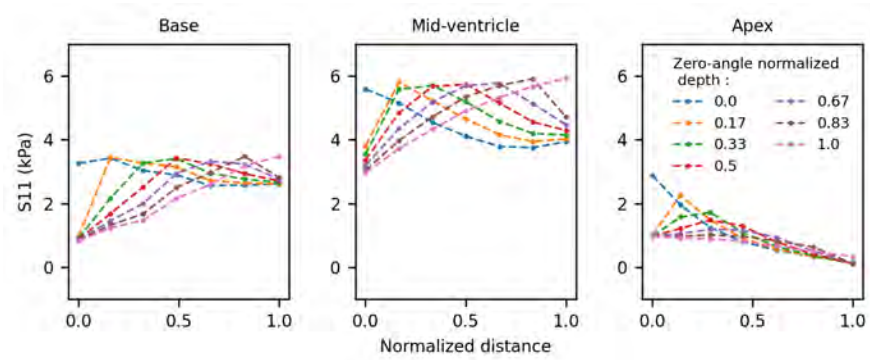
(b) Impact of helix angle transmural distribution on transmural stress values

Figure 4.19 Impact of helix angle transmural distribution on stress in the myocardium

4.3.2.2 Stiffness estimation

The estimated stiffness is minimal when the helix angle distribution is centered or nearly centered. Compared to the reference orientation, the deviation is 5.1% when the helix angle is zero at the endocardium (normalized distance: 0), and 13.5% when the helix angle is zero at the endocardium (normalized distance : 1) in average across the three subjects. The residual error deviates less than 2% in all cases.
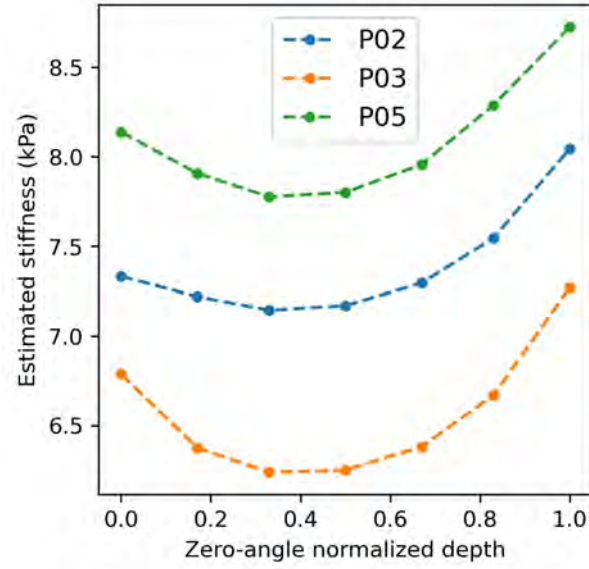
Figure 4.20 Estimated stiffness for different helix angle distribution

4.3.3 Change in maximal helix angle by sector

4.3.3.1 Passive inflation

Figure 4.21a shows impact of fiber orientation in each segment of P03 model. For each segment, the shaded bar corresponds to the maximum stress value in the segment with the reference orientation. The colored bar corresponds to the maximum stress value in the segment when this segment is affected (zero helix angle in the segment). The color of the bar refer to the color of the segment in Figure 4.12. Vertical lines delimit the basal, mid-ventricle, and apical regions as defined in [130]. Except in the basal region, each segment shows an increase in maximal stress when the helix angle is affected. Figure 4.21b illustrates the higher stress values when segment 11 is affected.

As a comparison, the same study is performed with P02 and P05 geometries (Appendix G). For the three geometries, maximum stress in apex is lower than in any other segment. Maximum stress of each segment increases when the segment is affected, except in some segments of basal region. Absolute deviation with reference orientation is equal in average to 33.4%, 22, 1%, and 32, 0% across all segments, respectively for P02, P03, P05. No sector clearly stands out as having a greater or lesser impact consistently across the three models.

The same study on displacement (Appendix G) shows that in each segment of the three geometries, the displacement slightly decreases when helix angle values of the segment are affected. The average deviation across segment is 1.88%, 2.0%, and 1.75% for P02, P03, P05.
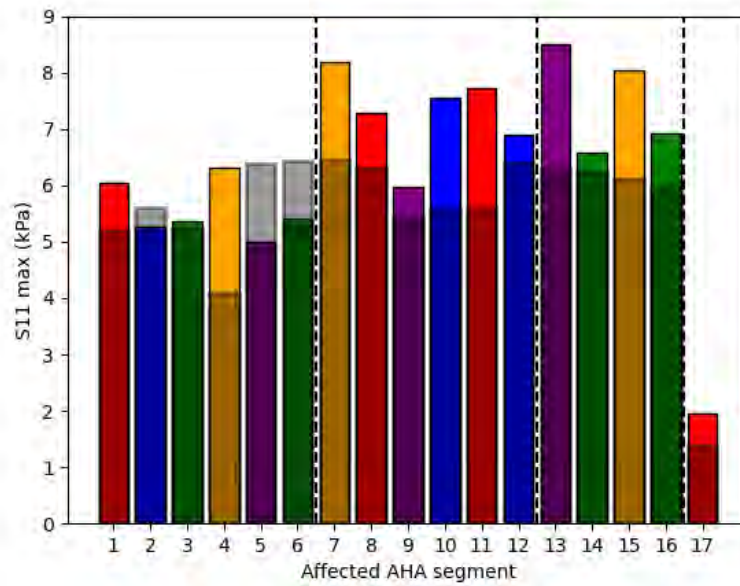
(a) Impact of helix angle on maximum stress
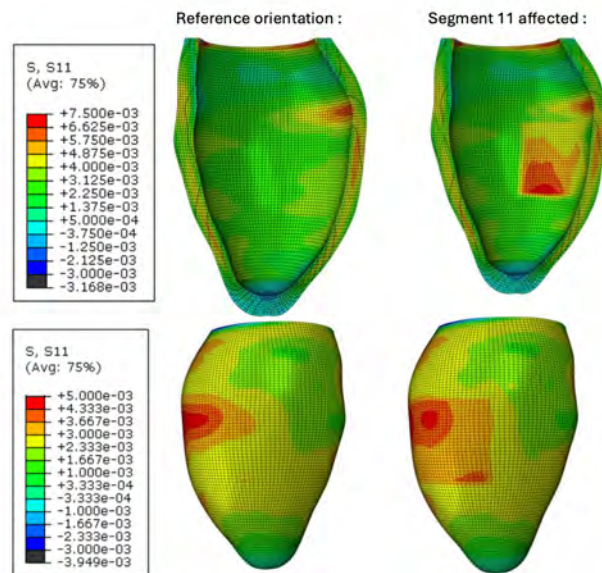
(b) Example of stress values increase

Figure 4.21 Impact of helix angle on stress values in each AHA segment

4.3.3.2 Stiffness estimation

Figure 4.21a shows impact of fiber orientation in each segment for P03 patient-specific stiffness estimation. The black horizontal line show the stiffness estimated value in the reference configuration.
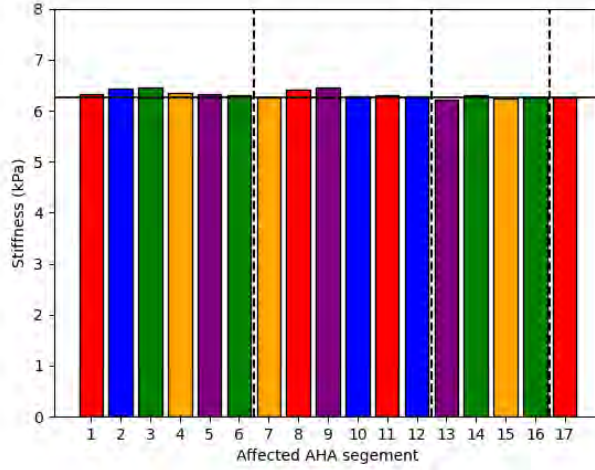
Figure 4.22 Impact of each sector fiber orientation on the global stiffness estimation

Each segment has minimal influence on global stiffness estimation : compared to the reference orientation, stiffness changes by an average of 1.2%. The maximum variation is observed in sector 9 (3.2%) for subject P03, but this sector varies depending on the geometry. The apex has the least influence on the result.

4.3.4 Change in transverse angle

The transverse angle has a minimal impact on the mechanical model compared to the helix angle (see Appendix H). Across simulations (from 0° to 50° maximal transverse angle), the average maximum deviation observed for the three subjects remains low : maximum stress varies by an average of 2.2%, with no consistent increase or decrease, as the trend depends on subjects geometries ; mean displacement shows a slight average reduction of 1.1% across all subjects ; and stiffness decreases slightly by an average of 1.3%.

4.3.5 Reconstruction of fiber architecture from a single DTI slice

4.3.5.1 Passive inflation

Figure 4.23b shows maximum stress in the myocardium obtained with different DTI-slice-based reconstructions. These tiffness estimates are generally higher than the reference orientation, with a mean absolute deviation of 22.19%, 16.42%, and 16.42% for P02, P03 and P05 respectively. Maximum absolute deviation reaches 41.18%, 28.33%, and 21.55% for P02, P03 and P05 respectively.

(a) Maximum stress for different DTI data   (b) Examples of stress distribution maps
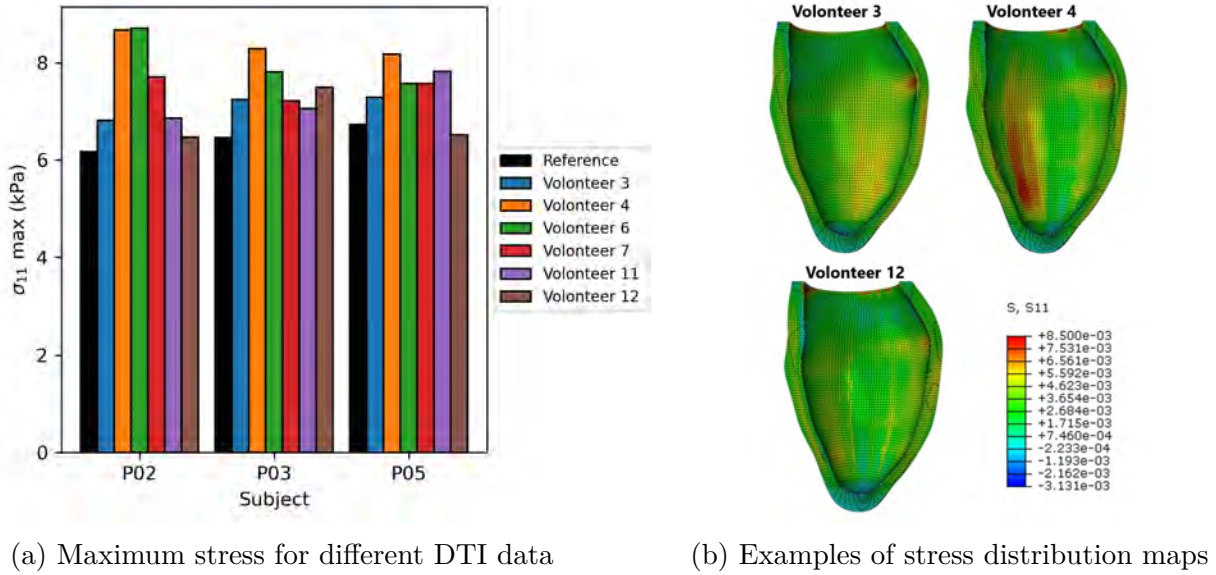
Figure 4.23 Difference in stress for DTI-slice-based reconstructions

4.3.5.2 Stiffness estimation

Figure 4.24 illustrates the variation in estimated stiffness resulting from using different DTI slices to define fiber orientation. The mean absolute deviation with the reference orientation is equal to 5.1%, 7.8%, and 2.9% for P02, P03 and P05 respectively. The maximum absolute deviation reaches 12.2%, 13.1%, and 10.0% for P02, P03 and P05 respectively.

The comparison of stiffness estimation with different DTI-slice-based reconstructions shows significant differences between the slices used (Friedman ANOVA : $p = 0.056$). However, pairwise comparisons show no significant differences between the reference orientation and any of the DTI-slice-based reconstructions (Wilcoxon test with Bonferroni correction : $p > 0.1$).

There are no significant differences between residual error (Friedman ANOVA : $p = 0.42$).
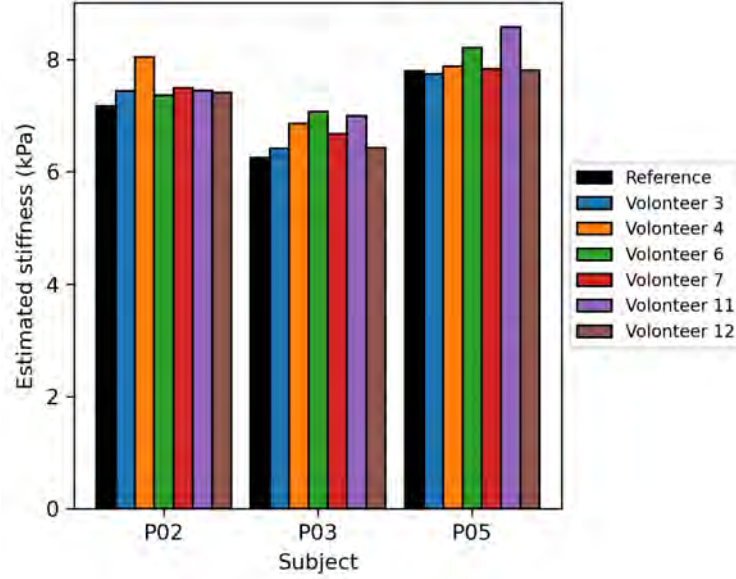
Figure 4.24 Difference in stiffness estimation for different DTI-slice-based reconstructions

As the first study of this Chapter shows a slightly higher impact of fiber orientation in stiffness estimation during isometric contraction compared to rest, the difference between DTI-slice-based reconstructions is also investigated during isometric contraction and is illustrated in Figure 4.25. The mean absolute deviation from the reference orientation during isometric contraction is equal to 9.4%, 7.5%, and 2.2% for P02, P03 and P05 respectively, which is comparable to observed deviation at rest.
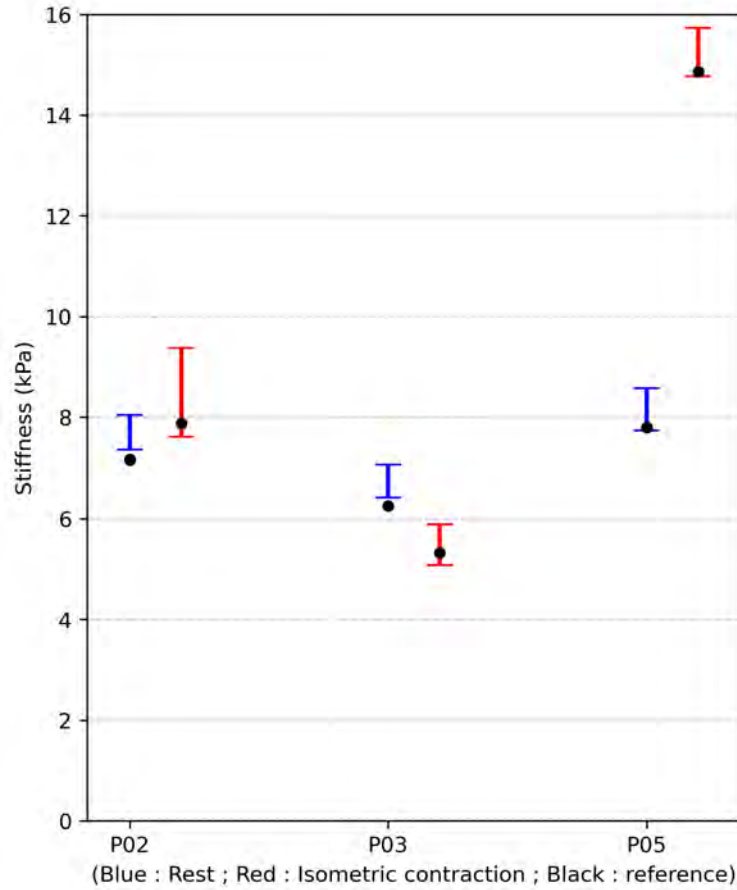
Figure 4.25 Comparaison of stiffness estimation at rest and during isometric contraction

4.4 Discussion

The aim of this study was to assess the impact of fiber architecture on the stiffness estimation. Methods first aim at understanding the mechanical implication of fiber orientation, in order to understand the observed impact on stiffness estimation. This was performed by analyzing the left ventricle passive inflation with different fiber architectures. The impact of fiber architecture on the stiffness estimation was also evaluated.

To identify the most influential characteristics of fiber architecture in the ventricle, sensitivity to multiple parameters was evaluated. First, the helix angle value at endocardium and epicardium, its transmural variation, and its impact by AHA segments were studied. The addition of a non-zero transverse angle was also evaluated. Finally, reconstructions with different mid-ventricle DTI slices of healthy volunteers were compared.

4.4.1 Global change in maximal helix angle

The stress values reported in the previous section are consistent with existing studies [14, 20, 97, 98]. Results shows that lower helix angles ($\leq 30°$) lead to increased stress near the endocardium, with higher maximum stress and less homogeneous stress distribution within the myocardium. In contrast, higher helix angles ($\geq 60°$) result in a more uniform distribution of stress throughout the myocardium. This results are consistent with *Palit et al.* observations [97].

Moreover, as the displacement results show, the motion of left ventricle parallel to the basal plane is greater than vertical displacement : during diastole, the ventricle primarily undergoes radial expansion rather than longitudinal elongation. Circumferentially oriented fibers act to resist this radial motion. It is thus consistent to observe higher stress in these areas.

The results on transmural stress values also support this observation. These transmural stress distributions are consistent with those reported by *Wang et al.* [98], as is the impact of the maximal helix angle on this distribution. The geometric disparities between the ventricle geometry used by *Wang et al.* [98] and those in our study explain the slight differences in transmural stress distribution. Indeed, results show that at different locations within the same ventricle, or between different ventricular geometries, the stress distribution is influenced by the local geometry. This observation has also been previously reported [98, 131].

Displacement analysis shows that lower helix angles favor longitudinal expansion of the ventricle, while higher helix angles inhibit its elongation and slightly promote its radial expansion. As stiffness is higher in the fiber direction than cross-fiber ($b_f = 19, 13$ and $b_t = 10, 67$), these observations are coherent with the myocardium material properties : when the helix angle decreases, the fibers are oriented more circumferentially, stiffening the ventricle in that direction ; conversely, as the helix angle increases, the fibers become more vertically oriented, stiffening the ventricle in the vertical direction. Overall, for low helix angle values, the ventricle is much circularly constrained by the circularly oriented fibers, but very little vertically constrained, increasing the mean displacement. Conversely, at higher angles, the helical distribution of the fibers constrains the ventricle in all directions, reducing the mean displacement.

This observation is consistent with higher values of estimated stiffness reported for lower helix angle values. The stiffness values obtained in this study are consistent with previous findings [5, 8, 12, 20, 21], and the range of variation due to the variation in helix angle is consistent with *Kolawole et al.* [20].

Although lowest values of helix angle tends to increase the estimated stiffness, higher values

have different impacts depending on the left ventricle geometry and the target displacement. Indeed, since fiber orientation influences the direction of displacement, being either more vertical or within the basal plane, global stiffness can vary to compensate for these directional variations. This can explain differences in impact observed between P02, P03, and P05. The stiffness estimates from *Kolawole et al.* [20] show that, for a fixed α, helix angle variation has different impact on stiffness between the different subjects studied.

Notable differences in stiffness values are observed with varying angles. However, it is important to keep in mind that this range of variation remains broader than the physiological range. Indeed, DTI studies have reported that local extrema of helix angle values can reach up to 10° and 90° [16,17], justifying the chosen variation range. However, values implemented in existing models are usually between 45° and 60° at the endocardium, and between −60° and −90° at the epicardium [5, 7, 9, 90, 95, 97, 100].

Residual error is much less affected by variations in helix angle. For subjects P02 and P05, no fiber orientation significantly improves the optimization. For subject P03, however, higher helix angles appear to be more favorable. An examination of the target displacement field (see Appendix I) reveals that this displacement is almost exclusively radial, whereas the simulated displacement includes a non-negligible longitudinal component (see Appendix I). Therefore, vertically oriented fibers (i.e., with higher helix angles) are better suited for this type of motion, which explains the observed reduction in residual error with increasing helix angle.

Stiffness estimates during isometric contraction are consistent with previous study [21]. With P05 model, a clear increase in estimated stiffness is observed during isometric contraction, linked to a significant increase in estimated ventricular pressure. The impact of helix angle on stiffness estimation is slightly greater than at rest, but the differences in impact remain comparable between rest and isometric contraction. This difference is possibly due to increased displacement and pressure during isometric contraction.

4.4.2 Transmural change in helix angle

The results of the transmural helix angle variation study are consistent with the previous analysis (Section 4.4.1). The layers with lower helix angles correspond to regions of higher stress. At the base of the heart, stresses are less affected due to boundary conditions, while at the apex, stresses are lower and also less sensitive to angle variation.

When the helix angle distribution is symmetric and centered across the wall thickness, the ventricle becomes more constrained in all spatial directions. As a result, simulated displace-

ments are reduced, and the stiffness estimated through optimization decreases accordingly.

4.4.3 Change in maximal helix angle by sector

This study aimed at determining wether certain regions in the left ventricle are more sensitive to fiber orientation and require greater precision. Imposing a zero angle is not physiological, but it is, according to previous studies, the choice of orientation that maximizes the impact of fiber orientation. This should allow for the analysis of differences between the AHA segments.

All segments are impacted by their change in fiber orientation. Howerver, the impact differs between segments and left ventricle geometries. Indeed, the strong impact of ventricular geometry on stress distribution has been observed in previous analyses and reported in the literature [98]. No sector stands out for greater or lesser sensitivity to fiber orientation.

The impact of each sector on the global stiffness estimate is negligible.

4.4.4 Change in transverse angle

The aim of this study was to assess the impact of the transverse angle on the mechanical behavior of the ventricle and stiffness estimation, in order to determine whether this angle should be taken into account in the model, or whether it can be approximated to zero. A zero angle corresponds to fibers parallel to the endocardial and epicardial surfaces.

Despite the wide variation range studied, the impact of the transverse angle on both ventricle mechanics and stiffness estimation is minimal. This result is consistent with previous results reported in the literature [101], and justifies its approximation to zero in several mechanical models [5, 20, 122, 124].

However, it is important to note that the chosen angle distribution implies near-zero values in the mid-ventricular region, resulting in fiber orientations that differ only slightly from the reference orientation in this area.

4.4.5 DTI-slice based reconstructions

The four initial studies aimed to assess the sensitivity of the reference orientation, in order to determine how much deviation of different parameters related to it can affect the results. This last study compared the reference orientation with orientations based on DTI measurements, and DTI measurements with each other.

The six different DTI slices lead to pronounced differences in both maximum stress values and stress distribution. Differences are observed between DTI-slices, and compared to the

reference orientation. Consistent with previous findings (Section 4.4.1), the areas of highest stress correspond to low helix angle values.

Although less pronounced than for stress, the impact on the stiffness estimate is also noticeable. As already observed in the four previous studies, the ventricle geometry affects the impact of fiber orientation. Overall, for the three subjects, the Friedman ANOVA test indicates significant differences between the various DTI slices. However, pairwise comparisons reveal that none of the slices significantly deviate from the reference slice. Despite this, when considering subjects individually, deviations in stiffness estimates can exceed 10% for some DTI-slices.

Deviations observed with isometric contraction estimates are comparable to those at rest.

Although deviations in stiffness estimates are not negligible, it is important to note that these variations are small compared to variations that can be caused by pressure differences [20] and material parameters variations (see Chapter 3).

It is important to note, however, that only healthy fiber configurations were evaluated. Nonetheless, deviations, even in the case of pathological configurations, are expected to remain within a similar range to those observed with a maximum helix angle of 10°.

4.4.6 Limits

There are some limitations to this study that must be taken into consideration.

First, the choice of an transversely-isotropic constitutive law leads us to neglect the sheetlet angle (E2A), despite its notable variation within the myocardial tissue [17,32]. However, this approach is important in reducing the number of parameters in the constitutive law, and thus attenuates issues related to non-uniqueness of the solution.

Moreover, all findings of this study are dependent on anisotropy parameter (b_f, b_t, b_{ft}), which dictates the material properties relative to fiber orientation. However, despite significant variation between parameter sets reported in the literature (see Chapter 3), the fiber to cross-fiber stiffness ratio is usually on the order of 2, thus resulting in a comparable impact.

Furthermore, important approximations should be noted in relation to reconstruction from DTI-slices. Firstly, given that only a single slice is available, mid-ventricle data were expanded to base and apex, whereas variation from base to apex has been reported in the literature [16]. Although this reconstruction deviates from the true complete fiber architecture in the ventricle, it provides a rough estimate of the angle values within the physiological range, and thus meets the objective of the study. However, this may have the drawback of propagating slight local errors in the slice throughout the entire height. In addition, as fiber

orientation vary between diastole and systole [29,37,40,132], the choice was made to perform the reconstructions using DTI data acquired during diastasis. However, DTI acquisition were reported to be more accurate at peak systolic [68,69]. This is not expected to impede the results, considering that the main goal is to compare various configurations within the physiological range, and not to determine an accurate patient-specific fiber orientation. Finally, given that only a few patient-specific geometries and a limited number of DTI slices have been studied, the statistical significance is limited.

Lastly, it should be noted that this whole study focuses on passive mechanics of the ventricle and does not address active behavior at all. Fiber orientation has yet been reported to have a stronger impact on the ventricle contraction [18,23].

4.5 Conclusion

In the context of left ventricle myocardial stiffness estimation with finite element models, the implementation of fiber orientation continues to raise many questions. Although fiber orientation has been reported to have a considerable impact on left ventricle mechanics, its impact on stiffness estimation remains little explored. Nevertheless, acquiring comprehensive and patient-specific data of fiber orientation remains challenging.

The study reveals an increase in stress values in the areas of lower values of helix angle, corresponding to circularly oriented fibers. No AHA segment stands out for greater or lesser sensitivity. The stress distribution and maximal values are significantly more affected than the stiffness estimate, yet their effects remain consistent with one another. Overall, helix angle has proven to be an important parameter of fiber orientation from the perspective of both stress distribution and stiffness estimate. In contrast, the transverse angle has a negligible impact.

Stiffness estimates vary considerably between DTI-slice based reconstructions, but no DTI-slice leads to significant deviation from the reference linear $60°/-60°$ orientation. In addition, this variation remains limited compared to material parameter impact.

This study should contribute to a better understanding and assessment of the impact of fiber orientation. This should help guide the selection of an appropriate fiber orientation implementation method, balancing ease of implementation with accuracy of stiffness estimates.

CHAPTER 5   CONCLUSION

This last Chapter briefly recapitulates the key results of the present work, and concludes with its main limitations and some directions for future work.

5.1   Summary of Works

Left ventricular myocardial stiffness is a promising biomarker for the early detection of cardiotoxicity and heart failure. Finite element models provide an effective non-invasive tool for estimating this parameter. However, defining myocardial anisotropy in such models remains challenging. The common assumption of transverse isotropy requires specifying three anisotropy parameters (b_f, b_t, b_{ft}) and fiber orientation to estimate global myocardial stiffness. As the impact of these inputs on stiffness estimation remains poorly characterized, this study aimed to assess their influence.

Chapter 3 reports the impact of each of the three anisotropy parameters on stiffness estimation. The increase in parameter b_f is responsible for the increase in stress along the fiber direction, and decrease of the left ventricle widening during passive inflation. As a consequence, its increase leads to a decrease in the estimated stiffness. The increase parameter in b_t is responsible for the increase in stress along the cross-fiber direction and shear-stress in SN and NS modes. Its increase also leads to a decrease in the left ventricle lengthening during passive inflation, and a decrease in the estimated stiffness. Within the studied range of variation, this parameter proved to be the most influential. The parameter b_{ft} dictates shear material properties in SF, FS, FN, and NF modes. Its impact on passive inflation and stiffness estimation is negligible.

Chapter 3 also provides a comparison of the different set of parameters reported in the literature. Notable differences in the stress–strain curves highlight significant variations in the myocardial mechanical response when using different parameter sets. Consistent with this, stiffness estimates based on different parameter sets reported in the literature also showed significant differences. In agreement with the sensitivity analysis results, parameter b_t appears to play a crucial role in these differences. No model stands out as being more suited in terms of residual error.

As anisotropy parameters dictate the mechanical response relative to fiber orientation, it seems crucial to investigate the impact of this orientation on stiffness estimate. This work is reported in Chapter 4. This study reveals an increase in stress and strain values caused by

the lowering of helix angle values, which corresponds to more circularly-aligned fibers. This also changes ventricular motion during passive inflation, limiting its widening and promoting lengthening. No AHA segment stands out for greater or lesser impact. In contrast to helix angle, transverse angle has minimal effect.

While less pronounced than its impact on stress, fiber orientation still has a notable effect on stiffness estimates. The comparison between DTI-slice-based reconstructions aimed to evaluate variations in stiffness estimates among healthy configurations by comparing a range of different, more "physiologically realistic" fiber configurations. It reveals evident variation between reconstructions, but no DTI-slice leads to a significant deviation of the stiffness estimate compared to the reference linear $60°/-60°$ orientation. Furthermore, it is important to note that the variation associated with fiber orientation (Chapter 4) is considerably lower than that associated with mechanical parameters (Chapter 3).

Given the promising potential of the stiffness estimation method with data acquired during exercise, this study was designed to be applicable to exercise-based estimations. Accordingly, the impact of fiber orientation was evaluated using such data, revealing that its effect on stiffness estimates during exercise is of the same order of magnitude as at rest.

These results are intended to guide the selection of input parameters for implementing myocardial anisotropy. Chapter 3 should help in choosing anisotropy parameters despite their wide variability in the literature. Chapter 4 is expected to support the selection of an appropriate fiber orientation implementation method, according to desired accuracy level for stiffness estimation.

These are important steps in determining standard and pathological values of myocardial passive stiffness. It should contribute to enhance the effectiveness of this biomarker in early detection of cardiotoxicity and heart failure.

5.2   Limitations and future research directions

The present work has several limitations that should be acknowledged, but also suggest potential directions for future research.

Firstly, the interdependence between the anisotropy parameters and fiber orientation should be noted. In the current study, these two sets of inputs were analyzed independently : the sensitivity of stiffness estimation to anisotropy parameters was assessed using a fixed fiber orientation, and vice versa. However, these factors are coupled. The mechanical behavior of the myocardium results from the combined effect of material properties and fiber architecture. For example, given sets of anisotropy parameters may modulate the impact of fiber orientation

on left ventricular mechanics and stiffness estimation, and fiber orientation may, in turn, influence the effect of these parameters. Although the interaction was not investigated, the present work provides a clearer understanding of the individual impact of each factor. The coupling could be the subject of a future study.

In addition, both studies were conducted on a limited number of subjects, restricting their statistical power. However, it provides valuable insights into the general influence of anisotropy parameters and fiber orientation. Extending this study to include more subjects, and thus a greater variety of left ventricular geometries, would provide valuable insights.

Another important aspect to consider is that the pressure values used as loading conditions in the simulations were only estimates. It remains less precise than catheterization measurement. This can have a non-negligible impact on stiffness estimates, due to their high sensitivity to pressure [20]. However, it remains a promising non-invasive approach for incorporating more patient-specific data instead of relying on standard values.

Regarding the use of left ventricle mechanical properties as a biomarker, current methods face challenges related to the uniqueness and variability of parameters estimation. When attempting to estimate all four parameters simultaneously, non-unique solutions undermine the reliability of the results and reduce the relevance of comparisons between patients. This makes it difficult to establish thresholds distinguishing healthy from pathological values. Restricting the estimation process to only one parameter reduces the dimensionality of the problem. However, the present work highlights that the stiffness estimate is significantly dependent on the values chosen for the other parameters. Although this study provides tools to help select the values of the other parameters, this significant dependence on the chosen values remains a limitation for clinical applications. Some studies have chosen to focus on a subset of two parameters. It may represent a practical compromise. However, in this case, the solution is not unique but rather involves a coupling of two parameters. This alternative is also not ideal for clinical applications. Therefore, further work is needed to establish mechanical parameters as an effective biomarker for the early detection of heart failure. A better understanding of the implications of these parameters, as presented in this study, will be a valuable tool to achieve this goal.

While fiber orientation's impact on stiffness estimation was smaller than mechanical parameters, it remains critical, especially for evaluating myocardial stress fields, which can provide valuable diagnostic information. This highlights the critical role of the work that some researchers are currently conducting to implement patient-specific distributions from in-vivo acquisitions. In the present study, only a single DTI slice was used, which is a significant limitation. For now, DTI data acquisition and implementation in the model remain highly

challenging. This makes it difficult to use a fully patient-specific fiber orientation clinically for stiffness estimation in an easy and timely manner. However, ongoing progress in the field could make this increasingly accessible. It is therefore important to understand the required level of precision based on the desired accuracy, both in terms of stress distribution and stiffness estimation. The present study represents a first step in this direction but should be extended with more comprehensive in-vivo DTI measurements. For exemple, comparing the influence of using single versus multiple in-vivo slices would provide valuable insights.

Finally, it would be highly valuable to extend this work to active contraction modeling. Active mechanical properties are also important indicators of cardiac function, and investigating the impact of myocardial anisotropy on these properties could help improve their estimation.

REFERENCES

[1] J. E. Hall and A. C. Guyton, *Textbook of Medical Physiology*, 12nd ed. Philadelphia: Saunders, Elsevier, 2011.

[2] P. Bovendeerd, J. Huyghe, T. Arts, D. Van Campen, and R. Reneman, "Influence of endocardial-epicardial crossover of muscle fibers on left ventricular wall mechanics," *Journal of Biomechanics*, vol. 27, no. 7, pp. 941–951, 1994.

[3] I. J. Legrice, P. J. Hunter, and B. H. Smaill, "Laminar structure of the heart: a mathematical model," *American Journal of Physiology-Heart and Circulatory Physiology*, vol. 272, no. 5, pp. H2466–H2476, 1997.

[4] S. Dokos, B. H. Smaill, A. A. Young, and I. J. LeGrice, "Shear properties of passive ventricular myocardium," *American Journal of Physiology-Heart and Circulatory Physiology*, vol. 283, no. 6, pp. H2650–H2659, 2002.

[5] J. Xi, P. Lamata, S. Niederer, S. Land, W. Shi, X. Zhuang, S. Ourselin, S. G. Duckett, A. K. Shetty, C. A. Rinaldi, D. Rueckert, R. Razavi, and N. P. Smith, "The estimation of patient-specific cardiac diastolic functions from clinical measurements," *Medical Image Analysis*, vol. 17, no. 2, pp. 133–146, 2013.

[6] Y. Zhang, V. Y. Wang, A. E. Morgan, J. Kim, R. Tafreshi, A. W. Wallace, J. M. Guccione, J. W. Weinsaft, L. Ge, and M. B. Ratcliffe, "Finite-element based optimization of left ventricular passive stiffness in normal volunteers and patients after myocardial infarction: Utility of an inverse deformation gradient calculation of regional diastolic strain," *Journal of the Mechanical Behavior of Biomedical Materials*, vol. 119, p. 104431, 2021.

[7] M. Genet, L. C. Lee, R. Nguyen, H. Haraldsson, G. Acevedo-Bolton, Z. Zhang, L. Ge, K. Ordovas, S. Kozerke, and J. M. Guccione, "Distribution of normal human left ventricular myofiber stress at end diastole and end systole: a target for in silico design of heart failure treatments," *Journal of Applied Physiology*, vol. 117, no. 2, pp. 142–152, 2014.

[8] V. Y. Wang, H. Lam, D. B. Ennis, B. R. Cowan, A. A. Young, and M. P. Nash, "Modelling passive diastolic mechanics with quantitative MRI of cardiac structure and function," *Medical Image Analysis*, vol. 13, no. 5, pp. 773–784, 2009.

[9] A. Nasopoulou, A. Shetty, J. Lee, D. Nordsletten, C. A. Rinaldi, P. Lamata, and S. Niederer, "Improved identifiability of myocardial material parameters by an energy-based cost function," *Biomechanics and Modeling in Mechanobiology*, vol. 16, pp. 971–988, 2017.

[10] "Childhood Acute Lymphoblastic Leukemia Treatment (PDQ®) - NCI," 2025. [Online]. Available: https://www.cancer.gov/types/leukemia/hp/child-all-treatment-pdq

[11] S. Armenian and S. Bhatia, "Predicting and Preventing Anthracycline-Related Cardiotoxicity," *American Society of Clinical Oncology Educational Book*, no. 38, pp. 3–12, 2018.

[12] M. Gamba, "Subtle changes in hyperelastic properties of myocardium with cardiotoxicity remodeling from cardiac magnetic resonance," Master's thesis, École Polytechnique de Montréal, 2019. [Online]. Available: https://publications.polymtl.ca/3846/

[13] G. A. Holzapfel and R. W. Ogden, "Constitutive modelling of passive myocardium: a structurally based framework for material characterization," *Philosophical Transactions of the Royal Society A: Mathematical, Physical and Engineering Sciences*, vol. 367, no. 1902, pp. 3445–3475, 2009.

[14] J. M. Guccione, A. D. McCulloch, and L. K. Waldman, "Passive Material Properties of Intact Ventricular Myocardium Determined From a Cylindrical Model," *Journal of Biomechanical Engineering*, vol. 113, no. 1, pp. 42–55, 1991.

[15] D. D. Streeter, H. M. Spotnitz, D. P. Patel, J. Ross, and E. H. Sonnenblick, "Fiber Orientation in the Canine Left Ventricle during Diastole and Systole," *Circulation Research*, vol. 24, no. 3, pp. 339–347, 1969.

[16] H. Lombaert, J.-M. Peyrat, P. Croisille, S. Rapacchi, L. Fanton, F. Cheriet, P. Clarysse, I. Magnin, H. Delingette, and N. Ayache, "Human atlas of the cardiac fiber architecture: Study on a healthy population," *IEEE Transactions on Medical Imaging*, vol. 31, no. 7, pp. 1436–1447, Jul 2012.

[17] J.-M. Peyrat, M. Sermesant, X. Pennec, H. Delingette, Chenyang Xu, E. McVeigh, and N. Ayache, "A Computational Framework for the Statistical Analysis of Cardiac Diffusion Tensors: Application to a Small Database of Canine Hearts," *IEEE Transactions on Medical Imaging*, vol. 26, no. 11, pp. 1500–1514, 2007.

[18] D. Guan, J. Yao, X. Luo, and H. Gao, "Effect of myofibre architecture on ventricular pump function by using a neonatal porcine heart model: from DT-MRI to rule-based methods," *Royal Society Open Science*, vol. 7, no. 4, p. 191655, 2020.

[19] R. Molléro, D. Neumann, M.-M. Rohé, M. Datar, H. Lombaert, N. Ayache, D. Comaniciu, O. Ecabert, M. Chinali, G. Rinelli, X. Pennec, M. Sermesant, and T. Mansi, "Propagation of myocardial fibre architecture uncertainty on electromechanical model parameter estimation: A case study," in *Functional Imaging and Modeling of the Heart. FIMH 2015*, ser. Lecture Notes in Computer Science, H. van Assen, P. Bovendeerd, and T. Delhaas, Eds. Springer, Cham, 2015, vol. 9126, pp. 438–445.

[20] F. O. Kolawole, V. Y. Wang, B. Freytag, M. Loecher, T. E. Cork, M. P. Nash, E. Kuhl, and D. B. Ennis, "Characterizing variability in passive myocardial stiffness in healthy human left ventricles using personalized MRI and finite element modeling," *Scientific Reports*, vol. 15, no. 1, p. 5556, 2025.

[21] F. Mahalatchimy, "Caractérisation du comportement mécanique des tissus cardiaques à l'effort," Master's thesis, École Polytechnique de Montréal, 2023. [Online]. Available: https://publications.polymtl.ca/54858/

[22] J. G. Betts, K. A. Young, J. A. Wise, E. Johnson, B. Poe, D. H. Kruse, O. Korol, J. E. Johnson, M. Womble, and P. DeSaix, "19.1 Heart Anatomy - Anatomy and Physiology | OpenStax," 2013. [Online]. Available: https://openstax.org/books/anatomy-and-physiology-2e/pages/19-1-heart-anatomy

[23] N. M. Colombo, "Numerical Modelling of Ventricular Mechanics: Role of the Myofibre Architecture," PhD Thesis, Politecnico Di Milano, 2014.

[24] R. Avazmohammadi, J. S. Soares, D. S. Li, S. S. Raut, R. C. Gorman, and M. S. Sacks, "A Contemporary Look at Biomechanical Models of Myocardium," *Annual review of biomedical engineering*, vol. 21, pp. 417–442, 2019.

[25] Z. Khalique, P. F. Ferreira, A. D. Scott, S. Nielles-Vallespin, D. N. Firmin, and D. J. Pennell, "Diffusion Tensor Cardiovascular Magnetic Resonance Imaging," *Journal of the American College of Cardiology : Cardiovascular Imaging*, vol. 13, no. 5, pp. 1235–1255, 2020.

[26] I. J. LeGrice, B. H. Smaill, L. Z. Chai, S. G. Edgar, J. B. Gavin, and P. J. Hunter, "Laminar structure of the heart: ventricular myocyte arrangement and connective tissue architecture in the dog," *American Journal of Physiology-Heart and Circulatory Physiology*, vol. 269, no. 2, pp. H571–H582, 1995.

[27] N. Toussaint, C. T. Stoeck, T. Schaeffter, S. Kozerke, M. Sermesant, and P. G. Batchelor, "In vivo human cardiac fibre architecture estimation using shape-based diffusion tensor processing," *Medical Image Analysis*, vol. 17, no. 8, pp. 1243–1255, 2013.

[28] C. Tous, T. L. Gentles, A. A. Young, and B. P. Pontré, "Ex vivo cardiovascular magnetic resonance diffusion weighted imaging in congenital heart disease, an insight into the microstructures of tetralogy of Fallot, biventricular and univentricular systemic right ventricle," *Journal of Cardiovascular Magnetic Resonance*, vol. 22, no. 69, 2020.

[29] K. Moulin, I. A. Verzhbinsky, N. G. Maforo, L. E. Perotti, and D. B. Ennis, "Probing cardiomyocyte mobility with multi-phase cardiac diffusion tensor MRI," *PLOS ONE*, vol. 15, no. 11, p. e0241996, 2020.

[30] F. Varray, I. Mirea, M. Langer, F. Peyrin, L. Fanton, and I. E. Magnin, "Extraction of the 3D local orientation of myocytes in human cardiac tissue using X-ray phase-contrast micro-tomography and multi-scale analysis," *Medical Image Analysis*, vol. 38, pp. 117–132, 2017.

[31] A. J. Wilson, G. B. Sands, I. J. LeGrice, A. A. Young, and D. B. Ennis, "Myocardial mesostructure and mesofunction," *American Journal of Physiology-Heart and Circulatory Physiology*, vol. 323, no. 2, pp. H257–H275, 2022.

[32] A. Palit, G. Turley, S. Bhudia, R. Wellings, and M. Williams, "Assigning myocardial fibre orientation to a computational biventricular human heart model," in *The 15th International Conference on Biomedical Engineering.* Springer International Publishing, 2014, vol. 43, pp. 144–147.

[33] L. J. Healy, Y. Jiang, and E. W. Hsu, "Quantitative comparison of myocardial fiber structure between mice, rabbit, and sheep using diffusion tensor cardiovascular magnetic resonance," *Journal of Cardiovascular Magnetic Resonance*, vol. 13, no. 1, p. 74, 2011.

[34] P. Cabanis, J. Magat, J. Rodriguez-Padilla, G. Ramlugun, M. Yon, Y. Bihan-Poudec, N. Pallares-Lupon, F. Vaillant, P. Pasdois, P. Jais, P. Dos-Santos, M. Constantin, D. Benoist, L. Pourtau, V. Dubes, J. Rogier, L. Labrousse, M. Haissaguerre, O. Bernus, B. Quesson, R. Walton, J. Duchateau, E. Vigmond, and V. Ozenne, "Cardiac structure discontinuities revealed by ex-vivo microstructural characterization. A focus on the basal inferoseptal left ventricle region," *Journal of Cardiovascular Magnetic Resonance*, vol. 25, no. 1, p. 78, 2023.

[35] S. Wang, Y. Wang, Z. Li, Y. Zhao, Y. Zhang, and F. Varray, "Investigating the three-dimensional myocardial micro-architecture in the laminar structure using X-ray phase-contrast microtomography," *Scientific Reports*, vol. 14, no. 1, p. 14329, 2024.

[36] S. Wang, F. Varray, W. Liu, P. Clarysse, and I. E. Magnin, "Measurement of local orientation of cardiomyocyte aggregates in human left ventricle free wall samples using X-ray phase-contrast microtomography," *Medical Image Analysis*, vol. 75, p. 102269, 2022.

[37] C. Von Deuster, E. Sammut, L. Asner, D. Nordsletten, P. Lamata, C. T. Stoeck, S. Kozerke, and R. Razavi, "Studying Dynamic Myofiber Aggregate Reorientation in Dilated Cardiomyopathy Using In Vivo Magnetic Resonance Diffusion Tensor Imaging," *Circulation: Cardiovascular Imaging*, vol. 9, no. 10, p. e005018, 2016.

[38] J. Chen, W. Liu, H. Zhang, L. Lacy, X. Yang, S.-K. Song, S. A. Wickline, and X. Yu, "Regional ventricular wall thickening reflects changes in cardiac fiber and sheet structure during contraction: quantification with diffusion tensor MRI," *American Journal of Physiology-Heart and Circulatory Physiology*, vol. 289, no. 5, pp. H1898–H1907, 2005.

[39] G. Seemann, D. U. J. Keller, D. L. Weiss, and O. Dossel, "Modeling human ventricular geometry and fiber orientation based on diffusion tensor MRI," *Computers in Cardiology*, pp. 801–804, 2006.

[40] S. Nielles-Vallespin, Z. Khalique, P. F. Ferreira, R. De Silva, A. D. Scott, P. Kilner, L.-A. McGill, A. Giannakidis, P. D. Gatehouse, D. Ennis, E. Aliotta, M. Al-Khalil, P. Kellman, D. Mazilu, R. S. Balaban, D. N. Firmin, A. E. Arai, and D. J. Pennell, "Assessment of Myocardial Microstructural Dynamics by In Vivo Diffusion Tensor Cardiac Magnetic Resonance," *Journal of the American College of Cardiology*, vol. 69, no. 6, pp. 661–676, 2017.

[41] D. E. Sosnovik, R. Wang, G. Dai, T. Wang, E. Aikawa, M. Novikov, A. Rosenzweig, R. J. Gilbert, and V. J. Wedeen, "Diffusion Spectrum MRI Tractography Reveals the Presence of a Complex Network of Residual Myofibers in Infarcted Myocardium," *Circulation: Cardiovascular Imaging*, vol. 2, no. 3, pp. 206–212, 2009.

[42] G. T. Armstrong, Q. Liu, Y. Yasui, J. P. Neglia, W. Leisenring, L. L. Robison, and A. C. Mertens, "Late Mortality Among 5-Year Survivors of Childhood Cancer: A Summary From the Childhood Cancer Survivor Study," *Journal of Clinical Oncology*, vol. 27, no. 14, pp. 2328–2338, 2009.

[43] A. Khanna, P. Pequeno, S. Gupta, T. Paaladinesh, D. S. Lee, H. Abdel-Qadir, and P. C. Nathan, "Increased Risk of All Cardiovascular Disease Subtypes Among Childhood Cancer Survivors," *Circulation*, vol. 140, pp. 1041–1043, 2019.

[44] K. Chatterjee, J. Zhang, N. Honbo, and J. S. Karliner, "Doxorubicin Cardiomyopathy," *Cardiology*, vol. 115, no. 2, pp. 155–162, 2010.

[45] M. Aissiou, D. Périé, F. Cheriet, N. S. Dahdah, C. Laverdière, and D. Curnier, "Imaging of early modification in cardiomyopathy: the doxorubicin-induced model," *The International Journal of Cardiovascular Imaging*, vol. 29, no. 7, pp. 1459–1476, 2013.

[46] M. Aissiou, D. Curnier, M. Caru, T. Hafyane, L. Leleu, M. Krajinovic, C. Laverdière, D. Sinnett, G. Andelfinger, F. Cheriet, and D. Périé, "Detection of doxorubicin-induced cardiotoxicity using myocardial T1 and T2 relaxation times in childhood acute lymphoblastic leukemia survivors," *The International Journal of Cardiovascular Imaging*, vol. 38, no. 4, pp. 873–882, 2021.

[47] R. Jurcut, H. Wildiers, J. Ganame, J. D'hooge, R. Paridaens, and J.-U. Voigt, "Detection and monitoring of cardiotoxicity—what does modern cardiology offer?" *Supportive Care in Cancer*, vol. 16, no. 5, pp. 437–445, 2008.

[48] V. W.-y. Li, D. K.-l. Cheuk, F. W.-t. Cheng, J. Y.-k. Yang, J. P.-w. Yau, K. K.-h. Ho, C.-k. Li, R. C.-h. Li, H.-l. Yuen, A. S.-c. Ling, G. C.-f. Chan, and Y.-f. Cheung, "Myocardial stiffness as assessed by diastolic wall strain in adult survivors of childhood leukaemias with preserved left ventricular ejection fraction," *European Heart Journal – Cardiovascular Imaging*, 2016.

[49] E. Smibert, J. B. Carlin, S. Vidmar, L. C. Wilkinson, M. Newton, and R. G. Weintraub, "Exercise echocardiography reflects cumulative anthracycline exposure during childhood," *Pediatric Blood & Cancer*, vol. 42, no. 7, pp. 556–562, 2004.

[50] M. Hauser, B. Gibson, and N. Wilson, "Diagnosis of anthracycline-induced late cardiomyopathy by exercise-spiroergometry and stress-echocardiography," *European Journal of Pediatrics*, vol. 160, no. 10, pp. 607–610, 2001.

[51] L. Mabudian, J. H. Jordan, W. Bottinor, and W. G. Hundley, "Cardiac MRI assessment of anthracycline-induced cardiotoxicity," *Frontiers in Cardiovascular Medicine*, vol. 9, p. 903719, 2022.

[52] H. Sawaya, I. A. Sebag, J. C. Plana, J. L. Januzzi, B. Ky, V. Cohen, S. Gosavi, J. R. Carver, S. E. Wiegers, R. P. Martin, M. H. Picard, R. E. Gerszten, E. F. Halpern,

J. Passeri, I. Kuter, and M. Scherrer-Crosbie, "Early Detection and Prediction of Cardiotoxicity in Chemotherapy-Treated Patients," *The American Journal of Cardiology*, vol. 107, no. 9, pp. 1375–1380, 2011.

[53] C. P. Houbois, M. Nolan, E. Somerset, T. Shalmon, M. Esmaeilzadeh, M. M. Lamacie, E. Amir, C. Brezden-Masley, C. A. Koch, Y. Thevakumaran, A. T. Yan, T. H. Marwick, B. J. Wintersperger, and P. Thavendiranathan, "Serial Cardiovascular Magnetic Resonance Strain Measurements to Identify Cardiotoxicity in Breast Cancer," *JACC: Cardiovascular Imaging*, vol. 14, no. 5, pp. 962–974, 2021.

[54] E. Uwase, M. Caru, D. Curnier, M. Abasq Meng, G. Andelfinger, M. Krajinovic, C. Laverdière, D. Sinnett, and D. Périé, "Cardiac Mechanical Performance Assessment at Different Levels of Exercise in Childhood Acute Lymphoblastic Leukemia Survivors," *Journal of Pediatric Hematology/Oncology*, vol. 45, no. 5, pp. 247–255, 2023.

[55] W. Liu and Z. Wang, "Current Understanding of the Biomechanics of Ventricular Tissues in Heart Failure," *Bioengineering*, vol. 7, no. 1, p. 2, 2019.

[56] Y. Sakata, T. Ohtani, Y. Takeda, K. Yamamoto, and T. Mano, "Left Ventricular Stiffening as Therapeutic Target for Heart Failure With Preserved Ejection Fraction," *Circulation Journal*, vol. 77, no. 4, pp. 886–892, 2013.

[57] M. R. Zile, C. F. Baicu, and W. H. Gaasch, "Diastolic Heart Failure — Abnormalities in Active Relaxation and Passive Stiffness of the Left Ventricle," *New England Journal of Medicine*, vol. 350, no. 19, pp. 1953–1959, 2004.

[58] A. Borbély, J. Van Der Velden, Z. Papp, J. G. Bronzwaer, I. Edes, G. J. Stienen, and W. J. Paulus, "Cardiomyocyte Stiffness in Diastolic Heart Failure," *Circulation*, vol. 111, no. 6, pp. 774–781, 2005.

[59] R. Emig, C. M. Zgierski-Johnston, V. Timmermann, A. J. Taberner, M. P. Nash, P. Kohl, and R. Peyronnet, "Passive myocardial mechanical properties: meaning, measurement, models," *Biophysical Reviews*, vol. 13, no. 5, pp. 587–610, 2021.

[60] T. Arts, K. D. Costa, J. W. Covell, and A. D. McCulloch, "Relating myocardial laminar architecture to shear strain and muscle fiber orientation," *American Journal of Physiology-Heart and Circulatory Physiology*, vol. 280, no. 5, pp. H2222–H2229, 2001.

[61] V. Y. Wang, A. A. Young, B. R. Cowan, and M. P. Nash, "Changes in In Vivo Myocardial Tissue Properties Due to Heart Failure," in *Functional Imaging and Modeling of*

the Heart, S. Ourselin, D. Rueckert, and N. Smith, Eds. Berlin, Heidelberg: Springer Berlin Heidelberg, 2013, vol. 7945, pp. 216–223.

[62] A. Krishnamurthy, C. T. Villongco, J. Chuang, L. R. Frank, V. Nigam, E. Belezzuoli, P. Stark, D. E. Krummen, S. Narayan, J. H. Omens, A. D. McCulloch, and R. C. Kerckhoffs, "Patient-specific models of cardiac biomechanics," *Journal of Computational Physics*, vol. 244, pp. 4–21, 2013.

[63] J. Prince and J. Links, *Medical Imaging Signals and Systems*, ser. Pearson Prentice Hall bioengineering. Pearson Prentice Hall, 2006.

[64] J. P. Ridgway, "Cardiovascular magnetic resonance physics for clinicians: part I," *Journal of Cardiovascular Magnetic Resonance*, vol. 12, no. 1, p. 71, 2010.

[65] O. Bieri and K. Scheffler, "Fundamentals of balanced steady state free precession MRI: Fundamentals of Balanced SSFP MRI," *Journal of Magnetic Resonance Imaging*, vol. 38, no. 1, pp. 2–11, 2013.

[66] L. E. Perotti, I. A. Verzhbinsky, K. Moulin, T. E. Cork, M. Loecher, D. Balzani, and D. B. Ennis, "Estimating cardiomyofiber strain in vivo by solving a computational model," *Medical Image Analysis*, vol. 68, p. 101932, 2021.

[67] C. Tous, "Evaluation of myocardial microstructure in congenital heart diseases with diffusion magnetic resonance imaging," PhD Thesis, University of Auckland, 2019. [Online]. Available: https://doi.org/10.13140/RG.2.2.29113.80480

[68] C. T. Stoeck, C. Von Deuster, T. Fleischmann, M. Lipiski, N. Cesarovic, and S. Kozerke, "Direct comparison of in vivo versus postmortem second-order motion-compensated cardiac diffusion tensor imaging," *Magnetic Resonance in Medicine*, vol. 79, no. 4, pp. 2265–2276, 2018.

[69] E. Aliotta, K. Moulin, P. Magrath, and D. B. Ennis, "Quantifying precision in cardiac diffusion tensor imaging with second-order motion-compensated convex optimized diffusion encoding," *Magnetic Resonance in Medicine*, vol. 80, no. 3, pp. 1074–1087, 2018.

[70] D. F. Scollan, A. Holmes, R. Winslow, and J. Forder, "Histological validation of myocardial microstructure obtained from diffusion tensor magnetic resonance imaging," *American Journal of Physiology-Heart and Circulatory Physiology*, vol. 275, no. 6, pp. H2308–H2318, 1998.

[71] F. C. Yin, R. K. Strumpf, P. H. Chew, and S. L. Zeger, "Quantification of the mechanical properties of noncontracting canine myocardium under simultaneous biaxial loading," *Journal of Biomechanics*, vol. 20, no. 6, pp. 577–589, 1987.

[72] B. Smaill and P. Hunter, "Structure and Function of the Diastolic Heart: Material Properties of Passive Myocardium," in *Theory of Heart*, L. Glass, P. Hunter, and A. McCulloch, Eds. New York, NY: Springer New York, 1991, pp. 1–29, series Title: Institute for Nonlinear Science.

[73] V. Novak, F. Yin, and J. Humphrey, "Regional mechanical properties of passive myocardium," *Journal of Biomechanics*, vol. 27, no. 4, pp. 403–412, 1994.

[74] G. Sommer, A. J. Schriefl, M. Andrä, M. Sacherer, C. Viertler, H. Wolinski, and G. A. Holzapfel, "Biomechanical properties and microstructure of human ventricular myocardium," *Acta Biomaterialia*, vol. 24, pp. 172–192, 2015.

[75] J. H. Omens, D. A. MacKenna, and A. D. McCulloch, "Measurement of strain and analysis of stress in resting rat left ventricular myocardium," *Journal of Biomechanics*, vol. 26, no. 6, pp. 665–676, 1993.

[76] R. Avazmohammadi, D. S. Li, T. Leahy, E. Shih, J. S. Soares, J. H. Gorman, R. C. Gorman, and M. S. Sacks, "An Integrated Inverse Model-Experimental Approach to Determine Soft Tissue Three-Dimensional Constitutive Properties: Application to Post-Infarcted Myocardium," *Biomechanics and modeling in mechanobiology*, vol. 17, no. 1, pp. 31–53, 2018.

[77] E. McEvoy, G. A. Holzapfel, and P. McGarry, "Compressibility and Anisotropy of the Ventricular Myocardium: Experimental Analysis and Microstructural Modeling," *Journal of Biomechanical Engineering*, vol. 140, no. 8, p. 081004, 2018.

[78] N. Tueni, J.-M. Allain, and M. Genet, "On the structural origin of the anisotropy in the myocardium: Multiscale modeling and analysis," *Journal of the Mechanical Behavior of Biomedical Materials*, vol. 138, p. 105600, 2023.

[79] H. Ashikaga, B. A. Coppola, K. G. Yamazaki, F. J. Villarreal, J. H. Omens, and J. W. Covell, "Changes in regional myocardial volume during the cardiac cycle: implications for transmural blood flow and cardiac structure," *American Journal of Physiology-Heart and Circulatory Physiology*, vol. 295, no. 2, pp. H610–H618, 2008.

[80] H. Oudin, *Méthode des éléments finis*, École d'ingénieurs centrale nantes ed., Nantes, France, 2008.

[81] P. M. Nielsen, I. J. Le Grice, B. H. Smaill, and P. J. Hunter, "Mathematical model of geometry and fibrous structure of the heart," *American Journal of Physiology-Heart and Circulatory Physiology*, vol. 260, no. 4, pp. H1365–H1378, 1991.

[82] J. M. Guccione, K. D. Costa, and A. D. McCulloch, "Finite element stress analysis of left ventricular mechanics in the beating dog heart," *Journal of Biomechanics*, vol. 28, no. 10, pp. 1167–1177, 1995.

[83] K. L. Sack, E. Aliotta, D. B. Ennis, J. S. Choy, G. S. Kassab, J. M. Guccione, and T. Franz, "Construction and Validation of Subject-Specific Biventricular Finite-Element Models of Healthy and Failing Swine Hearts From High-Resolution DT-MRI," *Frontiers in Physiology*, vol. 9, p. 539, 2018.

[84] J. D. Lemmon and A. P. Yoganathan, "Three-Dimensional Computational Model of Left Heart Diastolic Function With Fluid–Structure Interaction," *Journal of Biomechanical Engineering*, vol. 122, no. 2, pp. 109–117, 2000.

[85] P. Hunter, A. McCulloch, and H. Ter Keurs, "Modelling the mechanical properties of cardiac muscle," *Progress in Biophysics and Molecular Biology*, vol. 69, no. 2-3, pp. 289–331, 1998.

[86] S. Marchesseau, H. Delingette, M. Sermesant, and N. Ayache, "Fast parameter calibration of a cardiac electromechanical model from medical images based on the unscented transform," *Biomechanics and Modeling in Mechanobiology*, vol. 12, no. 4, pp. 815–831, 2013.

[87] B. Baillargeon, N. Rebelo, D. D. Fox, R. L. Taylor, and E. Kuhl, "The Living Heart Project: A robust and integrative simulator for human heart function," *European Journal of Mechanics - A/Solids*, vol. 48, pp. 38–47, 2014.

[88] R. C. P. Kerckhoffs, P. H. M. Bovendeerd, J. C. S. Kotte, F. W. Prinzen, K. Smits, and T. Arts, "Homogeneity of Cardiac Contraction Despite Physiological Asynchrony of Depolarization: A Model Study," *Annals of Biomedical Engineering*, vol. 31, no. 5, pp. 536–547, 2003.

[89] L. Geerts, R. Kerckhoffs, P. Bovendeerd, and T. Arts, "Towards Patient Specific Models of Cardiac Mechanics: A Sensitivity Study," in *Lecture notes in computer science*, I. E. Magnin, J. Montagnat, P. Clarysse, J. Nenonen, and T. Katila, Eds. Berlin, Heidelberg: Springer Berlin Heidelberg, 2003, vol. 2674, pp. 81–90.

[90] H. Osnes and J. Sundnes, "Uncertainty Analysis of Ventricular Mechanics Using the Probabilistic Collocation Method," *IEEE Transactions on Biomedical Engineering*, vol. 59, no. 8, pp. 2171–2179, 2012.

[91] J. Rijcken, P. H. M. Bovendeerd, A. J. G. Schoofs, D. H. Van Campen, and T. Arts, "Optimization of Cardiac Fiber Orientation for Homogeneous Fiber Strain During Ejection," *Annals of Biomedical Engineering*, vol. 27, no. 3, pp. 289–297, 1999.

[92] S. Ubbink, P. Bovendeerd, T. Delhaas, T. Arts, and F. Van De Vosse, "Towards model-based analysis of cardiac MR tagging data: Relation between left ventricular shear strain and myofiber orientation," *Medical Image Analysis*, vol. 10, no. 4, pp. 632–641, 2006.

[93] T. P. Usyk, R. Mazhari, and A. D. Mcculloch, "Effect of Laminar Orthotropic Myofiber Architecture on Regional Stress and Strain in the Canine Left Ventricle," *Journal of Elasticity*, vol. 61, pp. 143–164, 2000.

[94] M. Genet, L. C. Lee, E. Kuhl, and J. Guccione, "Abaqus/Standard-based quantification of human cardiac mechanical properties." Dassault Systèmes Simulia Corp., presented at the 2014 SIMULIA Community Conference.

[95] H. Gao, B. E. Griffith, D. Carrick, C. McComb, C. Berry, and X. Luo, "Initial experience with a dynamic imaging-derived immersed boundary model of human left ventricle," in *Functional Imaging and Modeling of the Heart. FIMH 2013*, ser. Lecture Notes in Computer Science, S. Ourselin, D. Rueckert, and N. Smith, Eds. Berlin, Heidelberg: Springer, 2013, vol. 7945, pp. 11–18.

[96] M. J. Moulton, L. L. Creswell, S. W. Downing, R. L. Actis, B. A. Szabó, and M. K. Pasque, "Myocardial material property determination in the in vivo heart using magnetic resonance imaging," *The International Journal of Cardiac Imaging*, vol. 12, no. 3, pp. 153–167, 1996.

[97] A. Palit, S. K. Bhudia, T. N. Arvanitis, G. A. Turley, and M. A. Williams, "Computational modelling of left-ventricular diastolic mechanics: Effect of fibre orientation and right-ventricle topology," *Journal of Biomechanics*, vol. 48, no. 4, pp. 604–612, 2015.

[98] H. M. Wang, H. Gao, X. Y. Luo, C. Berry, B. E. Griffith, R. W. Ogden, and T. J. Wang, "Structure-based finite strain modelling of the human left ventricle in diastole," *International Journal for Numerical Methods in Biomedical Engineering*, vol. 29, no. 1, pp. 83–103, 2013.

[99] K. F. Augenstein, B. R. Cowan, I. J. LeGrice, P. M. F. Nielsen, and A. A. Young, "Method and Apparatus for Soft Tissue Material Parameter Estimation Using Tissue Tagged Magnetic Resonance Imaging," *Journal of Biomechanical Engineering*, vol. 127, no. 1, pp. 148–157, 2005.

[100] E. W. Remme, P. J. Hunter, O. Smiseth, C. Stevens, S. I. Rabben, H. Skulstad, and B. Angelsen, "Development of an in vivo method for determining material properties of passive myocardium," *Journal of Biomechanics*, vol. 37, no. 5, pp. 669–678, 2004.

[101] R. Rodríguez-Cantano, J. Sundnes, and M. E. Rognes, "Uncertainty in cardiac myofiber orientation and stiffnesses dominate the variability of left ventricle deformation response," *International Journal for Numerical Methods in Biomedical Engineering*, vol. 35, no. 5, p. e3178, 2019.

[102] P. Lamata, M. Sinclair, E. Kerfoot, A. Lee, A. Crozier, B. Blazevic, S. Land, A. J. Lewandowski, D. Barber, S. Niederer, and N. Smith, "An automatic service for the personalization of ventricular cardiac meshes," *Journal of the Royal Society Interface*, vol. 11, no. 91, p. 20131023, 2014.

[103] J. C. Walker, M. B. Ratcliffe, P. Zhang, A. W. Wallace, B. Fata, E. W. Hsu, D. Saloner, and J. M. Guccione, "MRI-based finite-element analysis of left ventricular aneurysm," *American Journal of Physiology-Heart and Circulatory Physiology*, vol. 289, no. 2, pp. H692–H700, 2005.

[104] T. Arts, T. Delhaas, P. Bovendeerd, X. Verbeek, and F. W. Prinzen, "Adaptation to mechanical load determines shape and properties of heart and circulation: the CircAdapt model," *American Journal of Physiology-Heart and Circulatory Physiology*, vol. 288, no. 4, pp. H1943–H1954, 2005.

[105] J. D. Humphrey, R. K. Strumpf, and F. C. P. Yin, "Determination of a Constitutive Relation for Passive Myocardium: I. A New Functional Form," *Journal of Biomechanical Engineering*, vol. 112, no. 3, pp. 333–339, 1990.

[106] I. Legrice, P. Hunter, A. Young, and B. Smaill, "The architecture of the heart: a data–based model," *Philosophical Transactions of the Royal Society of London. Series A: Mathematical, Physical and Engineering Sciences*, vol. 359, no. 1783, pp. 1217–1232, 2001.

[107] M. P. Nash and P. J. Hunter, "Computational Mechanics of the Heart," in *Cardiovascular Soft Tissue Mechanics*, S. C. Cowin and J. D. Humphrey, Eds. Dordrecht: Kluwer Academic Publishers, 2004, pp. 113–141.

[108] A. Horowitz, Y. Lanir, F. C. P. Yin, M. Perl, I. Sheinman, and R. K. Strumpf, "Structural Three-Dimensional Constitutive Law for the Passive Myocardium," *Journal of Biomechanical Engineering*, vol. 110, no. 3, pp. 200–207, 1988.

[109] R. Avazmohammadi, M. Hill, M. Simon, W. Zhang, and M. Sacks, "A novel constitutive model for passive right ventricular myocardium: Evidence for myofiber-collagen fiber mechanical coupling," *Biomechanics and modeling in mechanobiology*, vol. 16, no. 2, pp. 561–581, 2017.

[110] H. Schmid, M. P. Nash, A. A. Young, and P. J. Hunter, "Myocardial Material Parameter Estimation—A Comparative Study for Simple Shear," *Journal of Biomechanical Engineering*, vol. 128, no. 5, pp. 742–750, 2006.

[111] F. J. Vetter and A. D. McCulloch, "Three-dimensional analysis of regional cardiac function: a model of rabbit ventricular anatomy," *Progress in Biophysics and Molecular Biology*, vol. 69, no. 2-3, pp. 157–183, 1998.

[112] J. D. Bayer, R. C. Blake, G. Plank, and N. A. Trayanova, "A Novel Rule-Based Algorithm for Assigning Myocardial Fiber Orientation to Computational Heart Models," *Annals of Biomedical Engineering*, vol. 40, no. 10, pp. 2243–2254, 2012.

[113] K. Takayama, T. Ashihara, T. Ijiri, T. Igarashi, R. Haraguchi, and K. Nakazawa, "A Sketch-Based Interface for Modeling Myocardial Fiber Orientation that Considers the Layered Structure of the Ventricles," *The Journal of Physiological Sciences*, vol. 58, no. 7, pp. 487–492, 2008.

[114] J. Wong and E. Kuhl, "Generating fibre orientation maps in human heart models using Poisson interpolation," *Computer Methods in Biomechanics and Biomedical Engineering*, vol. 17, no. 11, pp. 1217–1226, 2014.

[115] W. Kroon, T. Delhaas, P. Bovendeerd, and T. Arts, "Computational analysis of the myocardial structure: Adaptation of cardiac myofiber orientations through deformation," *Medical Image Analysis*, vol. 13, no. 2, pp. 346–353, 2009.

[116] D. Alexander, C. Pierpaoli, P. Basser, and J. Gee, "Spatial transformations of diffusion tensor magnetic resonance images," *IEEE Transactions on Medical Imaging*, vol. 20, no. 11, pp. 1131–1139, 2001.

[117] J. Stimm, C. Guenthner, S. Kozerke, and C. T. Stoeck, "Comparison of interpolation methods of predominant cardiomyocyte orientation from in vivo and ex vivo cardiac diffusion tensor imaging data," *NMR in Biomedicine*, vol. 35, no. 5, p. e4667, 2022.

[118] J. Huang, P. F. Ferreira, L. Wang, Y. Wu, A. I. Aviles-Rivero, C.-B. Schönlieb, A. D. Scott, Z. Khalique, M. Dwornik, R. Rajakulasingam, R. De Silva, D. J. Pennell, S. Nielles-Vallespin, and G. Yang, "Deep learning-based diffusion tensor cardiac magnetic resonance reconstruction: a comparison study," *Scientific Reports*, vol. 14, no. 1, p. 5658, 2024.

[119] F. J. Vetter and A. D. McCulloch, "Three-Dimensional Stress and Strain in Passive Rabbit Left Ventricle: A Model Study," *Annals of Biomedical Engineering*, vol. 28, no. 7, pp. 781–792, 2000.

[120] H. Gao, W. G. Li, L. Cai, C. Berry, and X. Y. Luo, "Parameter estimation in a Holzapfel–Ogden law for healthy myocardium," *Journal of Engineering Mathematics*, vol. 95, no. 1, pp. 231–248, 2015.

[121] A. Lazarus, D. Dalton, D. Husmeier, and H. Gao, "Sensitivity analysis and inverse uncertainty quantification for the left ventricular passive mechanics," *Biomechanics and Modeling in Mechanobiology*, vol. 21, no. 3, pp. 953–982, Jun. 2022.

[122] A. Nikou, R. C. Gorman, and J. F. Wenk, "Sensitivity of left ventricular mechanics to myofiber architecture: A finite element study," *Proceedings of the Institution of Mechanical Engineers, Part H: Journal of Engineering in Medicine*, vol. 230, no. 6, pp. 594–598, 2016.

[123] M. Peirlinck, K. L. Sack, P. De Backer, P. Morais, P. Segers, T. Franz, and M. De Beule, "Kinematic boundary conditions substantially impact in silico ventricular function," *International Journal for Numerical Methods in Biomedical Engineering*, vol. 35, no. 1, p. e3151, 2019.

[124] A. Palit, S. K. Bhudia, T. N. Arvanitis, G. A. Turley, and M. A. Williams, "In vivo estimation of passive biomechanical properties of human myocardium," *Medical & Biological Engineering & Computing*, vol. 56, no. 9, pp. 1615–1631, 2018.

[125] Dassault Systèmes, *Abaqus 2022 Documentation*, Dassault Systèmes Simulia Corp., 2022, https://www.3ds.com/products-services/simulia/products/abaqus/.

[126] "ABAQUS Analysis User's Manual (V6.6)." [Online]. Available: https://classes.engineering.wustl.edu/2009/spring/mase5513/abaqus/docs/v6.6/books/usb/default.htm?startat=pt01ch01s02aus02.html

[127] K. Costa, P. Hunter, J. Wayne, L. K. Waldman, J. M. Guccione, and A. D. McCulloch, "A Three-Dimensional Finite Element Method for Large Elastic Deformations of Ventricular Myocardium: II—Prolate Spheroidal Coordinates," *Journal of Biomechanical Engineering*, vol. 118, pp. 464–472, 1996.

[128] R. J. Okamoto, M. J. Moulton, S. J. Peterson, D. Li, M. K. Pasque, and J. M. Guccione, "Epicardial Suction: A New Approach to Mechanical Testing of the Passive Ventricular Wall," *Journal of Biomechanical Engineering*, vol. 122, no. 5, pp. 479–487, 2000.

[129] "t-Test, khi-deux, ANOVA, Régression, Corrélation..." [Online]. Available: https://datatab.fr/tutorial/friedman-test

[130] M. D. Cerqueira, N. J. Weissman, V. Dilsizian, A. K. Jacobs, S. Kaul, W. K. Laskey, D. J. Pennell, J. A. Rumberger, T. Ryan, and M. S. Verani, "Standardized myocardial segmentation and nomenclature for tomographic imaging of the heart," *Circulation*, vol. 105, no. 4, pp. 539–542, 2002.

[131] L. Green, W. X. Chan, M. Ren, C. N. Z. Mattar, L. C. Lee, and C. H. Yap, "The dependency of fetal left ventricular biomechanics function on myocardium helix angle configuration," *Biomechanics and Modeling in Mechanobiology*, vol. 22, no. 2, pp. 629–643, 2023.

[132] P. F. Ferreira, P. J. Kilner, L.-A. McGill, S. Nielles-Vallespin, A. D. Scott, S. Y. Ho, K. P. McCarthy, M. M. Haba, T. F. Ismail, P. D. Gatehouse, R. De Silva, A. R. Lyon, S. K. Prasad, D. N. Firmin, and D. J. Pennell, "In vivo cardiovascular magnetic resonance diffusion tensor imaging shows evidence of abnormal myocardial laminar orientations and mobility in hypertrophic cardiomyopathy," *Journal of Cardiovascular Magnetic Resonance*, vol. 16, no. 1, p. 87, 2014.

APPENDIX A   SHEAR STRESSES IN SENSITIVITY STUDY
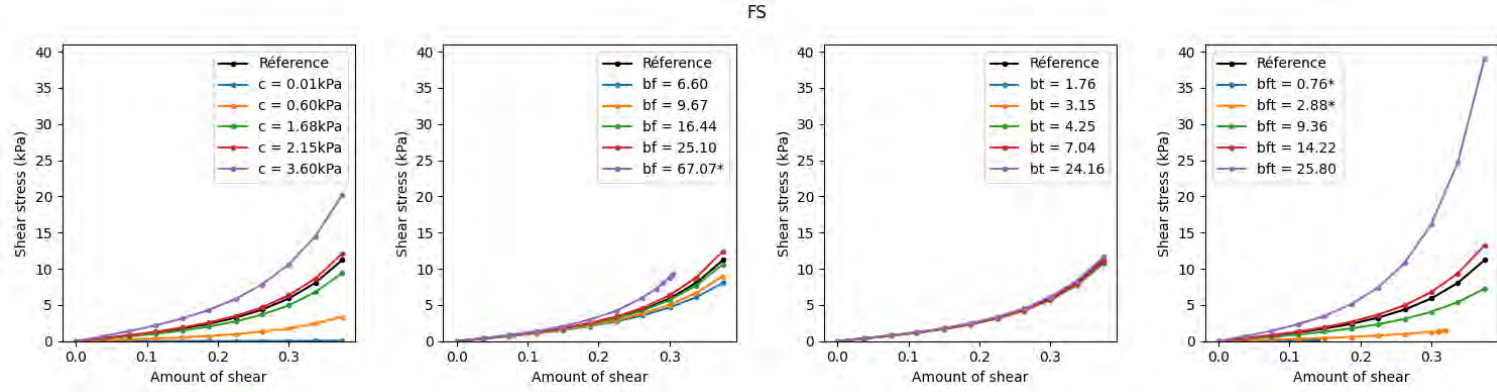
Figure A.1 FS shear stress with varying b_f, b_t, and b_{ft} parameters
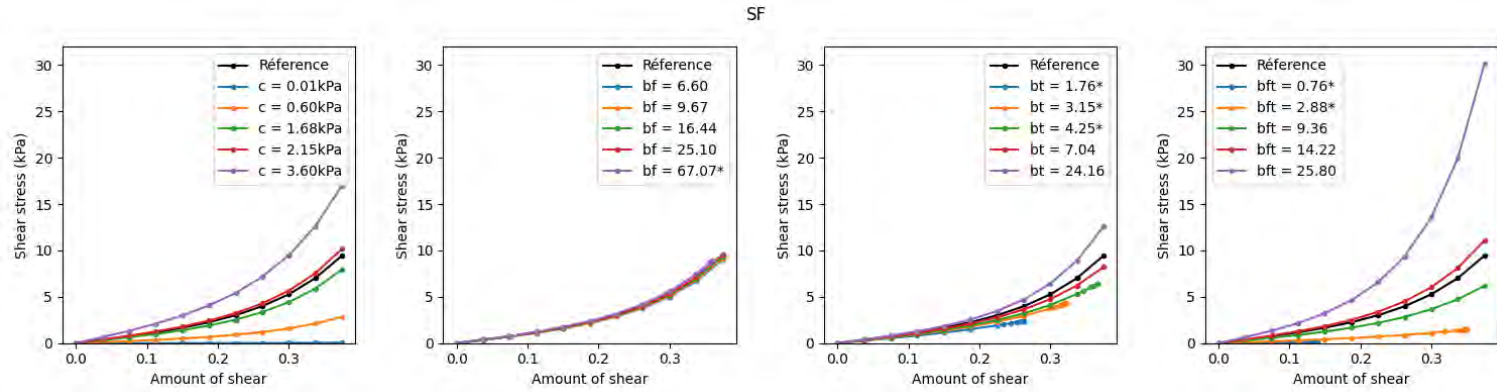
Figure A.2 SF shear stress with varying b_f, b_t, and b_{ft} parameters
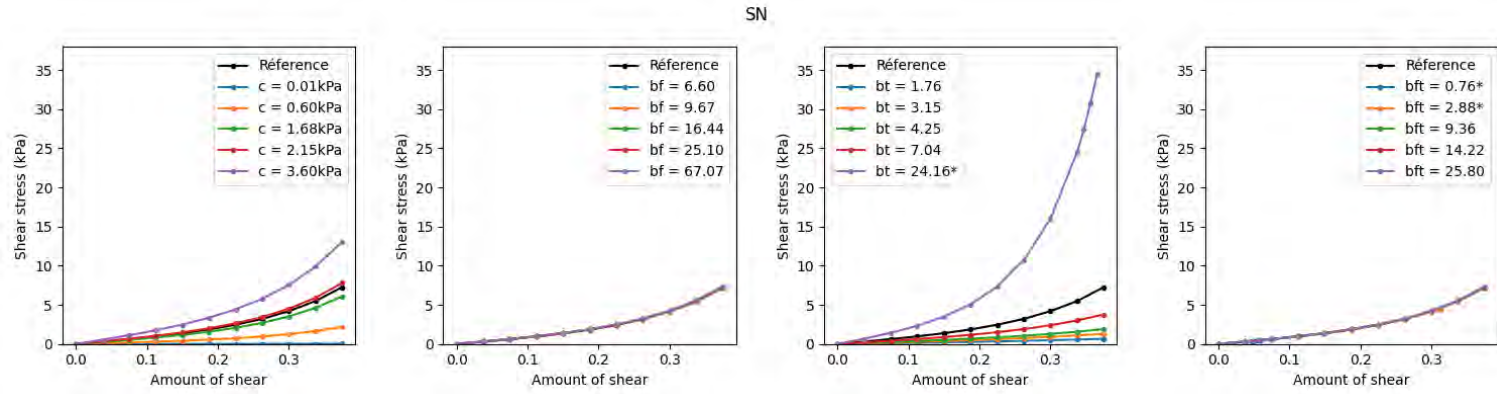
Figure A.3 SN shear stress with varying b_f, b_t, and b_{ft} parameters
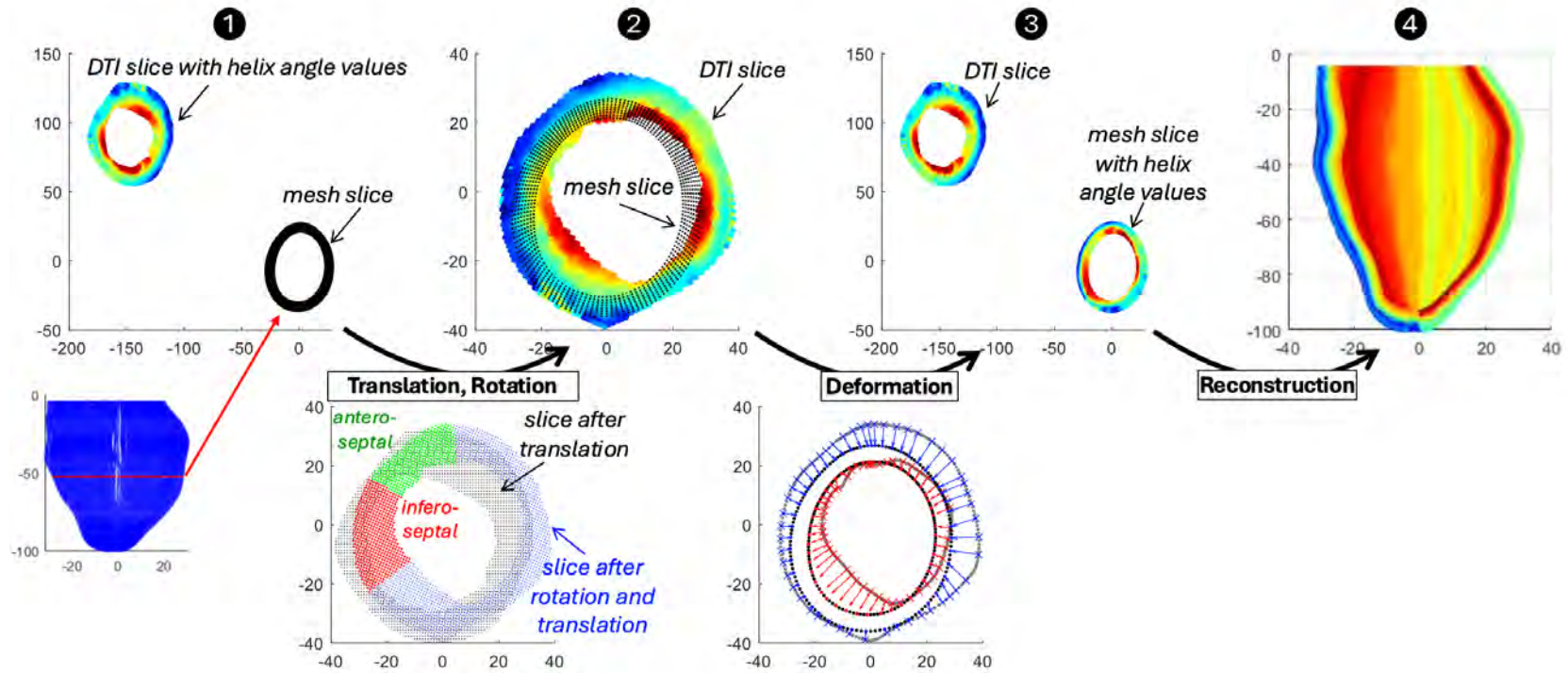
Figure B.1 Schematic representation of DTI-slice based reconstruction method

Figure C.1 Helix angle values in DTI-slice based reconstructions (cross-sectional view)

APPENDIX D   IMPACT OF MAXIMUM HELIX ANGLE ON TRANSMURAL STRESS VALUES
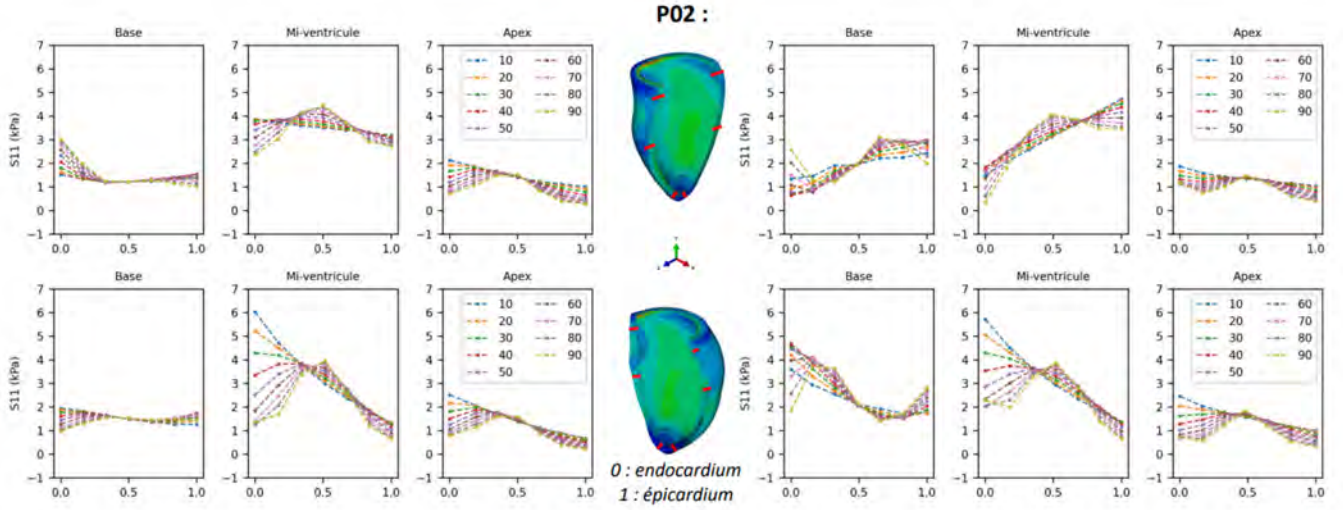
Figure D.1 Transmural stress values when varying maximum helix angle (P02)
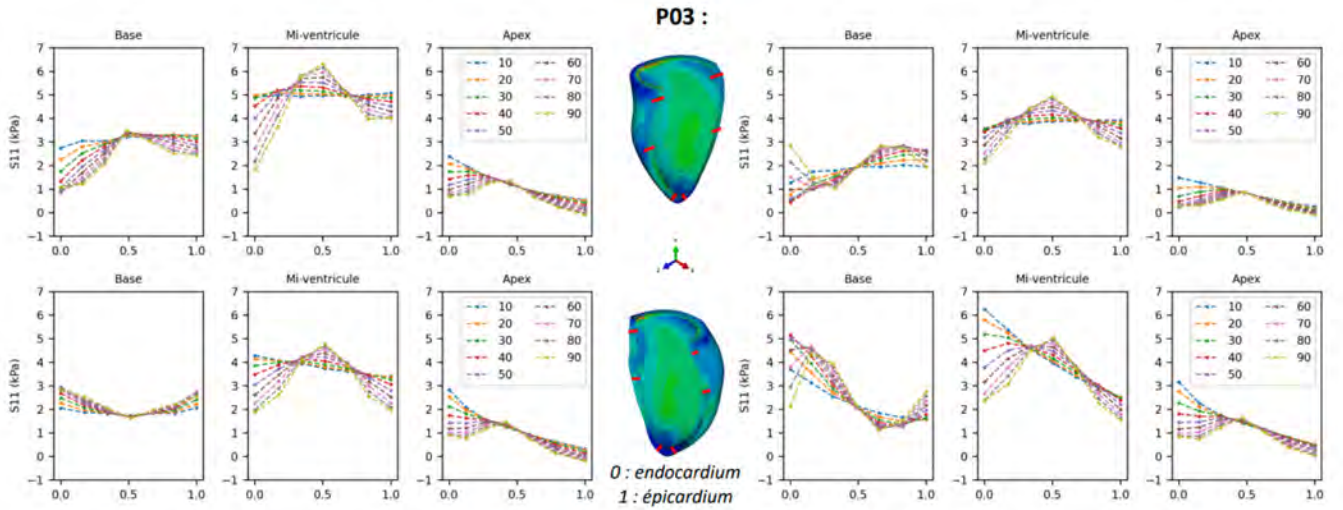
Figure D.2 Transmural stress values when varying maximum helix angle (P03)
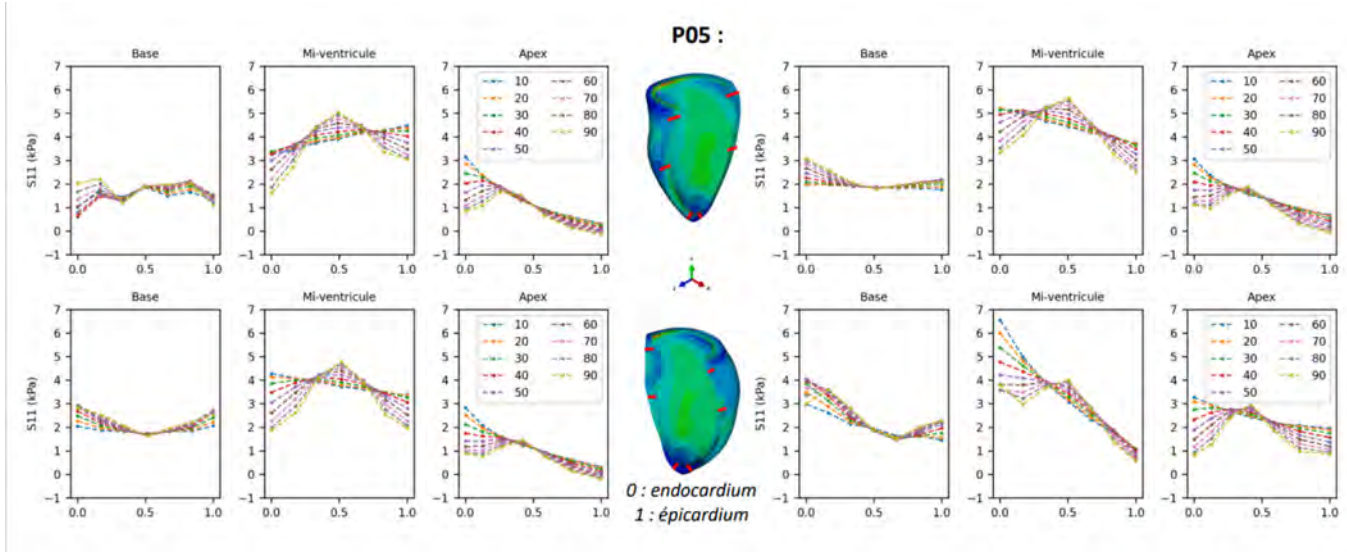
Figure D.3 Transmural stress values when varying maximum helix angle (P05)

APPENDIX E   IMPACT OF MAXIMUM HELIX ANGLE ON STRAIN VALUES
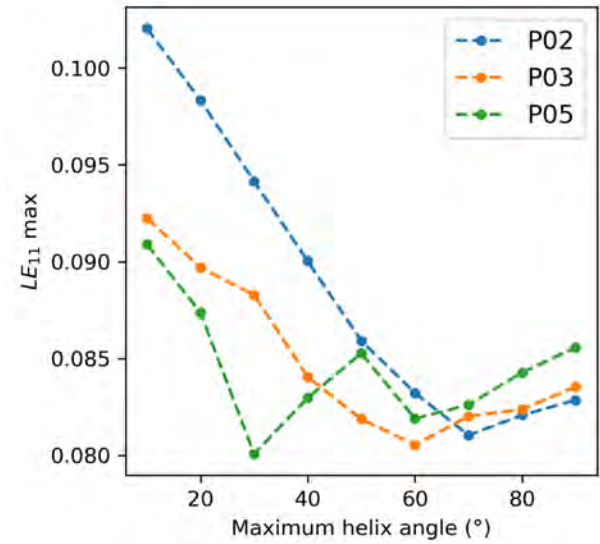
Figure E.1 Maximum strain when varying maximum helix angle
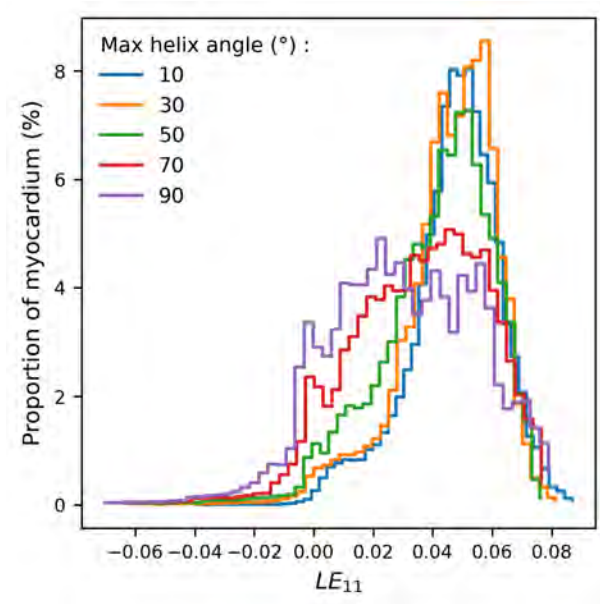
Figure E.2 Strain when varying maximum helix angle (P03)

APPENDIX F   IMPACT OF HELIX ANGLE TRANSMURAL DISTRIBUTION ON DISPLACEMENT VALUES
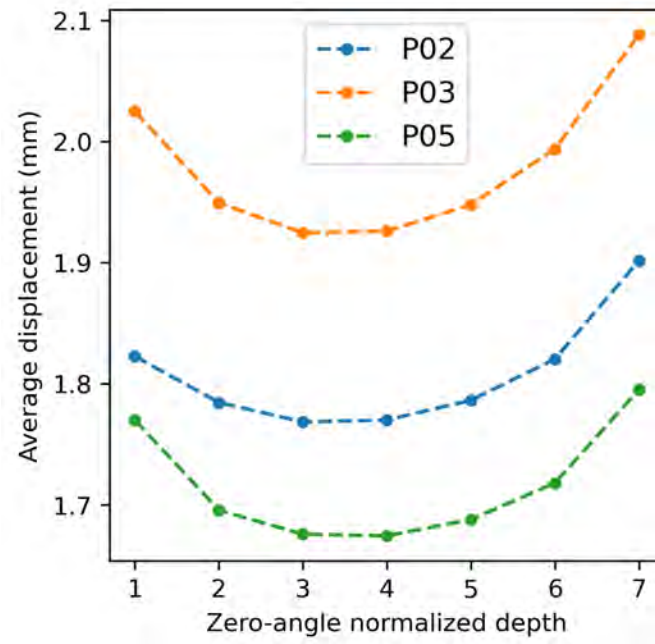
Figure F.1 Average displacement when helix angle transmural distribution

Figure G.1 Maximum stress and displacement values in each affected segment (colored bar) compared to reference orientation (shaded bar)

APPENDIX H   IMPACT OF TRANSVERSE ANGLE ON STRESS, DISPLACEMENT, AND STIFFNESS VALUES
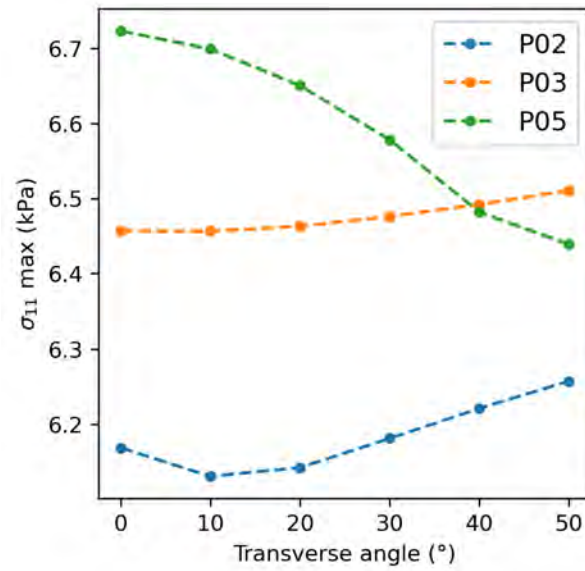
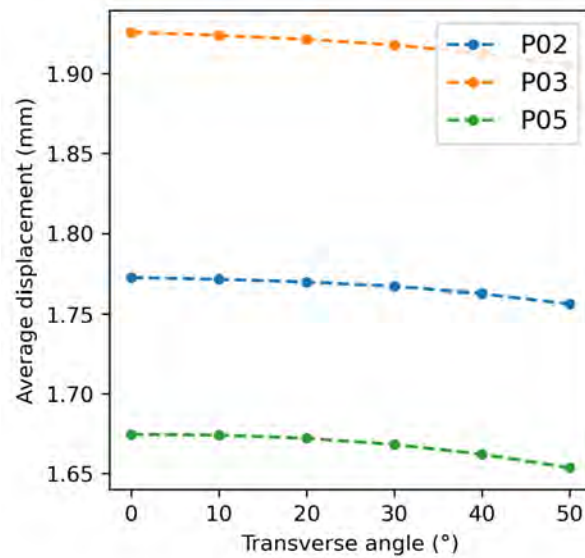Figure H.1 Maximum stress when varying maximum transverse angle

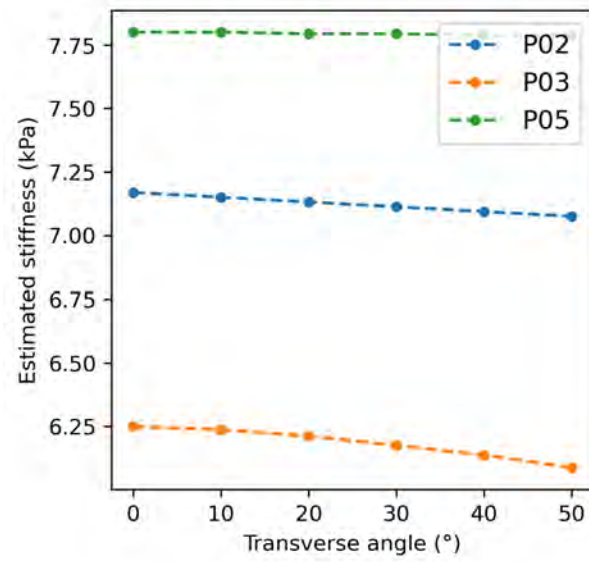Figure H.2 Average displacement when varying maximum transverse angle

Figure H.3 Estimated stiffness when varying maximum transverse angle

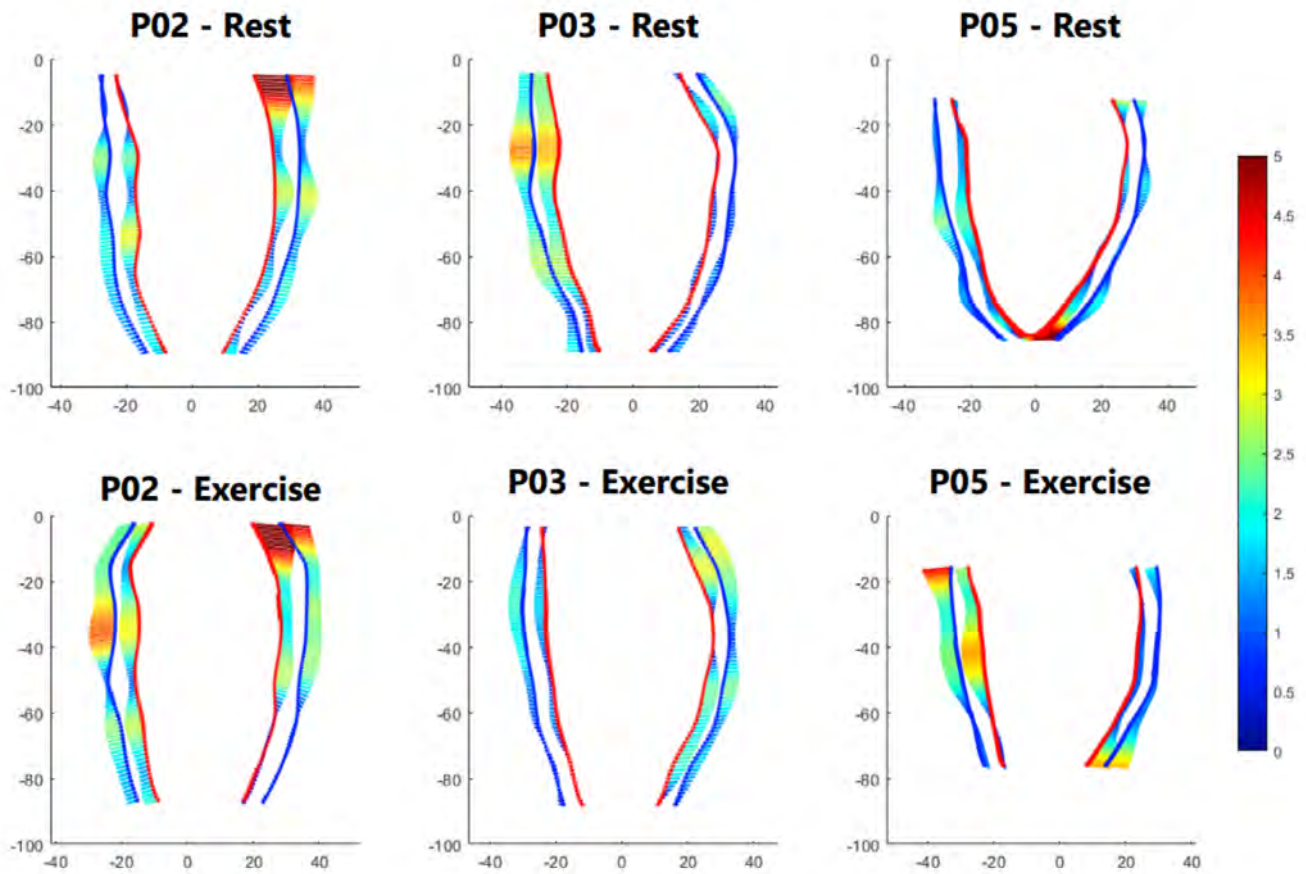**APPENDIX I   TARGET AND SIMULATED DISPLACEMENTS FOR THE 3 SUBJECTS**

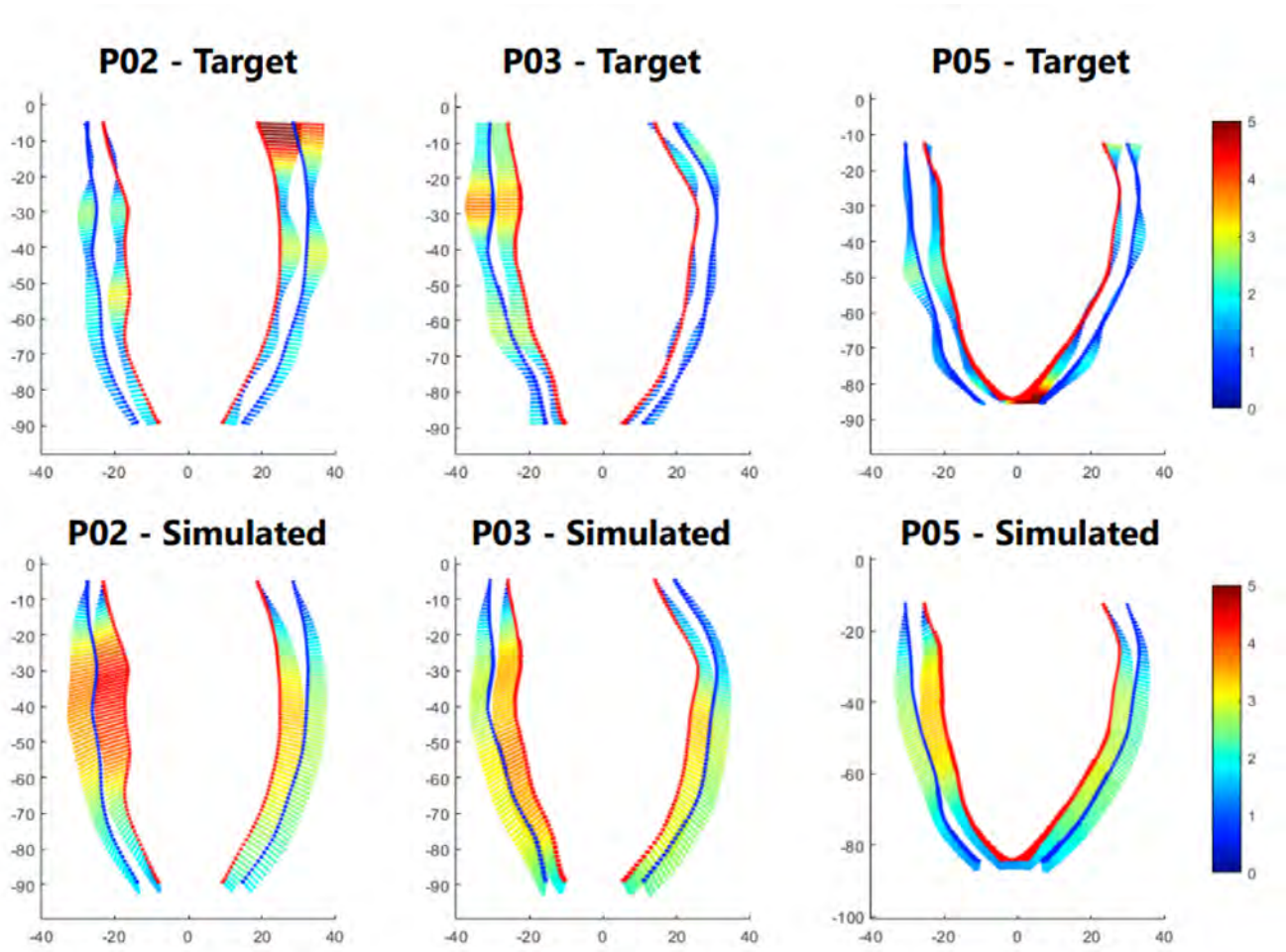Figure I.1 Target displacements for the three subjects at rest and during isometric contractions

Figure I.2 Target and simulated displacements for the three subjects at rest